Title
Computational Modeling in Three Dimensions of Multi-DOF Ship Motion in a Viscous Fluid

Author
JIANG, YICHEN

Publication Date
2014

Peer reviewed|Thesis/dissertation

Computational Modeling in Three Dimensions of Multi-DOF Ship Motion in a Viscous Fluid

by

Yichen Jiang

A dissertation submitted in partial satisfaction of the

requirements for the degree of

Doctor of Philosophy

in

Engineering - Mechanical Engineering

in the

Graduate Division

of the

University of California, Berkeley

Committee in charge:

Professor Ronald W. Yeung, Chair
Professor Ömer Savaş
Professor Per-Olof Persson

Spring 2014

This page intentionally left blank.

Abstract

Computational Modeling in Three Dimensions of Multi-DOF
Ship Motion in a Viscous Fluid
by

Yichen Jiang

Doctor of Philosophy in Engineering - Mechanical Engineering
University of California, Berkeley
Professor Ronald W. Yeung, Chair

The prediction of roll motion of a ship with bilge keels is particularly difficult because of the nonlinear characteristics of viscous damping. Flow separation and vortex shedding caused by bilge keels significantly affect the roll damping and the magnitude of the roll response. To predict roll damping and motion of a ship, the Slender-Ship Free-Surface Random Vortex Method (SSFSRVM) was employed. It is a free-surface viscous-flow solver with low computational cost so that it can run on a standard desktop computer. It features a quasi-three dimensional formulation that allows the decomposition of the three-dimensional hull problem into a sequence of two-dimensional computational planes, in which the two-dimensional free-surface Navier-Stokes solver FSRVM can be applied. In this work, the SSFSRVM methodology has been further developed to model multi-degrees of freedom of free-body motion in the time domain. This version of SSFSRVM model does not require the assumption of small amplitude motion, and is capable of having viscosity turned on or off in the solution procedure. Because FSRVM uses a grid-free formulation, there is no issue with numerical viscosity.

We validated the SSFSRVM in simulating the free roll decay motion of a naval vessel without forward speed. The numerically predicted vorticity distributions at different time instants near a bilge keel closely matched experimental PIV images. We found that the SSFSRVM model is capable of predicting the roll motion of a hull, and capturing the behavior of the vortical structures in the fluid. Further, we examined how the roll decay coefficients and the flow field were altered by the span of the bilge keels, based on the time-domain simulation of the coupled hull and fluid motion. Plots of vorticity contours and iso-surfaces along the three-dimensional hull

were presented to reveal the motion of fluid particles and vortex filaments near the keels. In addition, the generation of the quadratic roll damping was investigated by showing the bilge-keel hydrodynamic moment and the pressure distribution on the hull surface and bilge keels.

Finally, the predicted roll time histories of a naval hull with three different forward speeds were compared with those obtained from experimental measurements. The numerical predictions were in good agreement with the experimental measurements for all three speeds. In addition, the numerical model also successfully produced the divergent waves with the same angles as those measured in the experiment, and accurately predicted the locations of the peaks and troughs of the divergent waves. The motion of the sonar-dome and bilge-keel vortex filaments, as well as their interactions, were presented to investigate the effect of forward speed. Significant influences of forward speed on the roll motion and roll damping were noted and explained.

Acknowledgments

I would first thank my advisor Professor Ronald W. Yeung for his invaluable guidance and advice throughout my Ph.D. studies. His encouragement and willingness to help are deeply appreciated. His brilliance, resourcefulness, and patience are greatly admired. Without him, this work would not have been possible. He has been instrumental to my academic growth, as well as my personal growth. I appreciate his constant support and for allowing me to attend important conferences and various SNAME events. I truly thank him offering me the opportunity to study and work with him in Berkeley.

I would like to thank my thesis committee members: Professor Ömer Savaş and Professor Per-Olof Persson for their help and support during my doctoral study. I would also like to thank Professor Alaa Mansour and Professor Fai Ma for being the committee members of my qualifying examination. It is an great honor to have learned from all of them.

I believe that I would not have been a Ph.D. student if it were not for the advice and consistent support of my undergraduate and Master advisor Professor Shugeng Yang at Tianjin University. I cannot thank him enough for his guidance, encouragement, and support throughout my undergraduate and master studies.

I also believe that I have had the great opportunity to work with bright individuals in the Berkeley Ocean Engineering Group. I really appreciate their support and assistance. These individuals are: Nathan M. Tom, Sam Kanner, Christophe Cochet, Meghan Hough Sinclair, Farshad Madhi, Louis-Alexandre Couston, Mohamed Hariri Nokob, Abdulrahman Jbaily, and Lu Wang. I would like to wish them all the best during their graduate studies and future careers.

I would like to thank the China Scholarship Council for their financial support during my first four years of my Ph.D. studies, and I would like also to thank the Office of Naval Research for their support of this research under Grant # N00014-09-1-1086 at UC Berkeley

Most importantly, I would like to thank my family for their love and consistent support. I would like to thank my parents Niankun Jiang and Guangling Men, and my fiancee Jiawen Li. Without their support and patience I would have never reached this point. I would also like to thank my brother Yiting Jiang for always encouraging me and being supportive of my decisions. I am forever grateful for their love and kindness.

- Yichen Jiang

Contents

List of Figures

List of Tables

Nomenclature

L	Length of a vessel
B	Beam of a vessel
T	Draft of a vessel
N	Number of sections of a vessel
U	Forward speed of a vessel
ϵ	Small parameter of a vessel geometry
Fr	Length based Froude Number, $\frac{U}{\sqrt{gL}}$
x	Horizontal/lateral coordinate, positive port side
y	Vertical coordinate, positive upward
χ	Longitudinal coordinate, positive forward
G	Gravitational acceleration
χ, x, y	Coordinates in the referenced translating coordinate system, $O\chi xy$
χ_i, x_i, y_i	Coordinates in the translating sub-coordinate system, $O_i\chi_i x_i y_i$
$\overline{\chi}, \overline{x}, \overline{y}$	Coordinates in the earth-fixed coordinate system, $\overline{O}\overline{\chi x y}$
$\hat{\chi}, \hat{x}, \hat{y}$	Coordinates in the body-fixed coordinate system, $\hat{O}\hat{\chi}\hat{x}\hat{y}$
$\dot{x}_b, \dot{y}_b$	Velocity of body origin, $\hat{O}$
$\dot{\theta}_b$	Roll angular velocity
$\dot{\gamma}_b$	Pitch angular velocity

$\dot{\alpha}_b$	Yaw angular velocity
θ_b	Body roll angle, positive anticlockwise from bow
γ_b	Body pitch angle, positive anticlockwise from port side
α_b	Body yaw angle, positive anticlockwise from above
$\mathbf{V}$	Fluid velocity vector, $\mathbf{V} = (\mathsf{u},\ u,\ v)$
u	Local fluid velocity, χ-component
u	Local fluid velocity, x-component
v	Local fluid velocity, y-component
$\mathbf{u}$	Cross-plane velocity vector of components, (u, v)
$\mathbf{\Omega}$	Fluid vorticity vector, $\mathbf{\Omega} = (\xi,\ \eta,\ \zeta)$
ξ	Local fluid vorticity, χ-component
η	Local fluid vorticity, x-component
ζ	Local fluid vorticity, y-component
ρ	Density of the fluid
p	Local fluid pressure
ν	Kinematic viscosity
Re_B	Reynolds number, based on the transverse dimension
$\tilde{D}_t$	Three-dimensional material derivative
∇'_{2D}	2-D gradient operator with respect to the (x, y)- variables
$\mathbf{n}$	Three-dimensional unit normal vector outward to the fluid
$\vec{n}_{2D}$	Two dimensional unit normal vector of a vessel section
$\vec{\tau}_{2D}$	Two dimensional unit tangent vector of a vessel section
t^*	Pseudo-time variable, $\frac{L/2-\chi}{U}$

L_i Distance from i-th section to the midship section

$F(\hat{x}, \hat{y}, \hat{\chi})$ Function defining three dimensional vessel surface

$\mathcal{B}(x, y; t^*)$ Function defining two dimensional boundary of a vessel section

n_χ Normal vector in χ direction

D Computational domain

∂D Boundary of computational domain

∂D_b Body boundary of computational domain

∂D_f Free surface boundary of computational domain

∂D_Σ Far field boundary of computational domain

$\vec{x}$ Position vector

$\vec{u}$ Velocity vector

z Complex variable, $= x + \mathsf{i}y$

w Complex velocity, $= u - \mathsf{i}v$

w^* Conjugate of complex velocity

β Complex potential, $= \phi + \mathsf{i}\psi$

$\beta_{\mathbf{h}}$ Homogeneous component of the complex potential

$\beta_{\mathbf{v}}$ Vortical component of the complex potential

ϕ Velocity potential

ϕ_h Homogeneous component of the velocity potential

ϕ_v Vortical component of the velocity potential

ψ Stream function

ψ_h Homogeneous component of stream function

ψ_v Vortical component of stream function

Γ_i Circulation of blob i

$f(r)$ Blob core function

σ Blob core radius

R_b Radial distance from body origin

$x_{bo,i}, y_{bo,i}$ Coordinates of a body node on the i-th seciton, with respect to the referenced translating coordinate system

$\hat{x}_{bo,i}, \hat{y}_{bo,i}$ Coordinates of a body node on the i-th seciton, with respect to the body-fixed coordinate system

O Origin of the referenced translating coordinate system

O_i Origin of the i-th translating sub-coordinate system

G Center of gravity

$x_{\hat{O}_i}, y_{\hat{O}_i}$ Position of point O_i

$\theta_{\hat{O}_i}$ Roll angle of the i-th section

x_b Sway of the vessel

y_b Heave of the vessel

$\dot{\theta}_b$ Roll angular velocity

γ_b Pitch of the vessel

α_b Yaw of the vessel

M_b Body mass

$\vec{R}_G$ Position of point G in the referenced translating frame, $\doteq (\chi_G, x_G, y_G)^T$

$\ddot{\chi}_G, \ddot{x}_G, \ddot{y}_G$ Translational accelerations at point G

$\ddot{\theta}_G, \ddot{\gamma}_G, \ddot{\alpha}_G$ Angular accelerations at point G

$\vec{F}_G$ Force vectors at point G, $\doteq (\tilde{F}_\chi, \tilde{F}_x, \tilde{F}_y)^T$

$\vec{M}_G$ Moment vectors at point G, $\doteq (\tilde{M}_\chi, \tilde{M}_x, \tilde{M}_y)^T$

$\vec{M}_O$	Moment vector at point O, $\doteq (M_\chi, M_x, M_y)^T$
$\vec{a}_G$	Linear acceleration at point G
$\vec{a}_b$	Acceleration at point O
$I_{\chi\chi}$	Roll moments of inertia at point O
I_{xx}	Pitch moments of inertia at point O
$F_{1,i}$	Lateral forces acting on the i-th station
$F_{2,i}$	Vertical forces acting on the i-th station
$F_{3,i}$	Roll moment acting on the i-th station
ΔL	Distance between any two adjacent sections
η_i	Consecutive double roll amplitude
$\forall$	Displacement
B_2	Quadratic damping coefficient
C_B	Block coefficient
C_D	Drag coefficient
F_D	Drag force
F_r	Froude number
GM	Metacentric height
k_{44}	Roll radius of gyration
R_0	Initial roll angle
S	Area of a body projected on the crossplane normal to the direction of motion
S_w	Wetted surface area
U_b	Velocity of body
n	Non-dimensional roll decay coefficient

Chapter 1

Introduction

Consideration of the static and dynamic stability properties of a ship is fundamental to its design and safe operation.The stability of a ship, which is necessary to avoid capsizing, is directly related to its roll motion. The natural period of roll is designed to be away from the period of the higher energy of the wave spectrum. However, the encountering frequency and direction of waves could lead to the coalescing of the two periods, which may cause severe motion or serious damage because of excessive motion. In the unfortunate situation where resonant roll motion takes place, large damping is the only recourse to reduce the hazardous response. Bilge keels have been the traditional passive "stability enhancement system", offering an increase in the hydrodynamic resistance when a ship rolls, thus limiting roll motion and yet requiring little increase in operation costs.

1.1 Background and motivation

The primary damping mechanism arising from a bilge keel is the formation and shedding of vortices. These vortices significantly affect the roll damping and make the prediction of roll motion very difficult. Since the time of William Froude, a number of theoretical and experimental approaches have been taken to assess the nonlinear behavior of roll damping which led to the so-called quadratic model of the damping moment (Froude, 1872). The nonlinear model has a linear component plus another component proportional to $\dot{\theta}_b|\dot{\theta}_b|$, where $\dot{\theta}_b$ denotes the roll angular velocity.

The total roll damping has several components which are usually considered as: (1) surface friction damping, (2) wave damping, (3) eddy-formation damping, (4)

bilge keel damping, and (5) lift-effect damping due to the forward speed. Since the hydrodynamic interaction among these components is unavoidable, the subdivision of roll damping may not be justifiable easily. However, it is convenient to compute the individual component analytically and experimentally. Among these components, the bilge keel damping is considered to be composed of the normal-force damping of bilge keels, hull pressure damping due to bilge keels, and wave damping, due to bilge keels. The earliest prediction methods for these components were proposed by Ikeda *et al.* (1976, 1977a, 1977b, 1978) about 25 years ago. A complete and comprehensive review was made by Himeno (1981). The concept of the component-based damping has been widely used for typical rounded ship hulls with small bilge keels.

However, hulls with different shapes and larger bilge keels behave differently and various methods were proposed to improve accuracy of the damping prediction and to extend their applicability to multiple ship designs. Ikeda (2004) also detailed improvements to his method to determine optimal location for placement of the bilge keels. Changes have also been made to extend Ikeda's method to high-speed planing craft, with modifications to the lift component (Ikeda and Katayama, 2000), and high-speed multi-hull vessels, with modifications to the wave-making, eddy, and lift components (Katayama, et al., 2008). Additional studies have also examined some of the limitations of Ikedas method for application to ships with buttock flow stern geometries (Kawahara, et al., 2009) and large bilge keels (Bassler and Reed, 2009). A piecewise linear approach is presented to model large amplitude roll damping, with consideration of the abrupt physical changes, such as bilge keel emergence and deck submergence at large roll angles (Bassler, *et al.*, 2010).

To represent better roll-damping behavior, higher-order polynomials of the roll damping coefficient were proposed in several publications. For instance, Roberts (1985) developed linear-plus-quadratic and linear-plus-cubic damping forms. Turk, *et al.* (2013) proposed a linear-plus-quadratic-plus-cubic damping form for the prediction of parametric rolling of a container ship in regular waves. However, based on experiments, it is found that when the roll angle exceeds a certain value, the damping coefficient saturates in value. This clearly indicates that a higher polynomial fitting does not mean a better prediction. More importantly, the polynomial form may not be consistent with the nonlinear nature of the roll damping. Additionally, the damping at large anlges is over-predicted by using the polynomial form. This is unsafe in the design process of a floating structure.

Oliveira & Fernandes (2006) found that the damping stops increasing when the roll

angle reaches a certain value. Then, they proposed a bilinear methodology to deal with the nonlinear behavior of roll damping. Later, a hyperbolic tangent function was recommended by Oliveira & Fernandes (2014) because the bilinear methodology failed to reflect the continuous behavior of the nonlinear damping. However, as the roll angle increases to larger values, the roll damping starts to decrease, rather than maintain a constant value (see Avalos *et al.*, 2013).

Experimental works have shown that the roll damping depends on the amplitude and frequency of the roll motion in a very complicated manner. The hull shape is certainly another important factor in the type of nonlinear roll damping. Therefore, having a numerical method that can accurately and quickly predict the roll motion will be significantly helpful in designing a ship, as well as understanding the nonlinear behavior of roll damping.

1.2 Prediction of roll damping

The radiation damping of ships is usually computed by linear diffraction/radiation theories, such as inviscid strip theories (Xia, *et al.*, 1998; de Kat, *et al.*, 2002; Ribeiro e Silva and Guedes Soares, 2013), panel methods (Nakos and Sclavounos, 1991; Beck, 1994; Kim, 2002), and system-based filtering methods (Sadat-Hosseini, *et al.*, 2011; Araki, *et al.*, 2012; Han and Kinoshita, 2012). This radiation damping is adequate for an accurate prediction of the rigid body motion for most degrees of the freedom (Chakrabarti, 2001). However, this is not necessarily true for the roll motion. In this case, the radiation damping is generally small compared to the total damping. Although inviscid numerical methods have been widely used in different applications, they are usually complemented by empirical or experimental data to estimate the linear and nonlinear roll damping coefficients because of the absence of modeling the viscosity of the fluid.

Recently, with the continuous increase in computational power, the Reynolds Averaged Navier Stokes (RANS) flow solvers have also been applied in this area and show promise (e.g. Broglia and Di Mascio, 2003; Wilson *et al.*, 2006; Miller *et al.*, 2008; Quérard *et al.*, 2008), but they may require finer grids and Detached Eddy Simulation (DES) turbulence modeling for large roll angles to achieve high-fidelity simulations. Salui *et al.* (2000) noted that the application of a RANS solver to predict the ship motion is still computationally intensive. Issues of mesh density and

long computational time often prevail, and the Computational fluid dynamic(CFD) method may not be the most effective analysis tool in a design process with multiple parameters.

1.3 Slender-ship free-surface random-vortex method

In parallel to classical inviscid theories and CFD, the Free-Surface Random-Vortex Method (FSRVM) has also been described in a sequel of works (see Yeung and Cermelli, 1998; Yeung, *et al.*, 2000; Yeung, 2002). This represents an efficient grid-free numerical method developed to model viscous flow in the presence of a free surface. The method is based initially on the Random Vortex algorithm (Chorin, 1973), but had been significantly improved to accommodate bodies of arbitrary shapes, as well as been reformulated to include the effects of surface waves. There has been considerable success in applying this methodology to simulate flows near sharp keels and fins (e.g. Yeung, 2002, Roddier *et al.*, 2000, Thiagarajan & Braddock, 2010, Yeung & Jiang, 2011, Jiang & Yeung, 2012). These earlier developments, however, can only simulate two-dimensional floating bodies.

To predict the roll damping of a three-dimensional vessel in prescribed motion, we have completed some recent theoretical development, using the UC-Berkeley code, called SSFSRVM (Slender-Ship Free-Surface Random Vortex Method). SSFSRVM is a fast free-surface hydrodynamics solver designed to run on a standard desktop computer. It features a quasi-three dimensional formulation involving decomposing the problem into a sequence of two-dimensional computational planes (Seah, 2008). The theory for this 3-D to 2-D conversion was initially conceived in Yeung & Kim (1981) for an inviscid fluid. However, its extension to a viscous fluid took some time to develop. It was obtained using scaled variable analysis by Yeung *et al.* (2013), which allowed the two-dimensional computational engine of FSRVM (Liao, 2000) to be used for 3D flow. Previously, the most advanced applications were given in Seah & Yeung (2008), in which the exact body boundary condition was satisfied on the instantaneous wetted surface of the moving vessel with inviscid but fully nonlinear free-surface boundary conditions. Documentation of the results for these forced or prescribed motion cases were given by Seah & Yeung (2008) and Yeung et al (2013).

This version of SSFSRVM model does not require the assumption of small amplitude motion, and is capable of having viscosity turned on or off in the solution

procedure. Because FSRVM uses a grid-free formulation, there is no issue with numerical viscosity, and the method is efficient in producing accurate predictions at a fraction of the time required by methods such as RANS (Sarkar & Vassalos, 2000). Thus, SSFSRVM offers an efficient and effective alternative to simulate the prescribed motion. However, this version of SSFSRVM cannot predict the free-body motion.

1.4 Research objective

There are three objectives for this research. The first objective is to further develop the SSFSRVM model with the capability of accommodating the free-body motion in the time domain. The second objective is to gain insight into the physics of the flow-field of a rolling ship hull because of the presence of the bilge keels and to study the influence of the bilge-keel span, by using the SSFSRVM model. The third objective is to investigate the effects of forward speed of the vessel on the roll motion and the roll damping.

To achieve these objectives, the solution of the free motion of a three-dimensional body is carried out in a manner similar to the 2-D treatment of Roddier *et al.* (1999), allowing one to model the dynamic coupling between body and fluid motion, but now with the full capability of four degrees of freedom: free sway, heave, roll, and pitch. Chapter 2 shows the derivation of this physical problem.

In this work, we firstly examined the effectiveness of SSFSRVM modeling by comparing the time histories of free roll-decay motion resulting from simulations and experimental measurements. Furthermore, the detailed vorticity distribution near a bilge keel obtained from the numerical model were compared with the experimental PIV images. Chapter 3 examines the effectiveness of SSFSRVM modeling by comparing the time histories of free roll-decay motion resulting from simulations and experimental measurements. Moreover, the predicted vorticity distributions at different time instants near a bilge keel obtained from the numerical model closely match with the experimental PIV images. In Chapter 4, four ship models with different bilge-keel spans are built numerically to evaluate the effects of the bilge-keel span on the roll motion and damping. In addition, the roll responses of these four ship models in regular incident beam waves are also presented and discussed. Chapter 5 examines the influence of the hull speed by taking into account various hull speeds, including zero speed case. The motion of the sonar-dome and bilge-keel vortex filaments, as

well as their interactions, are presented to reveal how the presence of forward speed alters the vorticity field. Additionally, time series of surface waves are given to study the wave damping.

The numerical predictions of the roll motion and the vorticity field near a bilge keel are in good agreement with the experimental measurements. Significant influences of the bilge keel and the forward speed of the vessel on the roll motion and roll damping are noted and explained by using the SSFSRVM model.

Chapter 2

Methodology

Based on the slender body theory, a three-dimensional problem can be reduced into a sequence of two-dimensional problems, for an adequately slender hull. The approximation is not obvious if the fluid is viscous and is discussed in Yeung *et al.* (2013). The hull is geometrically defined by a sequence of sectional profiles (or stations) which are equally spaced along the length of the vessel, see Fig. 2.1. We allow the presence of forward speed U. The transient flow problem in each two-dimensional cross-plane is solved by FSRVM.

2.1 Overview of slender-ship FSRVM

In practice, the vessel is usually initially defined by a sequence of sectional profiles (or stations) which are arrayed equally along the length of the vessel, as seen in Figure 2.1. It is assumed that in one time step the vessel moves forward by $d\chi$ which is the distance between two stations, and the vessel moves one body length in one computational period. By this assumption, the number of sections used directly determines the size of the time step through:

$$\Delta t = \frac{L/U}{N-1} \tag{2.1}$$

where N is the number of sections used to define the vessel. Thus, smaller forward velocities (U) imply a greater time step. If too few sections are used, the time step becomes very large, leading to numerical instability.

As the vessel passes a computational plane, the initial cross sectional profile considered is that near the bow of the vessel. This is generally much narrower than

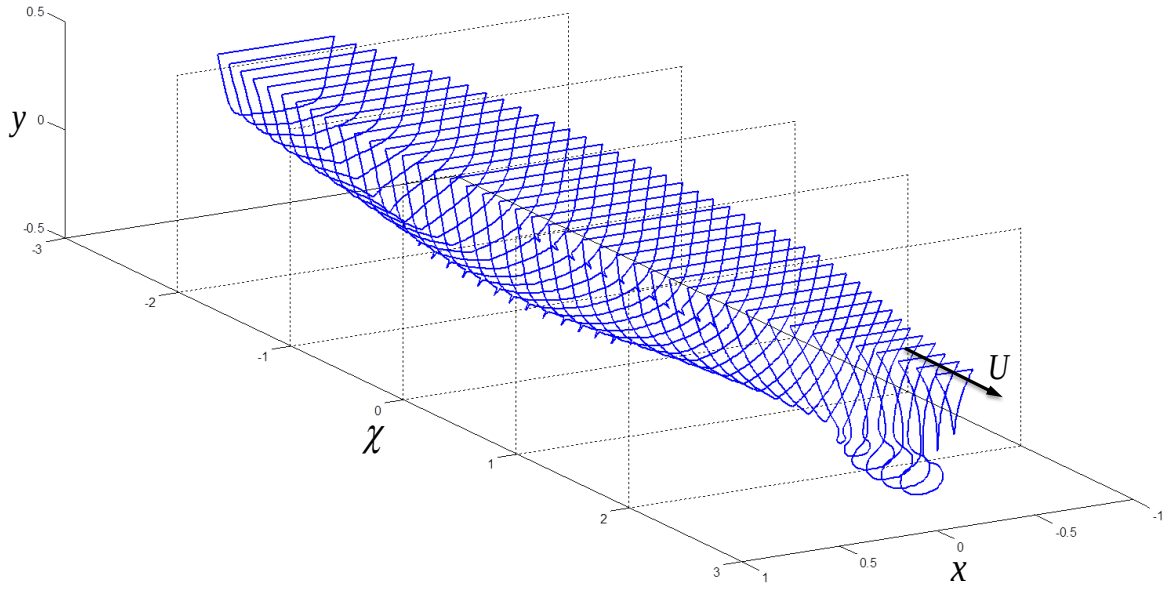

Figure 2.1: Computational planes along the longitudinal axis χ.

that of the midship section. As the vessel continues to move through the plane, the profile expands, before eventually contracting near the stern. Once the vessel passes completely through the plane at the stern, a new plane is generated at the bow.

Figure 2.2 shows an example of the distribution of body nodes in the first fifty computational sections from the bow. It can be seen that the body nodes are placed along the streamline. By assuming that the vessel moves forward by $d\chi$ in one time step, the fluid particle located at node ① will move along with the streamline to node ② in the next time step. Hence, the cross-sectional velocity of the fluid particle will transfer from node ① to node ②. Based on this idea, the fluid data of each body section will transfer to the next section in the next time step, except for the last section. The data flow is shown in Figure 2.3. However, it is worth noting that the fluid data of the free-surface nodes and blobs in each section will stay in the section without transferring.

2.2 Coordinate systems

For a ship hull, six independent coordinates are necessary to represent its position and attitude (see Fig. 2.4): surge, sway, heave, roll, pitch and yaw. In the current SSFSRVM model, three different coordinate systems are used to develop and solve the rigid-body motion of the vehicle, (Fig. 2.4). The first one is an earth-fixed coordinate

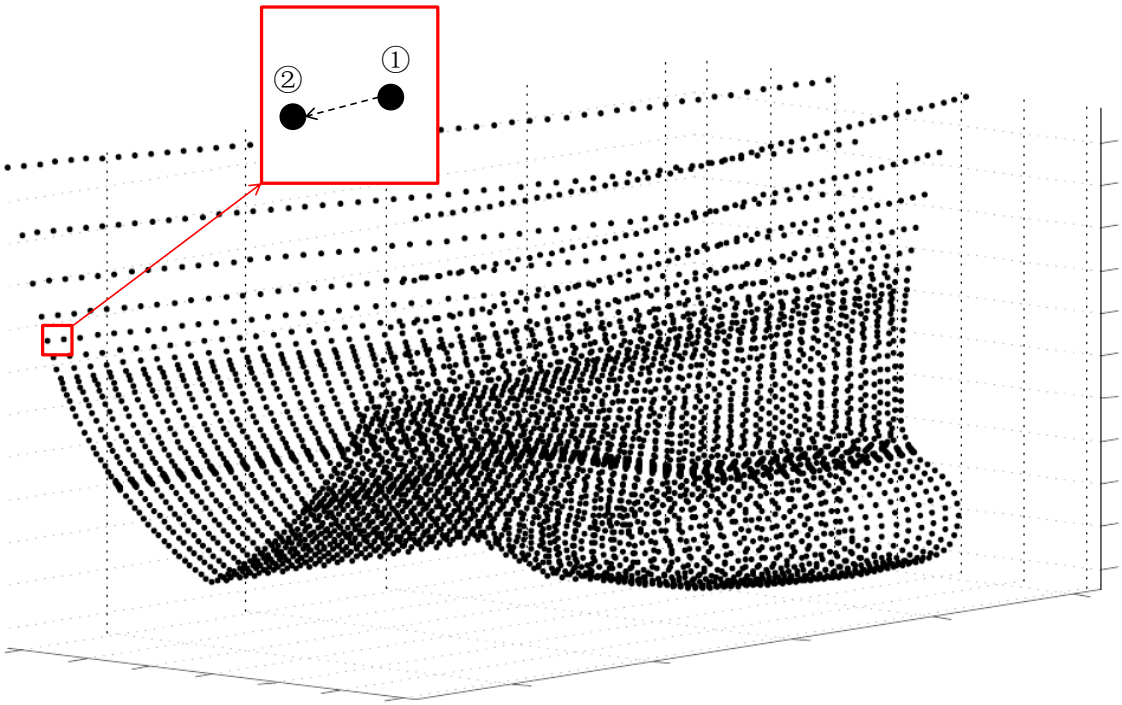

Figure 2.2: Body nodes and information transfer between nodes.

system $\overline{O}\overline{x}\overline{y}\overline{\chi}$, which is used to record the translational motion and the rotation of the vessel. The $(\overline{O}\overline{x}\overline{\chi})$-plane lies on the still water surface, the positive $\overline{\chi}$-axis is in the direction of the forward speed, and the positive $\overline{y}$-axis points upwards. We use χ instead of the conventional x to denote the forward direction as it is desirable to name the sectional-plane variables $(x,\ y)$ so that the complex variable $z = x + iy$ can be used as in FSRVM (Yeung, 2002). At the initial time, the origin of the earth-fixed coordinate system coincides with the geometrical center of the ship, $\hat{O}$, which is the intersection point of the still water plane, the midship plane and the centerplane.

The second coordinate system is a body-fixed coordinate system $\hat{O}\hat{x}\hat{y}\hat{\chi}$, which is used to define the position of the body nodes, with $\hat{O}$ attached to the geometrical center of the ship. $\hat{\chi}$ points in the forward longitudinal direction of the ship, $\hat{x}$ in the port-side direction, and $\hat{y}$ in the upward direction.

The third coordinate system $Oxy\chi$ is a steadily moving frame of reference that has the same constant forward speed as the vessel. When the vessel does not have a forward speed, $Oxy\chi$ would be fixed on earth and is essentially the same as the earth-fixed coordinate system $\overline{O}\overline{x}\overline{y}\overline{\chi}$. There are N translating coordinate systems with one for each 2D computational plane. Each one of these translating sub-systems

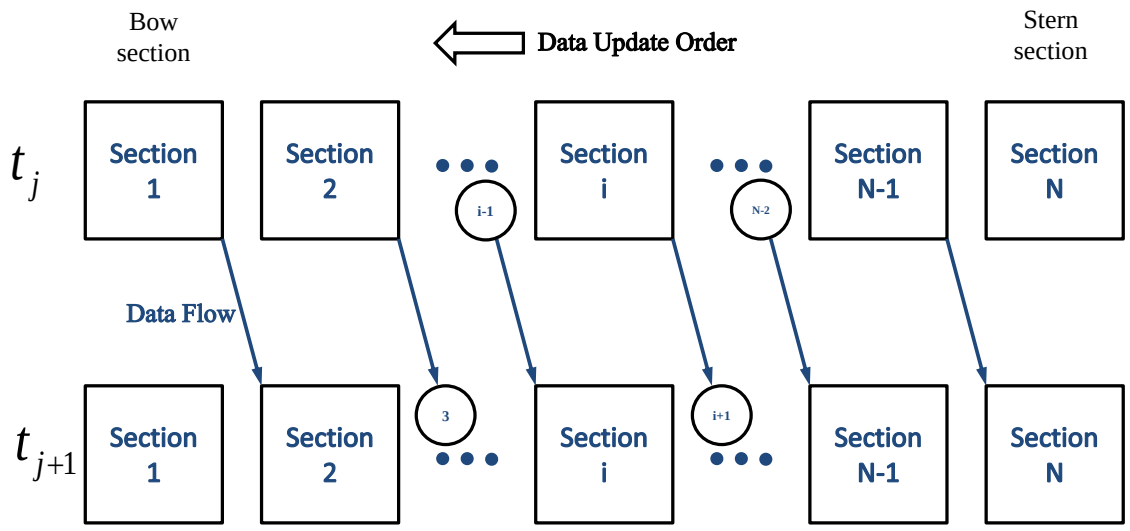

Figure 2.3: Data flow.

is set up to solve the two-dimensional transient flow problem. Figure 2.5 illustrates an example of the translating *sub-systems*, with origin O_i. The directions of the $x_i y_i \chi_i$ axes of each sub-system are set to be the same as those of the translating $xy\chi$ axes. Therefore, the $(O_i x_i \chi_i)$-plane also lies in the still water surface with the y_i-axis pointing upward. Among the translating coordinate systems, the one at mid-ship is chosen to describe the global equations of motion of the vessel, and is named as the **referenced** translating coordinate system, $Oxy\chi$. The others are named as translating sub-coordinate systems. At the initial time, the origin O is located at the origin of the earth-fixed coordinate system. Since the vessel could be allowed to move forward with sway and heave motion, the body center, $\hat{O}$, would not necessarily be coincident with the referenced origin O.

2.3 Near-field approximation

Slender body theory is a methodology that can be used to take advantage of the slenderness of a body in order to obtain an approximation to the field surrounding it. In this section, we will carry out an order-of-magnitude analysis under a slender body assumption in order to apply the combination of slender body theory and FSRVM to a three dimensional problem. The following development of the near-

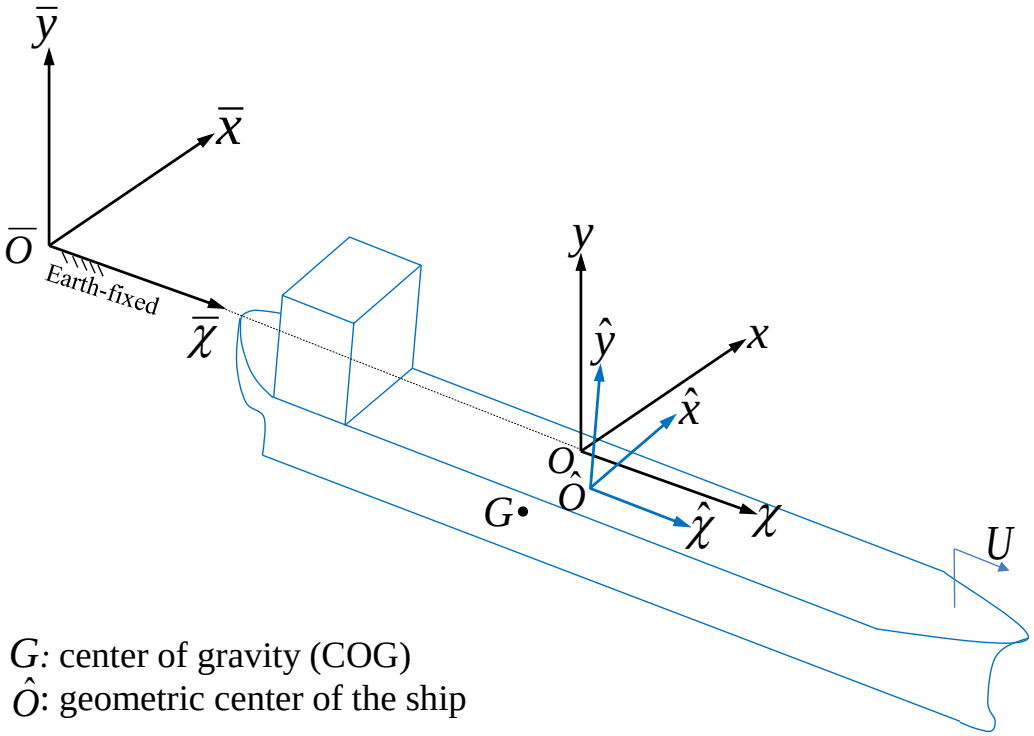

Figure 2.4: Coordinate systems: the earth-fixed coordinates $\overline{O}\overline{x}\overline{y}\overline{\chi}$; the body-fixed coordinates $\hat{O}\hat{x}\hat{y}\hat{\chi}$; and the steadily translating coordinates $Oxy\chi$.

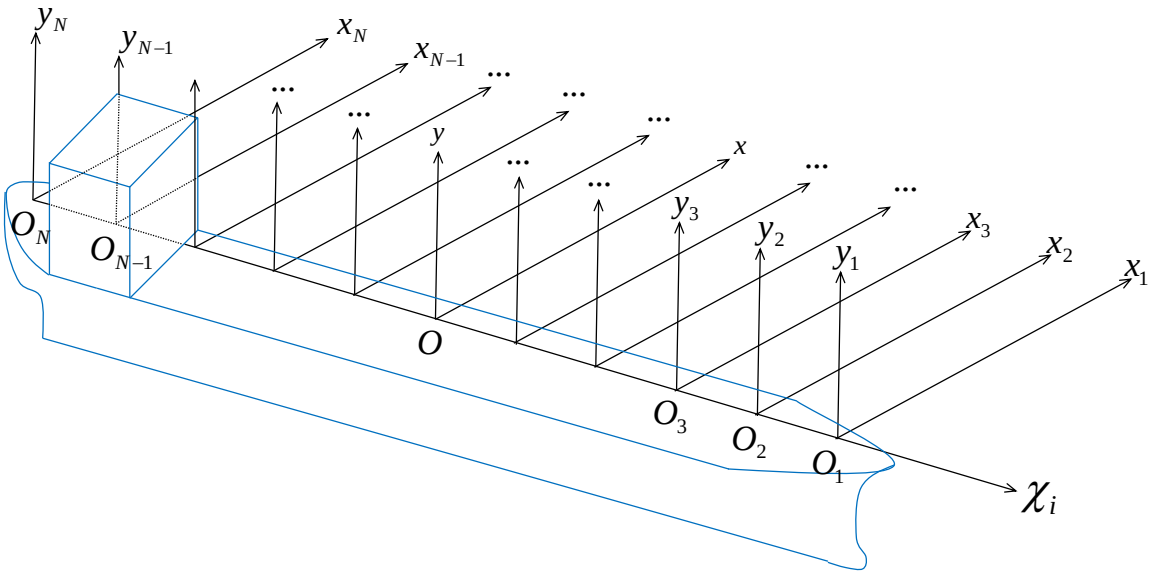

Figure 2.5: Illustration of the translating coordinate system $O\chi xy$ and its sub-systems spaced evenly on the χ axis.

field approximation for a slender body has been previously presented in Yeung, *et al.* (2013).

Let us consider a body of length L, beam B and draft T undergoing steady translation with velocity U in the positive χ direction. Because of the slenderness of the vessel, we assume that the body has geometric ratios of $B/L = \epsilon$ and $B/T = O(1)$, with ϵ being a small parameter. In order to be consistent with the earlier work of FSRVM (say, Seah and Yeung, 2003), we denote the three-dimensional velocity by $\mathbf{V} \equiv (\mathsf{u}, u, v)$, where u (in *sans-serif* font) is the axial component in χ, as opposed to (u, v) being the x, y components in the cross plane. For convenience, we use bold-faced $\mathbf{u}$ to represent the cross-plane velocity *vector* of components (u, v). The vorticity field is denoted by $\mathbf{\Omega} = (\xi,\ \eta,\ \zeta)$. Then, in the absence of any approximation, the velocity field $\mathbf{V}$ and the vorticity field $\mathbf{\Omega}$ satisfy the following:

$$\nabla \cdot \mathbf{V} = 0 \tag{2.2}$$

$$\frac{\tilde{D}\mathbf{V}}{\tilde{D}t} = -\nabla(p/\rho) + \nu\nabla^2\mathbf{V} \tag{2.3}$$

$$\frac{\tilde{D}\mathbf{\Omega}}{\tilde{D}t} = (\mathbf{\Omega}\cdot\nabla)\mathbf{u} + \nu\nabla^2\mathbf{\Omega} \tag{2.4}$$

where $\tilde{D}/\tilde{D}t$, or $\tilde{D}_t$, is the standard three-dimensional material derivative, ρ is the density of the fluid, and ν is the kinematic viscosity.

2.3.1 Near-field governing equations

Based on the slenderness assumption, we introduce the following non-dimensional scales for space, velocity, and vorticity:

$$\left\{\begin{array}{l} \chi' = \chi/L \\ x' = x/B \\ y' = y/B \end{array}\right. \qquad \left\{\begin{array}{l} \mathsf{u}' = \mathsf{u}/(\epsilon U) \\ u' = u/U \\ v' = v/U \end{array}\right. \qquad \left\{\begin{array}{l} \xi' = \xi(\equiv v_x - u_y)B/U \\ \eta' = \eta(\equiv \mathsf{u}_y - v_\chi)L/U \\ \zeta' = \zeta(\equiv u_\chi - \mathsf{u}_x)L/U \end{array}\right. \tag{2.5}$$

where all " $'$ " quantities are assumed to be $O(1)$. In this non-dimensionalization process, the transverse variables are scaled by B and the slenderness ratio of the body results in the smallness of u. This indicates that the perturbed velocity in the axial direction will be unable to satisfy the no-slip boundary condition in the

χ-direction. The time and pressure terms are non-dimensionalized by:

$$t' = tU/B \tag{2.6}$$

$$p' = p/(\rho U^2) \tag{2.7}$$

Based on these non-dimensional terms, Eqns. (2.2) and (2.3) can then be scaled to:

$$\epsilon^2 \frac{\partial \mathsf{u}'}{\partial \chi'} + \nabla'_{2D} \cdot (u', v') = 0 \tag{2.8}$$

$$D'_{t'}\mathsf{u}' = -p'_{\chi'} + \frac{1}{Re_B}\nabla'^2_{2D}\mathsf{u}' + O(\epsilon^2) \tag{2.9}$$

$$D'_{t'}\mathbf{u}' = -\nabla'_{2D}p' + \frac{1}{Re_B}\nabla'^2_{2D}\mathbf{u}' \tag{2.10}$$

In the above equations, we have introduced the following notations in the cross-flow plane:

$$\mathbf{u}' = (u', v') \tag{2.11}$$

$$D'_{t'} = \partial/\partial t' + \mathbf{u}' \cdot \nabla'_{2D} \tag{2.12}$$

where ∇'_{2D} is the 2-D gradient operator with respect to the (x, y)-variables. The Reynolds number is defined to be based on the transverse dimension: $Re_B = (UB)/\nu$.

The dominant vorticity component is found to be in the χ direction, ξ, as can be seen from the following:

$$\mathbf{\Omega}B/U = (\xi',\ \epsilon\eta',\ \epsilon\zeta'). \tag{2.13}$$

Hence, we recall the original vorticity equation (Eqn. (2.4)) for the axial component of the vorticity ξ:

$$\frac{\partial \xi}{\partial t} + (\mathbf{V} \cdot \nabla)\xi = (\vec{\zeta} \cdot \nabla)\mathsf{u} + \nu\nabla^2\xi, \tag{2.14}$$

which can be reduced to the following scaled form:

$$D'_{t'}\xi' = \epsilon^2(\mathbf{\Omega}' \cdot \nabla')\mathsf{u}' + \frac{1}{Re_B}{\nabla'_{2D}}^2\xi'. \tag{2.15}$$

From the above equation, it is seen that the vorticity-stretching term is of higher order, i.e., $O(\epsilon^2)$, following the assumed smallness of the perturbed u. This indicates that the axial vorticity ξ dominates. In summary, Eqns. (2.8), (2.10), and (2.15) state that, to the leading order, the nearfield can be treated as a two-dimensional viscous

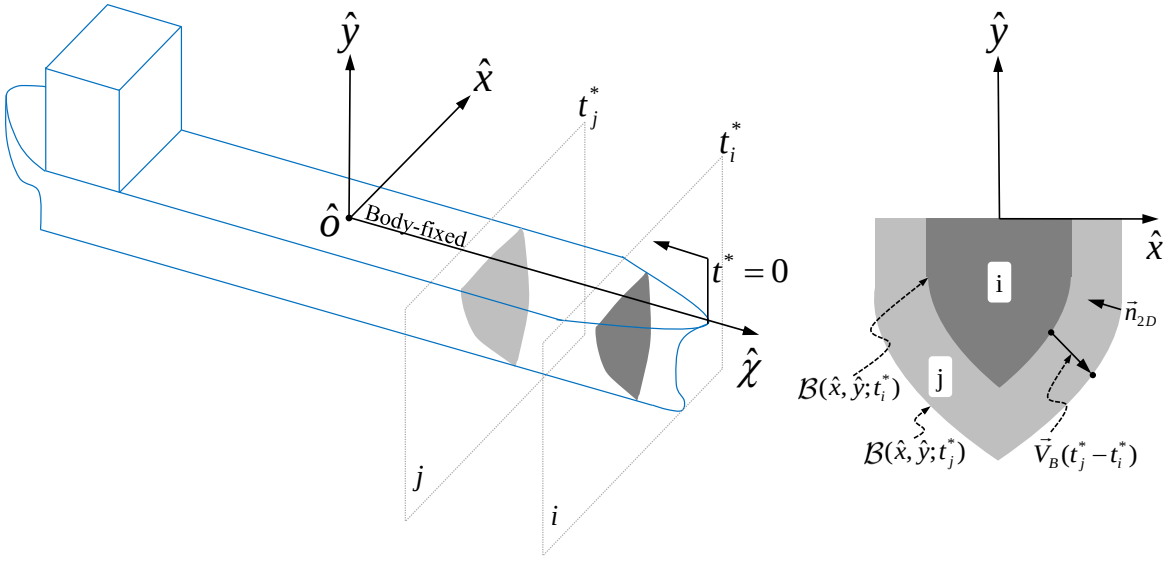

Figure 2.6: Pseudo-time and expansion velocity concepts

flow in the same framework as FSRVM. The next order of solution would involve the neglected perturbed axial flow u, which is governed by Eqn. (2.9).

The body boundary condition in the normal direction of the body surface is given by

$$\mathbf{V} \cdot \mathbf{n}|_{F(x,y,\chi)} = (U, u_b, v_b) \cdot \mathbf{n} = U n_\chi + u_b n_x + v_b n_y, \tag{2.16}$$

where $\mathbf{n}$ is the outward unit normal to the fluid. Here, the three-dimensional surface of the slender body is assumed to be given by $F(x, y, \chi) = 0$, and (u_b, v_b) are the transverse velocities of the body due to the rigid-body motion. Because of the slenderness assumption, the components of $\mathbf{n}$ have different magnitudes: $n_\chi = O(\epsilon)$, $n_x, n_y = O(1)$. The body condition (Eqn. 2.16) can be scaled to:

$$\mathbf{u}' \cdot \vec{n}_{2D}|_{F(x,y,\chi)} = \epsilon n'_\chi + (\frac{V}{U})[u'_b n'_x + v'_b n'_y] + O(\epsilon^2) \tag{2.17}$$

Besides the body-motion induced cross flow in Eqn. (2.17), the cross-plane velocities $\mathbf{u}'$ has, to the next order, an axial-direction contribution that is associated with the longitudinal slope of the body. The forward speed effect is contained in this axial-flow term which can be accounted for (x, y)-plane.

We can utilize the 'pseudo-time' concept of Yeung and Kim (1981) to quantify the change in sectional geometry. Let $t^* = -\chi/U$ denote the pseudo-time variable, which

relates the longitudinal location to the elapsed time required to move from the bow to the longitudinal location χ. This idea is illustrated in Fig. 2.6, in which one can define a two-dimensional boundary $\mathcal{B}$ in the $(\hat{x}, \hat{y})$ space that changes with pseudo-time as the body passes through a plane fixed in space (shaded region in Fig. 2.6).

$$\mathcal{B}(\hat{x}, \hat{y}; t^*) = F(\hat{x}, \hat{y}, \chi = -Ut^*). \tag{2.18}$$

With this definition, it is not difficult to establish the following:

$$\vec{n}_{2D} = \frac{\nabla_\perp \mathcal{B}}{|\nabla_\perp \mathcal{B}|} \tag{2.19}$$

$$Un_\chi = \frac{\partial F/\partial \chi}{|\nabla F|} = \frac{-\partial \mathcal{B}/\partial t^*}{|\nabla_\perp \mathcal{B}|}, \tag{2.20}$$

where $|\nabla F| = |\nabla_\perp \mathcal{B}|$ to $O(\epsilon^2)$ accuracy.

Supplementary to the normal-velocity boundary condition is a no-slip condition in the tangent direction $\vec{\tau}_{2D}$ on the contour of $\mathcal{B}$:

$$\mathbf{u} \cdot \vec{\tau}_{2D}|_{\mathcal{B}} = (u_b, v_b) \cdot \vec{\tau}_{2D.} \tag{2.21}$$

This can be implemented for a viscous-fluid solution in the nearfield. Note that, to the leading order, the no-slip condition for u in the χ direction is not imposed, thus restricting the generation of azimuthal vorticity, such as the formation of ring vortices. This is a limitation of the present theory. To account for these effects, a full three-dimensional theory would have to be adopted.

2.4 Free-surface random-vortex method

The Free-Surface Random Vortex Method (FSRVM) is a Lagrangian-Eulerian formulation of the fluid problem that takes into account the fluid viscosity and the free-surface motion. Various stages of development have taken place and the current capabilities can model forced or free-body motion with any background flow such as incident wave or current. The boundary-value problem is defined in Fig. 2.7, where a vorticity and stream-function formulation is used. The computational domain is bounded by the body ∂D_b, the nonlinear free surface ∂D_f, and the open boundary

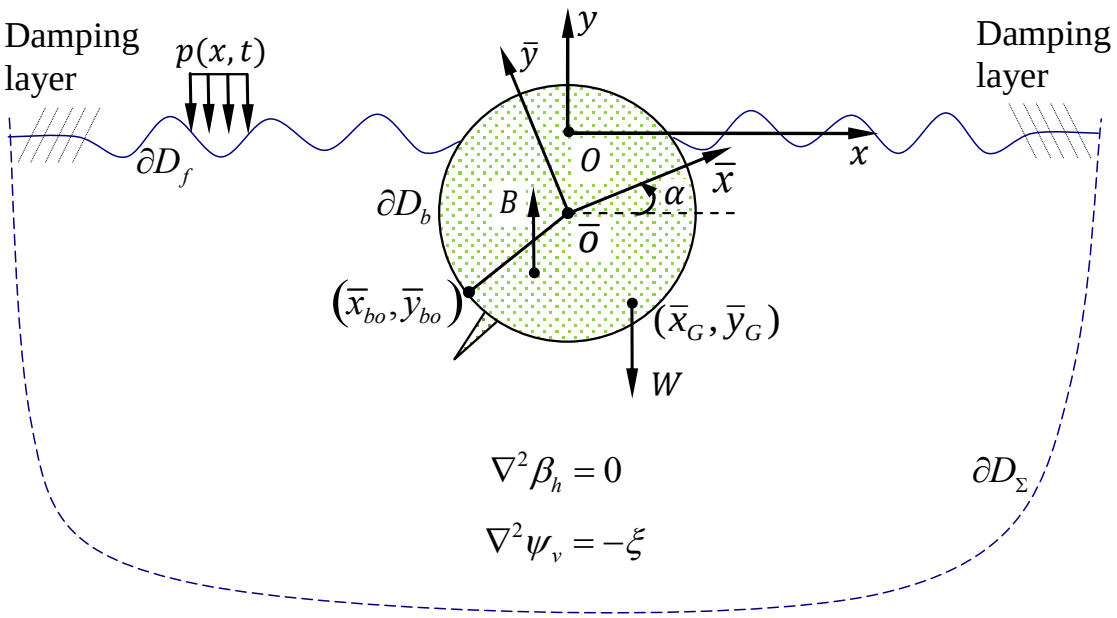

Figure 2.7: Definitions and computational domain D for a rolling body.

∂D_Σ. On the free surface, an oscillating pressure patch can be used to generate incident waves, if needed.

FSRVM is an efficient two-dimensional potential flow solver coupled with the random vortex method to simulate viscous effects. It relies upon a vorticity and stream-function formulation, coupled with nonlinear free surface boundary conditions to model the nonlinear wave-body interactions. The solution is obtained by decomposing the flow field into an irrotational component and a vortical component. The irrotational component of the flow is solved using a complex-variable Cauchy integral method, based on the instantaneous geometry of the computational domain and the associated vorticity field. The vorticity field is solved using the random vortex method of Chorin (1973). In this method, the vorticity field is represented by a large number of vortex blobs that are initially generated to satisfy the no-slip condition on the body. The blobs are subsequently convected away from the body by the solution of the irrotational field and an additional random diffusion component. It is capable of simulating the three degree-of-freedom transient motion as a result of incident waves or an unstable equilibrium condition.

FSRVM was successfully validated by Yeung *et al.* (1996) and Yeung and Cermelli (1998) who compared the results from FSRVM with experimental results of flow around a rolling plate. FSRVM was further validated by Liao and Roddier (1998) in simulating plunging breakers. Hydrodynamic coefficients of rolling rectangular

cylinders were compared using experiments and simulations by Yeung *et al.* (1998). Free motion capability of floating cylinders in a viscous fluid was added by Yeung and Liao (1999) which enabled Roddier *et al.* (2000) to study the induced motion due to waves on rectangular sections with bilge keels. Jiang and Yeung (2012) added the mooring system and electricity modules to FSRVM to study the performance of an asymmetric wave energy converter. FSRVM has proved to be a robust and accurate method for simulating viscous free surface flows with floating and submerged bodies.

The following development of FSRVM has been previously outlined in the review paper by Yeung (2002).

2.4.1 Governing equations and boundary conditions

The flow is assumed to be two-dimensional. Let $\mathbf{u}(\mathbf{x},t) = (u,v)$ be the Eulerian description of the fluid motion at point $\mathbf{x} = (x,y)$. The fluid is assumed to be incompressible and viscous, with positive vorticity $\xi\mathbf{k} = \nabla\times\mathbf{u}$ taken counter-clockwise. The Navier-Stokes equations are the governing equations, which consist of the continuity equation and the momentum equation:

$$\nabla\cdot\mathbf{u} = 0, \tag{2.22}$$

$$\frac{\partial\mathbf{u}}{\partial t} + \mathbf{u}\cdot\nabla\mathbf{u} = -\frac{\nabla p}{\rho} + \nu\nabla^2\mathbf{u} - g\mathbf{j}, \tag{2.23}$$

where ν is the kinematic viscosity coefficient and g gravitational acceleration. In order to solve the velocity field of fluid motion, the FSRVM developed originally by Yeung & Vaidhyanathan (1994) is used. The theoretical formulation of solving the velocity and acceleration fields is summarized with reference to Einstein (1956).

To model viscous effects, the stream function of the flow will be described by a complex velocity potential β in the complex plane $\mathsf{z} = x + \mathsf{i}y$, It has a homogeneous (irrotational) component β_h and a vortical component β_v, so that

$$\beta \equiv \phi + \mathsf{i}\psi = \beta_h + \beta_v, \tag{2.24}$$

$$\beta_h = \phi_h + \mathsf{i}\psi_h, \quad \text{and} \quad \beta_v = \phi_v + \mathsf{i}\psi_v, \tag{2.25}$$

where the velocity vector $\mathbf{u}$ is related to the potential ϕ and the stream function ψ by $(u,v) = (\partial\phi/\partial x, \partial\phi/\partial y) = (\partial\psi/\partial y, -\partial\psi/\partial x)$. The vorticity component, normal to the xy-plane, is defined by $\xi = \partial v/\partial x - \partial u/\partial y$.

Eqns. (2.22)-(2.23) can be reduced to

$$\nabla^2 \beta_h = 0, \tag{2.26}$$

$$\nabla^2 \psi_v = -\xi, \tag{2.27}$$

with the evolution of the vorticity field given by:

$$\frac{D\xi}{Dt} = \nu \nabla^2 \xi. \tag{2.28}$$

Here, $D/Dt = \partial/\partial t + \mathbf{u} \cdot \nabla$ is the material derivative. At any given t, ξ and ψ have to be solved, as to be expected in such vorticity-stream function formulation.

2.4.2 Solution to the vorticity field $\xi(\mathbf{x}, t)$

The vorticity field in the Random Vortex Method (RVM) is approximated by an aggregation of vortex blobs generated on the body surface to satisfy the "no-slip" boundary condition:

$$\xi(\mathbf{x}, t) = \sum_{i=1}^{N(t)} \Gamma_i f(\mathbf{x} - \mathbf{x}_i(t)), \tag{2.29}$$

where N is the number of blobs, with each of circulation Γ_i and located at $\mathbf{x}_i$. f is a pre-specified function that describes the vorticity distribution within the finite-size core of each blob.

The vorticity-transport Eqn. (2.28) is solved by a fractional step method, which consists of a convection step (Eqn. 2.30) and a diffusion step (Eqn. 2.31) at successive *half* time-steps (see Yeung, 2002)

$$\frac{\partial \xi}{\partial t} + (\mathbf{u} \cdot \nabla)\, \xi = 0, \tag{2.30}$$

$$\frac{\partial \xi}{\partial t} = \nu \nabla^2 \xi. \tag{2.31}$$

The diffusion step can be simulated statistically by a random walk algorithm. The convection step uses a fast order $N \log N$ multipole interaction algorithm (Yeung & Vaidhyanathan, 1994).

2.4.3 Solution to the irrotational field β_h

The irrotational component of the flow field is solved using a complex-valued boundary-element method (CVBEM). With reference to Fig. 2.7, the conditions for $\beta_h = \phi_h + \mathsf{i}\psi_h$ are:

$$\frac{D\mathsf{z}}{Dt} = \mathsf{w}^*(\mathsf{z}, t), \tag{2.32}$$

$$\frac{D\phi_h}{Dt} = -\frac{D\phi_v}{Dt} - \frac{p}{\rho} + \frac{1}{2}\mathsf{w}\mathsf{w}^* - gy \quad \text{on } \partial D_f, \tag{2.33}$$

$$\psi_h = -\psi_v + \dot{x}_b(t)\bar{y} - \dot{y}_b(t)\bar{x} - \frac{1}{2}\dot{\alpha}R_b^2 \quad \text{on } \partial D_b, \tag{2.34}$$

$$\frac{\partial\phi_h}{\partial t} = -\frac{\partial\phi_v}{\partial t} \quad \text{on } \partial D_\Sigma, \tag{2.35}$$

where the complex velocity $\mathsf{w} = u - \mathsf{i}v$, with * denoting complex conjugate and $R_b^2 \equiv {x_b}^2 + \bar{y}_{bo}^2$. In the body boundary condition (Eqn. 2.34), we have allowed the general case of three degrees of freedom, with the body origin $\overline{O} = (x_b(t), y_b(t))$ and the roll angle $\alpha(t)$ about $\overline{O}$ considered prescribed. In the present application, the translational modes are suppressed. If $\alpha(t)$ is the free motion excited by waves, rather than prescribed, an equation of motion is needed, as explained in Section 2.4.

To absorb waves travelling towards the ends of the domain, the damping algorithm based on Israeli & Orszag (1981) is used to modify Eqn. (2.33) in the damping region. The boundary conditions in Eqns. (2.33)–(2.35) are used to set up the Cauchy integral equation for β_h which can solve for either ϕ_h or ψ_h on the fluid boundary when its conjugate part is specified:

$$\pi\mathsf{i}\beta_h(\mathsf{z}) - \fint_{\partial D} \frac{\beta_h(\zeta)}{\zeta - \mathsf{z}} d\zeta = 0 \ \text{ for } \mathsf{z} \in \partial D. \tag{2.36}$$

Expressions for $D\phi_v/Dt$ and $\partial\phi_v/\partial t$ are needed for Eqns. (2.33) and (2.35), which can be obtained from the real part of the time derivatives of β_v. If the motion of the body is unknown, an integral equation for $\partial\beta_h/\partial t$, similar to Eqn. (2.36) can be developed using information of $\partial\beta_v/\partial t$. Solution of the integral equation (2.36) follows then the published techniques of Grosenbaugh & Yeung (1989).

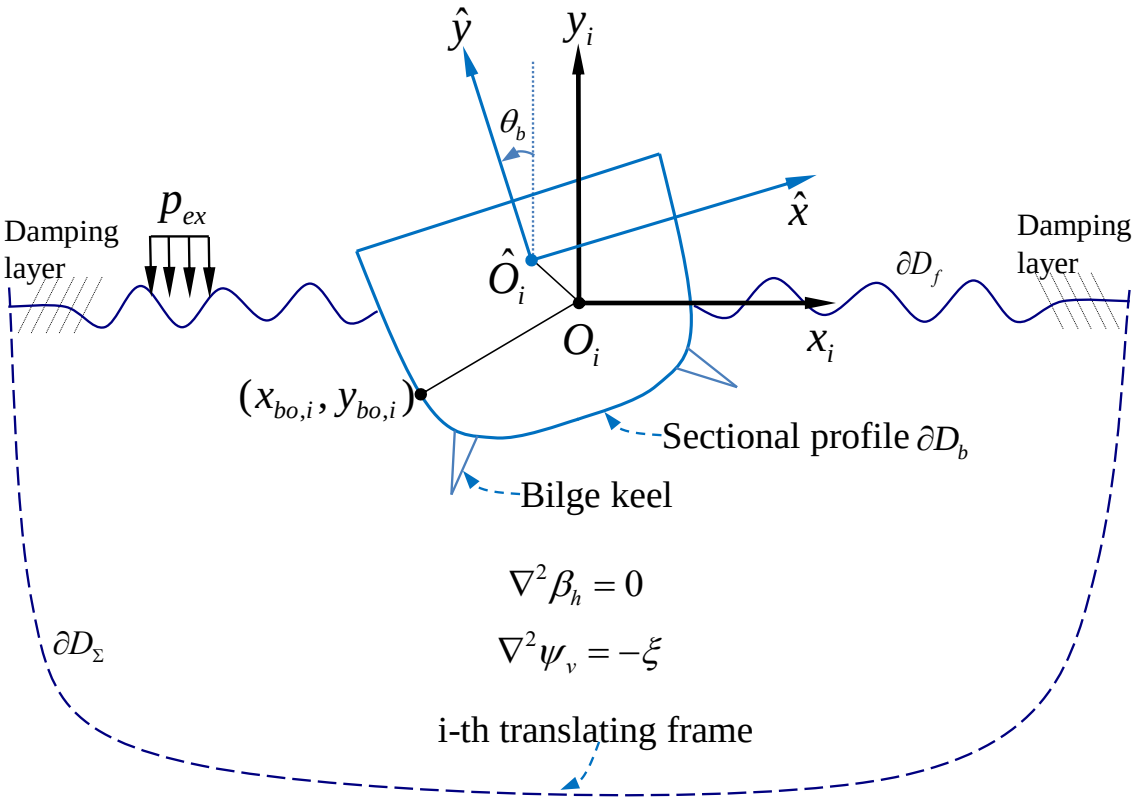

Figure 2.8: FSRVM model in a two-dimensional computational plane.

2.5 Relation between global and sectional motion

A relation between the reference motion of O and sub-system motion of O_i is needed to build the global equations of motion of the hull.

Figure 2.8 shows an example of the FSRVM model in a two-dimensional computational plane. The i-th station of a vessel translates and rotates in this fluid domain according to the the global motion of the point O. Point $\hat{O}_i$ is the geometrical center of the local section. Its location with respect to the i-th translating sub-frame is denoted by $(x_{\hat{O}_i}, y_{\hat{O}_i})$.

In order to establish the dynamic coupling between the fluid and a specific section of the ship, the instantaneous sectional body profile and the sectional motion on the body are needed to obtain the boundary conditions. A point on the i-th section, with initial coordinates $(\hat{x}_{bo,i}, \hat{y}_{bo,i})$ on the body, will have new coordinates $(x_{bo,i}, y_{bo,i})$ in

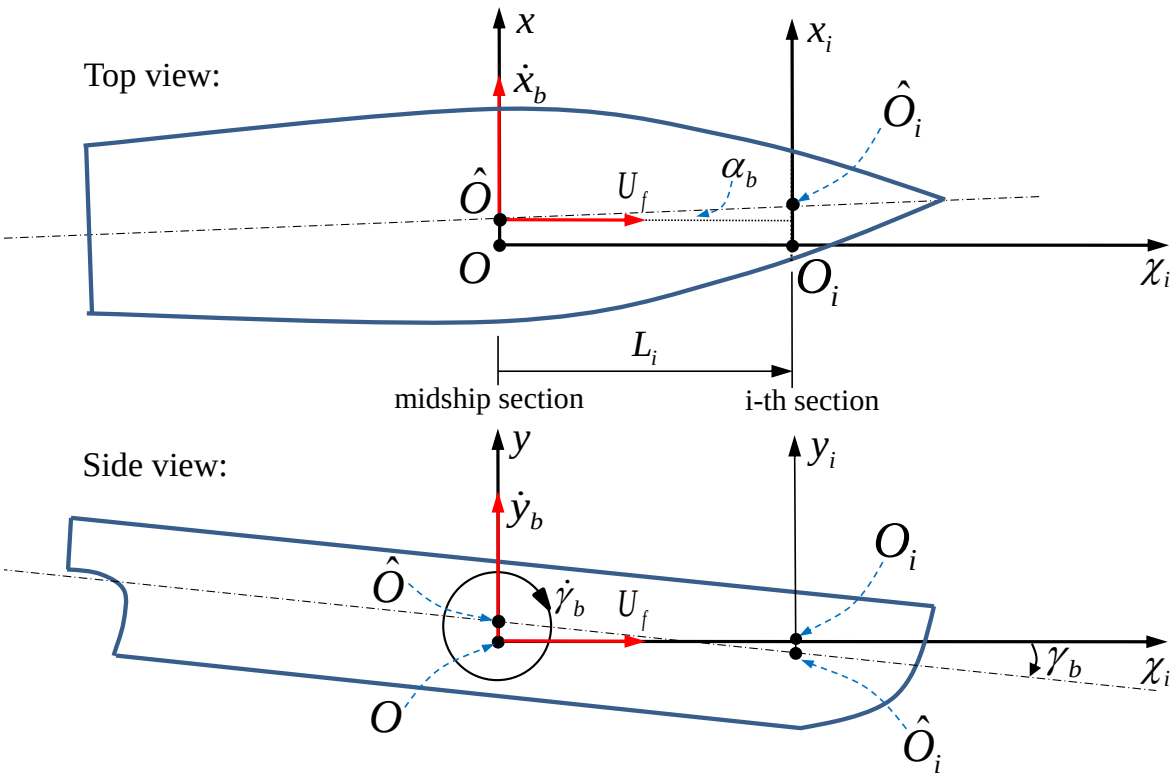

Figure 2.9: Relation between global motion of $\hat{O}$ and sectional motion of $\hat{O}_i$ with positive yaw and pitch angles.

the $O_i x_i y_i$ system:

$$\begin{bmatrix} x_{bo,i} \\ y_{bo,i} \end{bmatrix} = \begin{bmatrix} \cos\theta_b & -\sin\theta_b \\ \sin\theta_b & \cos\theta_b \end{bmatrix} \begin{bmatrix} \hat{x}_{bo,i} \\ \hat{y}_{bo,i} \end{bmatrix} + \begin{bmatrix} x_{\hat{O}_i} \\ y_{\hat{O}_i} \end{bmatrix} \tag{2.37}$$

where $(x_{\hat{O}_i}, y_{\hat{O}_i})$ can be obtained from the motion of the reference point $\hat{O}$ of the vessel. Note that θ_b is the Euler roll angle about the χ-axis.

The hull section in each computational plane has, evidently, only three degrees of freedom (sway, heave and roll). Since the actual vessel has six degrees of freedom, the sectional motion of sway, heave and roll are directly related to the global motion of the $\hat{}$ system. As the influence of surge motion (in the presence of forward velocity) is modeled by the concept of expansion velocity (see Yeung *et al.*, 2013), global pitch and yaw motion leads to sectional sway and heave motion. The following can be deduced in a straightforward manner: Per Fig. 2.9, a positive (counterclockwise from above) yaw of the vessel, α_b, induces sway of sections from bow to stern, while a positive (clockwise from starboard side) global pitch, γ_b, induces heave of sections

from bow to stern. Hence, with the contribution of global yaw and pitch, the position and rotation of the i-th sectional center $(x_{\hat{O}_i}, y_{\hat{O}_i})$ can be expressed in the following form:

$$\begin{cases} x_{\hat{O}_i} = x_b + L_i \ \tan\alpha_b \\ y_{\hat{O}_i} = y_b - L_i \ \tan\gamma_b \\ \theta_{\hat{O}_i} = \theta_b \end{cases} \tag{2.38}$$

where x_b, y_b, θ_b, γ_b, and α_b denote the sway, heave, roll, pitch, and yaw displacements of the vessel with respect to the translating frame. L_i denotes the distance from i-th section to the midship section, with bow sections positive and stern sections negative.

A positive (clockwise from starboard side) pitch velocity, $\dot{\gamma}_b$, is perceived to be negative heave velocities of sections in the positive χ-direction. In this work, the yaw velocity is assumed to be zero, so the sway velocity has no contribution from the yaw velocity. Hence, the two-dimensional rigid body velocity $(\dot{x}_{\hat{O}_i}, \dot{y}_{\hat{O}_i}, \dot{\theta}_{\hat{O}_i})$ can be expressed in the following form:

$$\begin{cases} \dot{x}_{\hat{O}_i} = \dot{x}_b \\ \dot{y}_{\hat{O}_i} = \dot{y}_b - L_i \ \dot{\gamma}_b \\ \dot{\theta}_{\hat{O}_i} = \dot{\theta}_b \end{cases} \tag{2.39}$$

Similarly, the two-dimensional rigid body acceleration $(\ddot{x}_{\hat{O}_i}, \ddot{y}_{\hat{O}_i}, \ddot{\theta}_{\hat{O}_i})$ can be expressed in the following form:

$$\begin{cases} \ddot{x}_{\hat{O}_i} = \ddot{x}_b \\ \ddot{y}_{\hat{O}_i} = \ddot{y}_b - L_i \ \ddot{\gamma}_b \\ \ddot{\theta}_{\hat{O}_i} = \ddot{\theta}_b \end{cases} \tag{2.40}$$

Here, we need to note that the computational plane $O_i x_i y_i$ is fixed in space, while the body profile ∂D_b, moves with the vessel. Due to the pitch angle γ_b and constant yaw angle α_b, the body contour is not perfectly parallel with the computational plane. However, we know that the pitch and yaw angles of the a slender ship are always small. However, the accuracy of the results is expected to decrease as either large pitch angle or yaw angle ($> 15°$) happens.

2.6 Equations of motion

In order to simulate the free response of the floating body, the equations of motion must be written and solved with respect to one reference point in a coordinate system. Normally, equations of motion are written about the center of gravity (COG) of a body. Alternatively, it is preferable to develop these equations at the referenced coordinate origin O, rather than G, as the former is the geometric center.

In this section, it is more convenient to obtain the equations of motion with respect to point G first (see Fig. 2.4) and then transform the results to O in the steadily translating coordinate system.

Newton's second law with respect to the COG translating frame for the 6-DOF motions can be easily expressed as:

$$\begin{bmatrix} M_b & 0 & 0 & 0 & 0 & 0 \\ 0 & M_b & 0 & 0 & 0 & 0 \\ 0 & 0 & M_b & 0 & 0 & 0 \\ 0 & 0 & 0 & \tilde{I}_{\chi\chi} & 0 & 0 \\ 0 & 0 & 0 & 0 & \tilde{I}_{xx} & \tilde{I}_{xy} \\ 0 & 0 & 0 & 0 & \tilde{I}_{xy} & \tilde{I}_{yy} \end{bmatrix} \begin{bmatrix} \ddot{\chi}_G \\ \ddot{x}_G \\ \ddot{y}_G \\ \ddot{\theta}_G \\ \ddot{\gamma}_G \\ \ddot{\alpha}_G \end{bmatrix} = \begin{bmatrix} \tilde{F}_\chi \\ \tilde{F}_x \\ \tilde{F}_y \\ \tilde{M}_\chi \\ \tilde{M}_x \\ \tilde{M}_y \end{bmatrix} \tag{2.41}$$

where M_b is the body mass. $(\ddot{\chi}_G,\ \ddot{x}_G,\ \ddot{y}_G)$ and $(\ddot{\theta}_G,\ \ddot{\gamma}_G,\ \ddot{\alpha}_G)$ denote the translational and angular accelerations (the Euler's angles) of the body. The tilde $\tilde{}$ over each variable in Eqn. (2.41) denotes that the value of this variable is calculated about point G in the translating coordinate system

The moments acting on the body measured at point G can be obtained from the moments measured at point O by:

$$\vec{M}_G = \vec{M}_O - \vec{R}_G \times \vec{F}_G = \vec{M}_O - \vec{R}_G \times (M_b \vec{a}_G) \tag{2.42}$$

where $\vec{F}_G$ and $\vec{M}_G$ denote the force and moment vectors about point G. $\vec{M}_O$ denotes the moment vector about point O. $\vec{R}_G (\doteq (\chi_G, x_G, y_G)^T)$ denotes the position G in the translating frame.

Written in a matrix form, Eqn. (2.42) can be expressed as:

$$\begin{bmatrix} \tilde{M}_\chi \\ \tilde{M}_x \\ \tilde{M}_y \end{bmatrix} = \begin{bmatrix} M_\chi \\ M_x \\ M_y \end{bmatrix} - \begin{bmatrix} M_b(x_G\ddot{y}_G - y_G\ddot{x}_G) \\ M_b(y_G\ddot{\chi}_G - \chi_G\ddot{y}_G) \\ M_b(\chi_G\ddot{x}_G - x_G\ddot{\chi}_G) \end{bmatrix} \tag{2.43}$$

According to basic kinematic concepts, the angular accelerations and the forces measured at point G and point O will have the same values. So,

$$\begin{cases} \ddot{\theta}_G = \ddot{\theta}_b \\ \ddot{\gamma}_G = \ddot{\gamma}_b \\ \ddot{\alpha}_G = \ddot{\alpha}_b \end{cases} \quad \& \quad \begin{cases} \tilde{F}_\chi = F_\chi \\ \tilde{F}_x = F_x \\ \tilde{F}_y = F_y \end{cases} \tag{2.44}$$

Substituting Eqn. (2.43) and Eqn. (2.44) in Eqn. (2.41) gives:

$$\begin{bmatrix} M_b & 0 & 0 & 0 & 0 & 0 \\ 0 & M_b & 0 & 0 & 0 & 0 \\ 0 & 0 & M_b & 0 & 0 & 0 \\ 0 & 0 & 0 & \tilde{I}_{\chi\chi} & 0 & 0 \\ 0 & 0 & 0 & 0 & \tilde{I}_{xx} & \tilde{I}_{xy} \\ 0 & 0 & 0 & 0 & \tilde{I}_{xy} & \tilde{I}_{yy} \end{bmatrix} \begin{bmatrix} \ddot{\chi}_G \\ \ddot{x}_G \\ \ddot{y}_G \\ \ddot{\theta}_G \\ \ddot{\gamma}_G \\ \ddot{\alpha}_G \end{bmatrix} + \begin{bmatrix} 0 \\ 0 \\ 0 \\ M_b(x_G\ddot{y}_G - y_G\ddot{x}_G) \\ M_b(y_G\ddot{\chi}_G - \chi_G\ddot{y}_G) \\ M_b(\chi_G\ddot{x}_G - x_G\ddot{\chi}_G) \end{bmatrix} = \begin{bmatrix} F_\chi \\ F_x \\ F_y \\ M_\chi \\ M_x \\ M_y \end{bmatrix} \tag{2.45}$$

We assume that the vessel moves with constant forward speed (could be zero) and constant yaw angle. Substituting Eqns. (2.43) and (2.44) in Eqn. (2.41) and removing the surge and yaw degrees of freedom from the 6-DOF equations of motion, we obtain the following 4-DOF equations of motion:

$$\begin{bmatrix} M_b & 0 & 0 & 0 \\ 0 & M_b & 0 & 0 \\ 0 & 0 & \tilde{I}_{\chi\chi} & 0 \\ 0 & 0 & 0 & \tilde{I}_{xx} \end{bmatrix} \begin{bmatrix} \ddot{x}_G \\ \ddot{y}_G \\ \ddot{\theta}_b \\ \ddot{\gamma}_b \end{bmatrix} + \begin{bmatrix} 0 \\ 0 \\ M_b(x_G\ddot{y}_G - y_G\ddot{x}_G) \\ M_b(y_G\ddot{\chi}_G - \chi_G\ddot{y}_G) \end{bmatrix} = \begin{bmatrix} F_x \\ F_y \\ M_\chi \\ M_x \end{bmatrix} \tag{2.46}$$

Per basic kinematics, the linear acceleration at point G, $\vec{a}_G$, can be expressed in terms of the acceleration at point O, $\vec{a}_b$, by the following equation:

$$\vec{a}_G = \vec{a}_b + \ddot{\theta}_b\vec{i} \times \vec{R}_G + \ddot{\gamma}_b\vec{j} \times \vec{R}_G + \dot{\theta}_b\vec{i} \times (\dot{\theta}_b\vec{i} \times \vec{R}_G) + \dot{\gamma}_b\vec{j} \times (\dot{\gamma}_b\vec{j} \times \vec{R}_G) \tag{2.47}$$

where $\vec{a}_G \doteq (\ddot{\chi}_G, \ddot{x}_G, \ddot{x}_G)^T$ and $\vec{a}_b \doteq (\ddot{\chi}_b, \ddot{x}_b, \ddot{x}_b)^T$. The second and third terms in the R.H.S. of the equation, $\ddot{\theta}_b\vec{i} \times \vec{R}_G$ and $\ddot{\gamma}_b\vec{j} \times \vec{R}_G$, represent the accelerations due

to the roll and pitch angular accelerations. The last two terms, $\dot{\theta}_b\vec{i} \times (\dot{\theta}_b\vec{i} \times \vec{R}_G)$ and $\dot{\gamma}_b\vec{j} \times (\dot{\gamma}_b\vec{j} \times \vec{R}_G)$, represent the accelerations due to the centrifugal accelerations. Written in the vector form, Eqn. (2.47) becomes:

$$\begin{bmatrix} \ddot{\chi}_G \\ \ddot{x}_G \\ \ddot{y}_G \end{bmatrix} = \begin{bmatrix} \ddot{\chi}_b \\ \ddot{x}_b \\ \ddot{y}_b \end{bmatrix} + \begin{bmatrix} 0 \\ -\ddot{\theta}_b y_G \\ \ddot{\theta}_b x_G \end{bmatrix} + \begin{bmatrix} \ddot{\gamma}_b y_G \\ 0 \\ -\ddot{\gamma}_b \chi_G \end{bmatrix} + \begin{bmatrix} 0 \\ -\dot{\theta}_b^2 x_G \\ -\dot{\theta}_b^2 y_G \end{bmatrix} + \begin{bmatrix} -\dot{\gamma}_b^2 \chi_G \\ 0 \\ -\dot{\gamma}_b^2 y_G \end{bmatrix} \quad (2.48)$$

With the use of Eqn. (2.48), the final 4-DOF equations of motion about point O are:

$$\begin{bmatrix} M_b & 0 & -M_b y_G & 0 \\ 0 & M_b & M_b x_G & -M_b \chi_G \\ -M_b y_G & M_b x_G & I_{\chi\chi} & -M_b \chi_G x_G \\ 0 & -M_b \chi_G & -M_b \chi_G x_G & I_{xx} \end{bmatrix} \begin{bmatrix} \ddot{x}_b \\ \ddot{y}_b \\ \ddot{\theta}_b \\ \ddot{\gamma}_b \end{bmatrix}$$

$$= \begin{bmatrix} F_x \\ F_y \\ M_\chi \\ M_x \end{bmatrix} + \begin{bmatrix} M_b x_G \dot{\theta}_b^2 \\ M_b y_G (\dot{\theta}_b^2 + \dot{\gamma}_b^2) \\ M_b x_G y_G \dot{\gamma}_b^2 \\ -M_b \chi_G y_G \dot{\theta}_b^2 \end{bmatrix} \quad (2.49)$$

where $I_{\chi\chi}$ and I_{xx} denote the roll and pitch moments of inertia about point O, respectively.

2.7 Global forces and moments

The 4-DOF equation with respect to the body center has been obtained in the previous section. In order to solve for the accelerations at the reference point, the global forces and moments are needed to know. In the next section, the method of calculating the global forces and moments will be introduced.

2.7.1 Relation between global and sectional loads

Based on the slender-ship theory, force and moment contributions from each plane are combined in a strip-wise manner to obtain the overall force on the vessel. The total external forces and moments acting on the vessel with respect to the translating coordinate frame are given by:

$$\begin{cases} F_x = \sum_{i=1}^{N} F_{1,i} \\ F_y = \sum_i F_{2,i} - M_b g \\ M_\chi = \sum_i F_{3,i} - M_b g \ x_G \\ M_x = \sum_i F_{2,i} L_i + M_b g \ \chi_G \end{cases} \tag{2.50}$$

where $F_{1,i}$ and $F_{2,i}$ denote the lateral and vertical forces acting on the i-th station. $F_{3,i}$ denotes the sectional roll moment. Apart from the first equation, showing the limits of the summation over i, we will henceforth adopt the simplified notation of $\sum_i$ to mean the same limits of i. The sectional loads can be obtained by integrating the pressure over the wetted sectional body contour ∂D_b,

$$\begin{cases} F_{1,i} = \int\limits_{\partial D_b} p \ n_x ds \\ F_{2,i} = \int\limits_{\partial D_b} p \ n_y ds \\ F_{3,i} = \int\limits_{\partial D_b} p(n_x y - n_y x) ds. \end{cases} \tag{2.51}$$

where p denotes the fluid pressure that can be calculated by using Euler's integral,

$$\frac{p}{\rho} = -(\frac{\partial \phi_h}{\partial t} + \frac{\partial \phi_v}{\partial t}) - \frac{1}{2}|\vec{u}|^2 - gy. \tag{2.52}$$

2.7.2 Dynamic coupling between fluid and body

Solution of the term $\partial\phi_h/\partial t$ in Eqn. (2.52) needs the boundary condition $\partial\psi_h/\partial t$, which involves the unknown accelerations $\ddot{x}_b$, $\ddot{y}_b$, and $\ddot{\alpha}_b$. So, Eqns. (2.49) is a set of implicit second-order differential equations. In order to solve the accelerations, a manner similar to Vinje & Brevig (1980) is used to obtain the explicit expressions for $\ddot{\alpha}$. The procedure is briefly described here, but more details can be found in Liao (2000).

On the body contour ∂D_b (see Fig. 2.8), the boundary condition of $\partial\phi_h/\partial t$ is

$$\begin{aligned}\frac{\partial\psi_h}{\partial t} &= \ddot{x}_{\hat{O}_i} y_{bo,i} - \ddot{y}_{\hat{O}_i} x_{bo,i} - \frac{1}{2}\ddot{\theta}_{\hat{O}_i} R^2_{bo,i} \\ &\quad -\frac{\partial\psi_v}{\partial t} + \dot{x}_b v_{bo,i} - \dot{y}_b u_{bo,i} + \dot{\theta}_{\hat{O}_i}[(\dot{x}_b - u_{bo,i})x_{bo,i} + (\dot{y}_b - v_{bo,i})y_{bo,i}]. \qquad (2.53)\end{aligned}$$

where $x_{bo,i}, y_{bo,i}$ denotes the coordinate of a body node. $R^2_{bo,i} = x^2_{bo,i} + y^2_{bo,i}$.

Following Vinje & Brevig (1980), we let the boundary conditions be written as

$$\frac{\partial\psi_h}{\partial t} = \frac{\partial\psi_1}{\partial t}\ddot{x}_{\hat{O}_i} + \frac{\partial\psi_2}{\partial t}\ddot{y}_{\hat{O}_i} + \frac{\partial\psi_3}{\partial t}\ddot{\theta}_{\hat{O}_i} + \frac{\partial\psi_4}{\partial t} \quad \text{on } \partial D_b, \qquad (2.54)$$

$$\frac{\partial\phi_h}{\partial t} = -\frac{\partial\phi_v}{\partial t} - \frac{p}{\rho} - \frac{1}{2}|\nabla\phi|^2 - gy \equiv \frac{\partial\phi_4}{\partial t} \quad \text{on } \partial D_f, \qquad (2.55)$$

$$\frac{\partial\phi_h}{\partial t} = -\frac{\partial\phi_v}{\partial t} \equiv \frac{\partial\phi_4}{\partial t} \quad \text{on } \partial D_\Sigma. \qquad (2.56)$$

Thus, four new analytic functions have been introduced for $\partial\beta_h/\partial t$ and can be written as

$$(\frac{\partial\phi_h}{\partial t} + \mathsf{i}\frac{\partial\psi_h}{\partial t}) = \beta_{1t}\ddot{x}_{\hat{O}_i} + \beta_{2t}\ddot{y}_{\hat{O}_i} + \beta_{3t}\ddot{\theta}_{\hat{O}_i} + \beta_{4t}. \qquad (2.57)$$

Equations (2.54)–(2.57) show that β_{1t}, β_{2t}, and β_{3t} can be related to the unit acceleration of the body, and β_{4t} is related to the solution of the velocity field and the generation of surface waves. The boundary-value problems for β_{1t}, β_{2t}, and β_{3t} are:

$$\frac{\partial\phi_1}{\partial t} = 0 \quad \text{on } \partial D_f \text{ and } \partial D_\Sigma, \quad \frac{\partial\psi_1}{\partial t} = y_{bo,i} \quad \text{on } \partial D_b, \qquad (2.58)$$

$$\frac{\partial\phi_2}{\partial t} = 0 \quad \text{on } \partial D_f \text{ and } \partial D_\Sigma, \quad \frac{\partial\psi_2}{\partial t} = -x_{bo,i} \quad \text{on } \partial D_b, \qquad (2.59)$$

$$\frac{\partial\phi_3}{\partial t} = 0 \quad \text{on } \partial D_f \text{ and } \partial D_\Sigma, \quad \frac{\partial\psi_3}{\partial t} = -\frac{1}{2}R^2_{bo,i} \quad \text{on } \partial D_b. \qquad (2.60)$$

The boundary-value problem of β_{4t} is defined by

$$\frac{\partial \phi_4}{\partial t} = -\frac{\partial \phi_v}{\partial t}, \tag{2.61}$$

$$\frac{\partial \phi_4}{\partial t} = -\frac{\partial \phi_v}{\partial t} - \frac{p}{\rho} - \frac{1}{2}|\nabla\phi|^2 - gy, \tag{2.62}$$

$$\frac{\partial \psi_4}{\partial t} = -\frac{\partial \psi_v}{\partial t} + \dot{x}_{\hat{O}_i} v_{bo,i} - \dot{y}_{\hat{O}_i} u_{bo,i} + \dot{\theta}_{\hat{O}_i}[(\dot{x}_{\hat{O}_i} - u_{bo,i})x_{bo,i} + (\dot{y}_{\hat{O}_i} - v_{bo,i})y_{bo,i}], \tag{2.63}$$

for $\mathsf{z} \in \partial D_\Sigma$, ∂D_f, and ∂D_b, respectively. None of these four boundary-value problems depend on $(\ddot{x}_{\hat{O}_i}, \ddot{y}_{\hat{O}_i}, \ddot{\theta}_{\hat{O}_i})$. Similar to the integral equation (2.36) for β_h, four additional integral equations can be set up for β_{1t}, β_{2t}, β_{3t}, and β_{4t} according to the boundary conditions given in Eqns. (2.58)–(2.63).

Based on the solutions of β_{1t}, β_{2t}, β_{3t}, and β_{4t}, a set of coefficients $A_{jk,i}$ and $A_{4k,i}$ can be defined for the i-th section as:

$$A_{jk,i}(t) = \rho \int_{\partial D_b} \frac{\partial \phi_k}{\partial t} n_j ds, \ j,k = 1,2,3, \tag{2.64}$$

$$A_{4k,i}(t) = -\rho \int_{\partial D_b} (\frac{\partial \phi_4}{\partial t} + \frac{\partial \phi_v}{\partial t} + \frac{1}{2}|\nabla\phi|^2 + gy) n_k ds, \ k=1,2,3. \tag{2.65}$$

where $A_{jk,i}, \ j,k = 1,2,3$ represent the sectional hydrodynamic added mass or added moment of inertia; $A_{4k,i}, \ k = 1,2,3$ represent the summation of sectional hydrodynamic damping and hydrostatic restoring loads.

So the total hydrostatic and hydrodynamic forces and moment acting on the i-th section with respect to the corresponding translating frame reference will be as following:

$$\begin{cases} F_{1,i} = (A_{41,i} - A_{11,i}\ddot{x}_{\hat{O}_i} - A_{12,i}\ddot{y}_{\hat{O}_i} - A_{13,i}\ddot{\theta}_{\hat{O}_i})\Delta L \\ F_{2,i} = (A_{42,i} - A_{21,i}\ddot{x}_{\hat{O}_i} - A_{22,i}\ddot{y}_{\hat{O}_i} - A_{23,i}\ddot{\theta}_{\hat{O}_i})\Delta L \\ F_{3,i} = (A_{43,i} - A_{31,i}\ddot{x}_{\hat{O}_i} - A_{32,i}\ddot{y}_{\hat{O}_i} - A_{33,i}\ddot{\theta}_{\hat{O}_i})\Delta L \end{cases} \tag{2.66}$$

where ΔL denotes the distance between any two adjacent sections.

2.7.3 Global forces and moments and final EOM

Substitution of the sectional forces (Eqn. 2.66) and sectional acceleration (Eqn. 2.40) in Eqn. (2.50) gives the following global forces and moments:

$$\begin{cases} F_x = \sum_i (A_{41,i} - A_{11,i}\ddot{x}_b - A_{12,i}(\ddot{y}_b - L_i\ddot{\gamma}_b) - A_{13,i}\ddot{\theta}_b)\Delta L \\ F_y = \sum_i (A_{42,i} - A_{21,i}\ddot{x}_b - A_{22,i}(\ddot{y}_b - L_i\ddot{\gamma}_b) - A_{23,i}\ddot{\theta}_b)\Delta L - M_b g \\ M_\chi = \sum_i (A_{43,i} - A_{31,i}\ddot{x}_b - A_{32,i}(\ddot{y}_b - L_i\ddot{\gamma}_b) - A_{33,i}\ddot{\theta}_b)\Delta L - M_b g\ x_G \\ M_x = \sum_i (-A_{42,i} + A_{21,i}\ddot{x}_b + A_{22,i}(\ddot{y}_b - L_i\ddot{\gamma}_b) + A_{23,i}\ddot{\theta}_b)L_i\Delta L + M_b g\ \chi_G \end{cases} \tag{2.67}$$

With the use of the above forces and moments, the final 4-DOF equations of motion can be expressed as:

$$\begin{bmatrix} (B_{11}+M_b) & B_{12} & (B_{13}-M_b y_G) & -B_{14} \\ B_{21} & (B_{22}+M_b) & (B_{23}+M_b x_G) & (-B_{24}-M_b\chi_G) \\ (B_{31}-M_b y_G) & (B_{32}+M_b x_G) & (B_{33}+I_{\chi\chi}) & (-B_{34}-M_b\chi_G x_G) \\ -B_{41} & (-B_{42}-M_b\chi_G) & (-B_{43}-M_b\chi_G x_G) & (B_{44}+I_{xx}) \end{bmatrix} \begin{bmatrix} \ddot{x}_b \\ \ddot{y}_b \\ \ddot{\theta}_b \\ \ddot{\gamma}_b \end{bmatrix}$$

$$= \begin{bmatrix} W_{41} + M_b x_G \dot{\theta}_b^2 \\ W_{42} + M_b y_G(\dot{\theta}_b^2 + \dot{\gamma}_b^2) - M_b g \\ W_{43} - M_b g x_G + M_b x_G y_G \dot{\gamma}_b^2 \\ -W_{44} - M_b\chi_G y_G \dot{\theta}_b^2 + M_b g \chi_G \end{bmatrix} \tag{2.68}$$

where the coefficients B_{jk} and W_{jk} are defined by:

$$\begin{cases} B_{jk} = \sum_i A_{jk,i}\Delta L, j,k = 1,2,3 \\ B_{j4} = \sum_i A_{j2,i}L_i\Delta L, j = 1,2,3 \\ B_{4k} = \sum_i A_{2k,i}L_i\Delta L, k = 1,2,3 \\ W_{4j} = \sum_i A_{4j,i}\Delta L, j = 1,2,3 \\ B_{44} = \sum_i A_{22,i}L_i^2\Delta L \\ W_{44} = \sum_i A_{42,i}L_i\Delta L \end{cases} \tag{2.69}$$

Equation (2.68) completely describes the full nonlinear dynamic coupling between the fluid and the three-dimensional vessel, which can be solved explicitly to yield $(\ddot{x}_b, \ddot{y}_b, \ddot{\theta}_b, \ddot{\gamma}_b)$ at any given time t.

Further, with the acceleration being solved, the velocity and position can be integrated in time to update the location of the body. Then the kinematic and dynamic conditions are used to update the boundary nodes. A new set of boundary conditions is available for the next time step. The time-domain simulation for free motion can now be achieved.

2.8 Computational procedure and time evolution

In this section, we will discuss the numerical procedure used in SSFSRVM to solve for the accelerations, as well as the preparation of all the terms required in these equations.

Figure 2.10 shows the general numerical procedure of the entire program, including three main modules: Initial module, Inner loop module and Outer loop module.

2.8.1 Initial module

The simulation is usually started with the vessel progressing into quiescent fluid, thus homogeneous boundary conditions are used as initial values. Specifically, the velocity potentials and their derivatives are taken to be zero on the free surface and far field boundaries. In addition, the free surface is also taken to be at the calm waterline level.

The initial body boundary conditions on the vessel are dependent on the initial motion prescribed to it, including the initial position and attitude, as well as the forward speed and yaw angle. These procedures are done by the Update subroutine.

2.8.2 Inner loop module

Two main loops are involved in the numerical procedure: an outer global time stepping loop and an inner sectional computational loop.

The inner loop independently solves for the complex potential and velocities of each computational plane. The computation for each plane starts by advancing the positions of the nodes and vortices. The free surface nodes and vortex blobs are convected using the underlying fluid velocities calculated from the previous time step. For the body nodes, their positions are updated from the global motion of the vessel, which is solved from the outer loop. Then, the boundary conditions are updated according to the new nodal position. This allows a new system of equations to be assembled and ready to be solved. Finally, by solving the Cauchy integral equation, the complex potential and the required fluid velocities are obtained.

A predictor-corrector method is used to update the nodal positions in the inner loop. The procedure followed in the corrector step is essentially the same as the predictor step. The major difference lies in the evaluation of the vorticity transport equation. In the corrector step, the vortex blobs are given a random walk to simulate

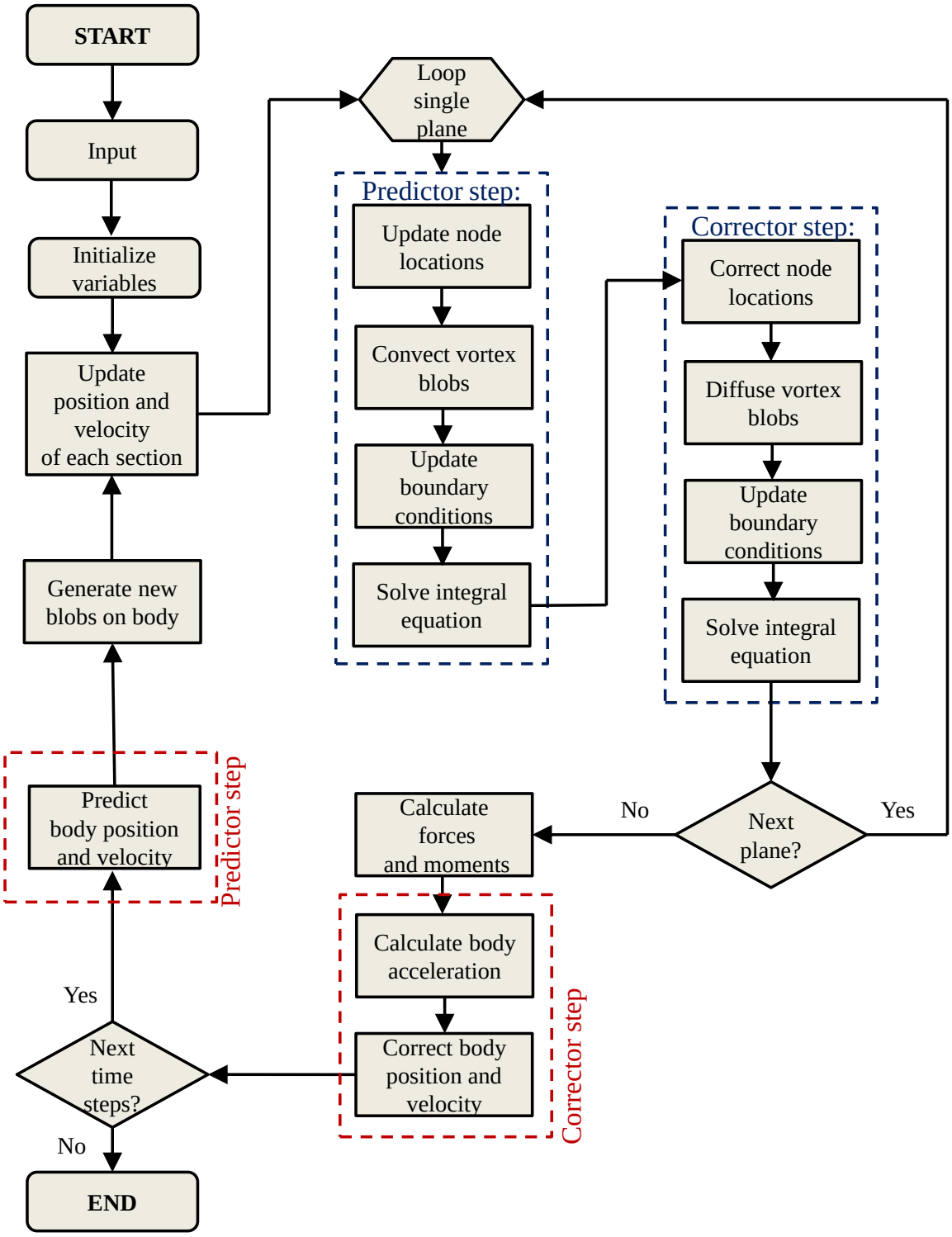

Figure 2.10: Flowchart of the program.

the diffusion of vorticity. More information is given in the next subsection.

2.8.3 Predictor-corrector method

Since FSRVM uses the mixed Eulerian-Lagrangian formulation on the free surface, the positions of the boundary nodes on the free surface have to be advanced in time. In addition, the Neumann condition on the free surface is used to advance the value of the homogeneous velocity potential there. To advance these values in time, FSRVM uses a predictor-corrector method. The update procedure of the positions of the vortex blobs in the convection step also follows the same method. Using a predictor-corrector, the position of a node or blob is first advanced, based on the velocities at the beginning of the predictor step. After that, the boundary conditions are updated according to the predicted nodal positions. This allows an "intermediate" system of equations to be assembled and solved. By solving the "intermediate" problem, updated velocities are obtained at the end of the predictor step. Then, the corrector step combines the initial and intermediate velocities to give more accurate estimates of the velocities. Based on the corrected velocities, the positions of nodes and blobs are advanced.

With respect to the specific numerical methods, FSRVM uses a first order Adams-Bashforth predictor for the time-independent cases and a simple Euler predictor for the time-dependent cases. A first order Adams-Moulton corrector step is used for both cases.

2.8.4 Outer loop module

The outer loop is responsible for calculating the global forces, solving the global accelerations and advancing the global motion in time. In this loop, the acceleration of the vessel with respect to the referenced translating frame is solved first, and then the velocity and position are obtained after time integration. At the end, the sectional body motion in each translating frame is evaluated to prepare for the inner loop in the next time step.

The predictor-corrector method is applied for the advancement of the body motion. At the beginning of each time step, the global velocity is predicted from the acceleration at the previous time step as shown in Eqn. 2.70. And the position of the body is similarly predicted from the velocity at the previous time step. Then based on these predicted values, the position and velocity of each station of the vessel is

updated in the corresponding sub-translating frame.

$$\vec{\bar{V}}_{i+1}^{p} = \vec{\bar{V}}_i + \dot{\vec{\bar{V}}}_i \Delta t \tag{2.70}$$

where the variables marked with a superscript , p, denote intermediate values.

After the inner loop and solving the equation of motion, Eqn. 2.71 is used to correct the velocity. Finally, the position vector of the body is also corrected by Eqn. 2.72. This is the last step for the current time step.

$$\vec{\bar{V}}_{i+1} = \vec{\bar{V}}_i + \frac{1}{2}(\dot{\vec{\bar{V}}}_i + \dot{\vec{\bar{V}}}_{i+1})\Delta t \tag{2.71}$$

$$\vec{\bar{X}}_{i+1} = \vec{\bar{X}}_i + \frac{1}{2}(\vec{\bar{V}}_i + \vec{\bar{V}}_{i+1})\Delta t \tag{2.72}$$

The next time step starts the prediction of the body position and velocity. After that, new boundary conditions are set up for the new round of inner loop and outer loop. The procedure will be repeated till the end of simulation is reached.

This page intentionally left blank.

Chapter 3

Effectiveness of SSFSRVM Modeling

Aloisio & Felice (2006) carried out an experimental study of the velocity field around a ship model in free roll decay motion at the INSEAN towing tank n°2. The ship model is a bare hull with a pair of bilge keels. Measurements are carried out at both Froude numbers $Fr = 0$ and $Fr = 0.138$. The flow around the bilge keels was investigated using a 2-D PIV underwater system. Their experiments visualize the fluid dynamics and provide a set of certified experimental data that can be used to validate numerical simulations.

To evaluate the accuracy of SSFSRVM in predicting the roll motion of a three-dimensional hull with bilge keels, these experimental results are compared with our numerical computations.

3.1 Free roll decay with zero forward speed

In this section, we will compare the time histories of roll motion resulting from SSFSRVM simulations and experimental measurements. Furthermore, we will examine the accuracy of the numerical model on simulating vortical structures in the fluid by comparing the numerical predictions with the experiments. Then, flow along the three-dimensional hull will be presented to illustrate the motion of the vortex filaments generated and convected by the bilge keels.

Table 3.1: Geometric and hydrostatic parameters of INSEAN model C2340.

Parameter	Units	Model C2340
Linear scale ratio	–	24.8
Length L	m	5.72
Beam B	m	0.768
Draft T	m	0.248
Displacement $\forall$	m^3	0.554
Block coefficient C_B	–	0.506
Roll radius of gyration $k_{44} = 0.25B$	m	0.192

3.1.1 Roll decay time history

In the experiments, a 5720 mm length model (INSEAN model C2340) with bilge keels was chosen and tested in the free roll decay motion without forward speed. The span of the bilge keel is 4.76% of the full beam of the hull. The model-scale geometric and hydrostatc parameters are summarized in Table. 3.1. All other motions of the ship are constrained except the roll motion. Measurements were performed for 10 cycles with an initial roll angle of 10°.

By using SSFSRVM, we simulated the same roll decay test. The time histories of roll motion from the experiments and SSFSRVM simulations are presented in Fig. 3.1. It can be seen that the numerically predicted time history matches exceedingly well with the experimental data, a remarkable confirmation of the theory.

3.1.2 Vorticity contours at the midship section

To further validate the accuracy of the model on simulating the viscous-fluid flow around the ship with zero Froude number, the vorticity evolution near the port-side bilge keel (at the longitudinal position, $\chi/L = 0.504$) was simulated and compared to experimental PIV measurements, as can be seen in Fig. 3.2 and 3.3. The blue color in the figure denotes negative (clockwise when observed from bow) vorticity, while the red color denotes positive (counter-clockwise) vorticity. In both PIV measurements and simulation, a positive vortex roll up gradually at the keel with increasing strength and core size during the first half period. When the roll motion changes its direction at $t = 1.02$ sec, a negative vortex gradually roll up. After a short period of time, a pair of two counter-rotating vortices is generated at the keel. Then, the interaction between

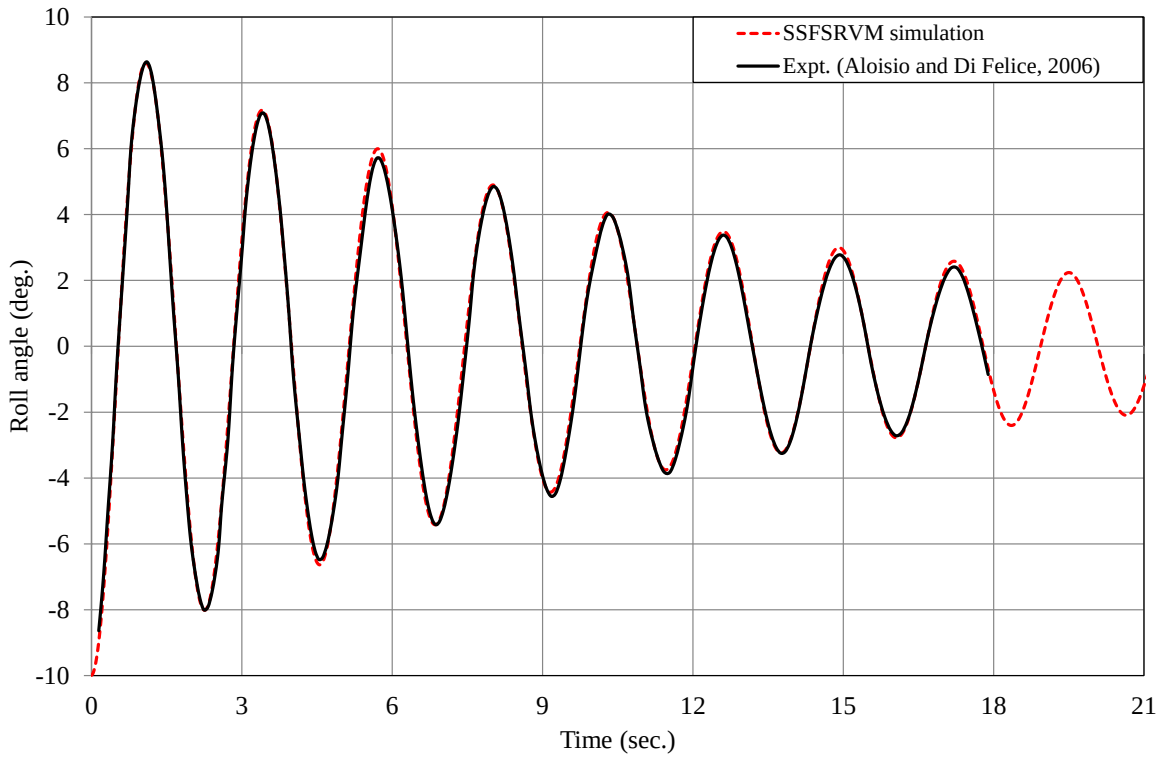

Figure 3.1: Time histories of the roll motion: experimental measurements and the SSFSRVM simulation for the case of $Fr = 0$.

the counter-rotating vortices drives the vortex pair away from the hull between $t = 1.53$ and $t = 1.78$ sec. Since the hull continues rolling counterclockwise, another negative vortex gradually grows up (see at $t = 2.03$ sec in Fig. 3.3). However, the newly generated negative vortex does not have a strong core because the roll motion changes its direction in a short period of time. At $t = 2.285$ sec, a positive vortex emerges at the keel. Then its strength and core size increase as the clockwise roll motion progresses in time. Subsequently, another pair of two counter-rotating vortices appears, and travels away due to the interaction between them. It is known that this interaction accelerates the energy diffusion in the fluid. The negative vortex expands, diffuses, and loses its strength soon afterwards. But the stronger positive vortex keeps its core, travels back to the hull, and forms another vortex pair with a newly generated negative vortex (see $t = 3.3$ to 3.8 sec).

Based on the comparison of these two figures, we conclude that the numerical model closely predicts the motion of vortices as well as the interaction between them. Although minor differences can be spotted, we believe the numerical model captures the motion of the vortical structures well.

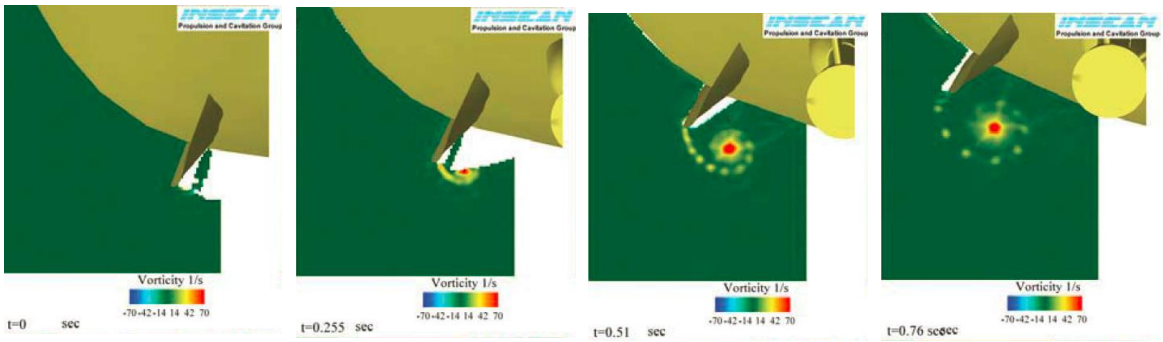

(a) Vorticity contours from experiments (t=0 to 0.76 sec).

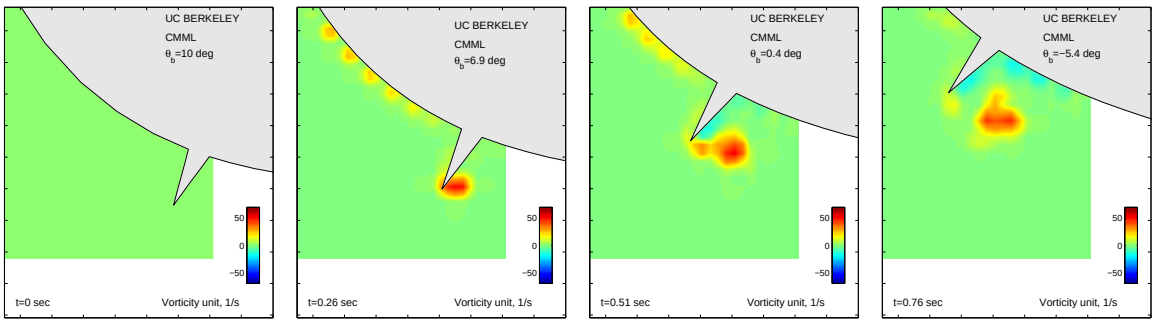

(b) Vorticity contours from SSFSRVM simulation (t=0 to 0.76 sec).

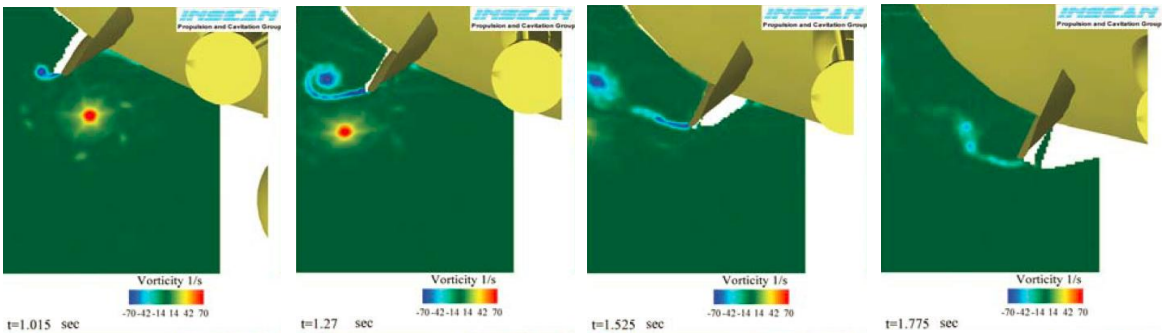

(c) Vorticity contours from experiments (t=1.015 to 1.775 sec).

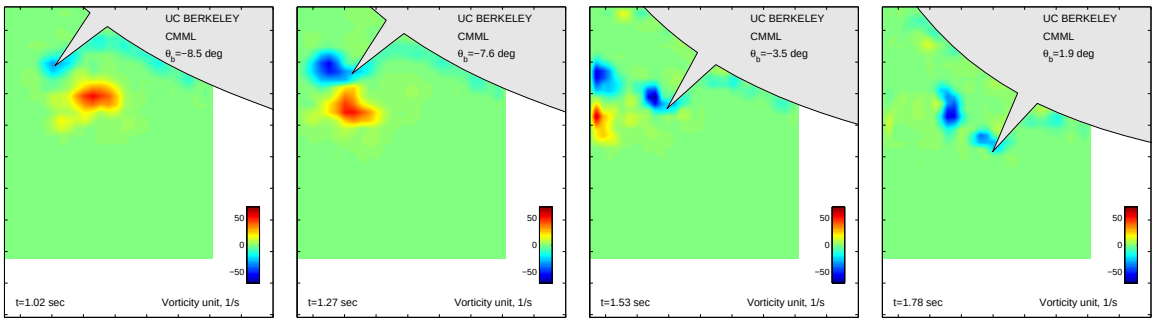

(d) Vorticity contour plots from SSFSRVM simulation (t=1.02 to 1.78 sec).

Figure 3.2: Comparison of vorticity evolutions at the section $\chi/L = 0.504$ between experiments and simulations for t=0 to 1.78 sec.

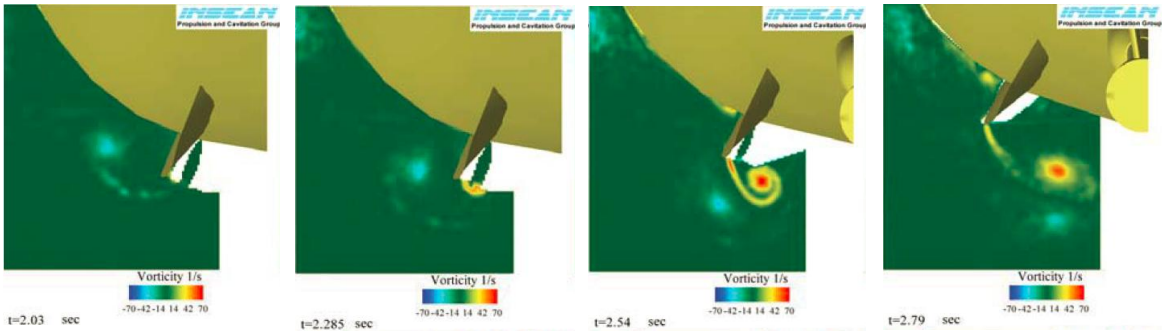

(a) Vorticity contours from experiments (t=2.03 to 2.79 sec).

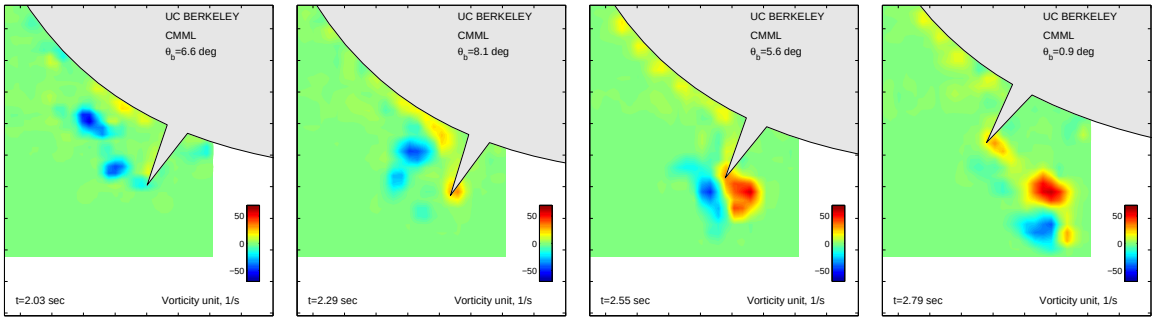

(b) Vorticity contours from SSFSRVM simulation (t=2.03 to 2.79 sec).

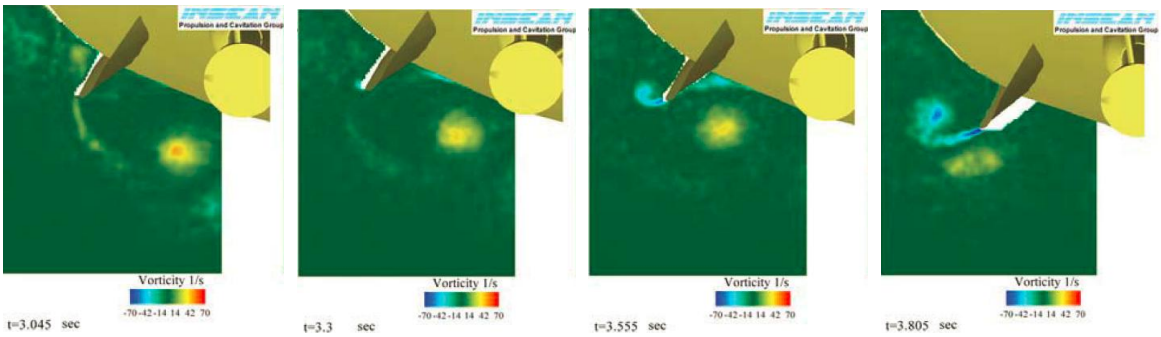

(c) Vorticity contours from experiments (t=3.045 to 3.805 sec).

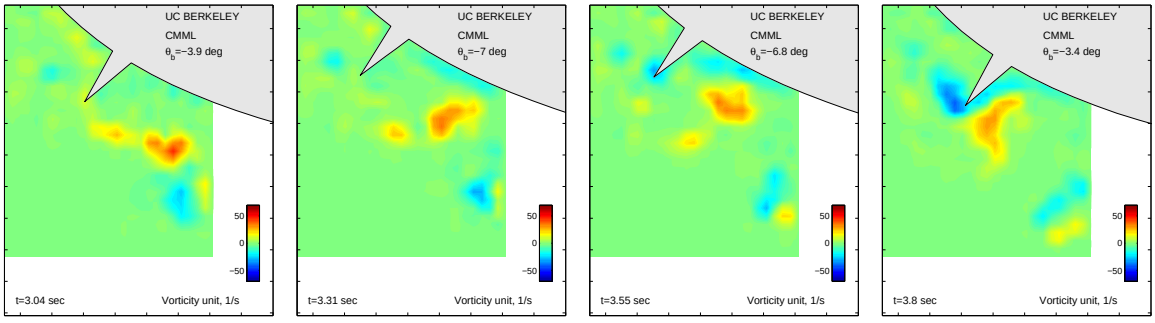

(d) Vorticity contour plots from SSFSRVM simulation (t=3.04 to 3.8 sec).

Figure 3.3: Comparison of vorticity evolutions at the section $\chi/L = 0.504$ between experiments and simulations for t=2.03 to 3.8 sec.

3.1.3 Flow along the three-dimensional hull

In the previous subsection, we showed the vorticity evolution near the port-side bilge keel in the midship portion. The evolution illustrates the motion of vortices and validates the numerical model in a two-dimensional manner. To visualize the predicted three-dimensional nature of the vortical structures, Figs. 3.4 - 3.6 present a quarter-period time sequence of vorticity contours and vorticity iso-surfaces along the three-dimensional hull in the first cycle of roll decay motion. Times are selected to correspond with the peaks and zero crossing of the roll motion as shown in the upper left sub-figures of Figs. 3.4 - 3.6. In the figures, the blue color still denotes negative vorticity (clockwise observed from bow), while the red color denotes positive (counter-clockwise) vorticity. In the lower right corner, a two-dimensional vorticity contour at the midship section is given as a diagram of the three-dimensional sub-figure. The iso-surfaces are plotted in the three-dimensional sub-figure to represent the vortex filaments in the fluid. In the following analysis we will focus on the starboard bilge keel for convenience.

Figure 3.4 shows the vorticity distribution at the moment when the hull starts to change its roll direction. It can be seen that a positive strong vortex filament has rolled up with strong vortex cores along the starboard bilge keel. Besides, a negative vortex filament is just generated at the tip of the keel with a very small core. As the roll motion progresses in time, the newly generated negative vortex filament rolls up. When the ship rolls to its vertical position (see Fig. 3.5), a fully formed vortex-filament pair is evident. Then the interaction between the counter-rotating vortices convects the pair away from the hull and rapidly mixes their energy and decreases their cores. When the ship reverses its direction (see Fig. 3.6), a new negative vortex filament is generated near the tip. At this moment, the previously generated vortex pair has split into parts and almost dissipated into the surrounding fluid, as shown in Fig. 3.6. As the roll motion progresses in time, a positive vortex filament will be generated at the keel. Then, a new cycle of vortex shedding will start.

These three figures illustrate the motion of vortex filaments in the first oscillation. We find that bilge keels alternately generate positive and negative vortex filaments and form vortex pairs along the hull. The vortical structures that represent high energy density dissipate the kinetic energy of the hull, increase the viscous damping and reduce the amplitude of roll motion. These figures clearly reveal the working mechanism of the bilge keel from the energy-dissipation point of view. Through the above analysis, we consider that the SSFSRVM model is capable of simulating the

three-dimensional vortical structures.

In terms of the computation time, it costs 6 hours on a standard desktop computer with a four-core CPU to simulate these 10 cycles of roll motion. Considering the accuracy, the useful information, and the computation time, we conclude that SSFSRVM as described is an excellent modeling tool for predicting the roll motion of ships with bilge keels and for investigating the effects of bilge keels.

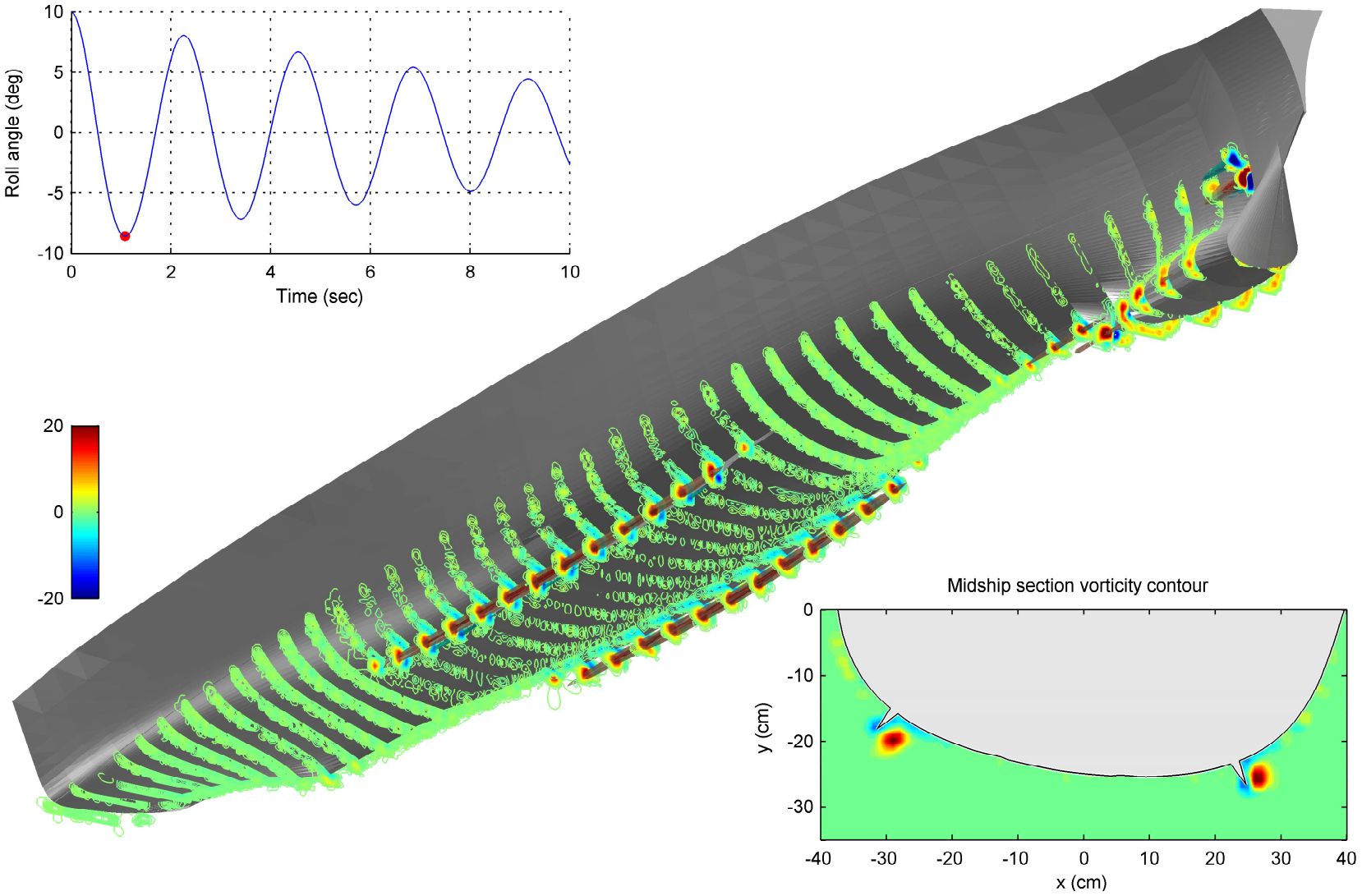

Figure 3.4: Vorticity contours and vorticity iso-surfaces along the hull at t =0.90 sec.

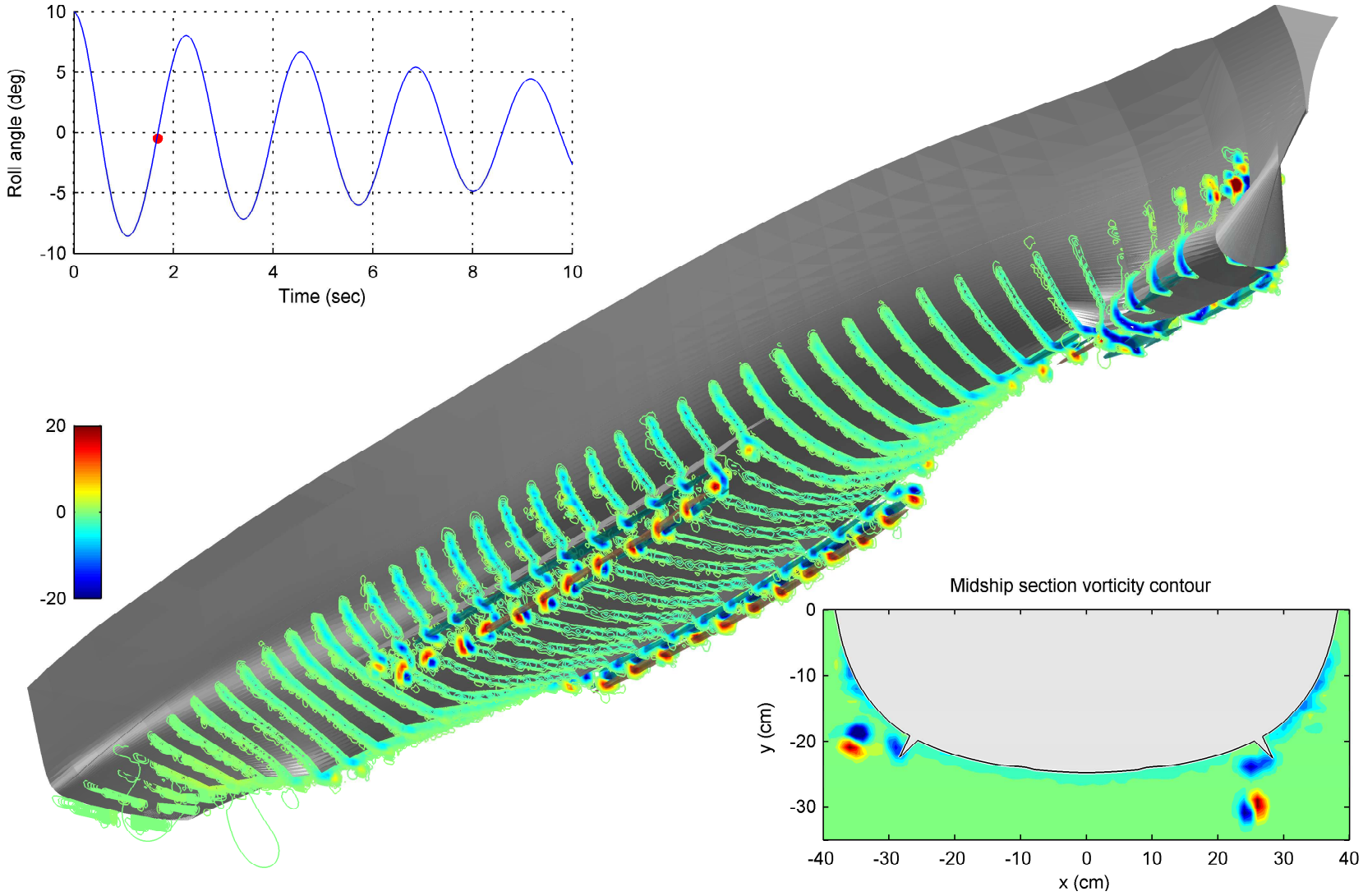

Figure 3.5: Vorticity contours and vorticity iso-surfaces along the hull at t =1.69 sec.

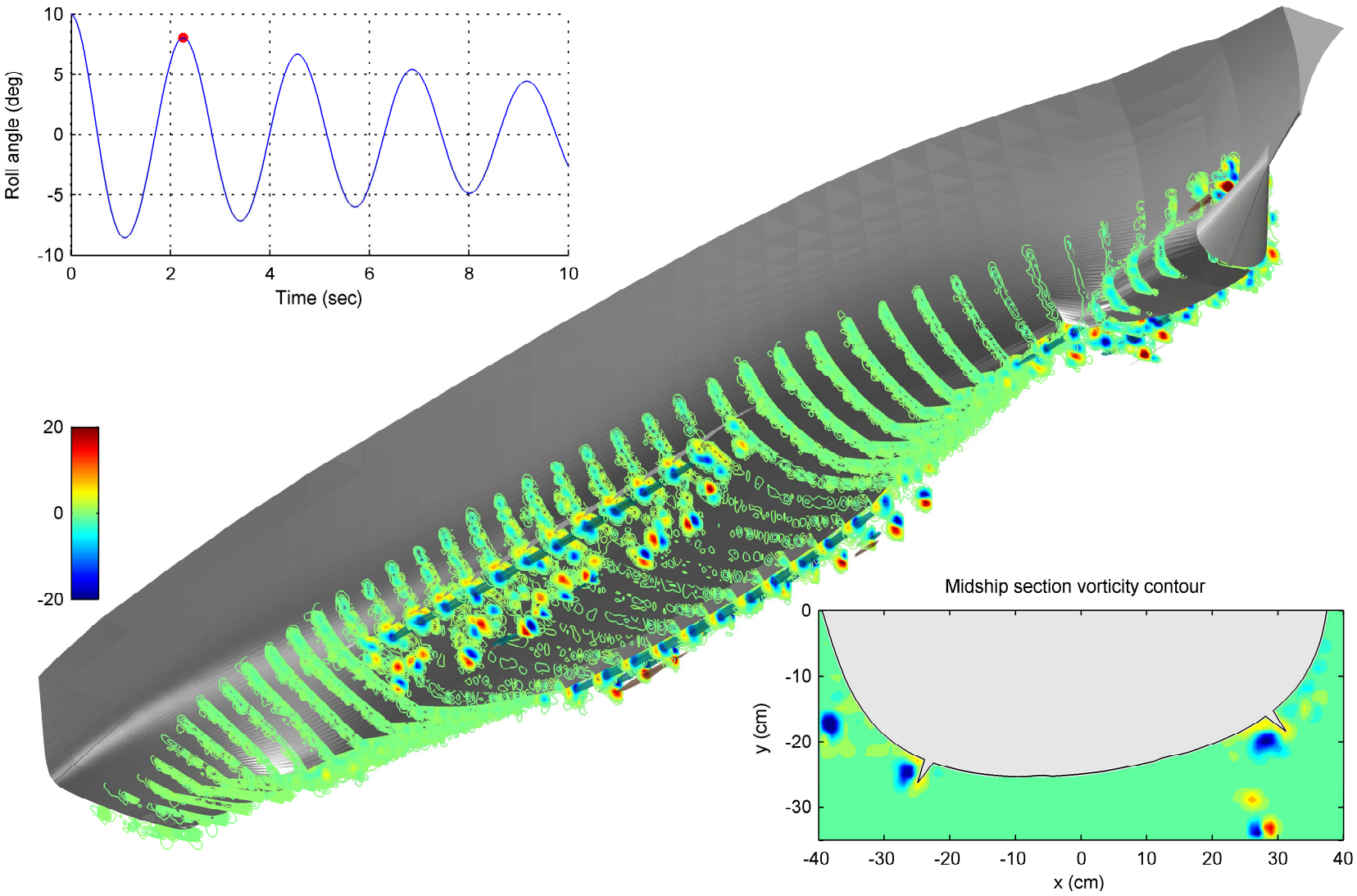

Figure 3.6: Vorticity contours and vorticity iso-surfaces along the hull at t =2.26 sec.

3.2 Free roll decay with forward speed

In this section, we examine the accuracy of SSFSRVM model in simulating the roll motion of a moving vessel with a constant forward speed. The concept of expansion velocity is employed to simulate the hull speed in this scenario. In addition to the free decay test without forward speed, Aloisio & Felice (2006) also carried out a decay test at the INSEAN towing tank n°2 with a forward speed of 1.03 m/s. Based on the model scale, the corresponding Froude number Fr is 0.138. In the experiment, the model C2340 was initially towed with the target forward speed in static heel to port in calm water. When the surface waves were in a steady state, the ship model was released from an initial angle of 10° by using an electromagnet.

3.2.1 Roll decay time history

By using SSFSRVM, we simulated the roll decay test for the same scenario. The numerical ship model pierces in calm water with a constant hull speed of 1.03 m/s and with a constant roll angle of $R_0 = 10°$ for about 5 seconds when the pattern of the surface waves does not change. At this moment, the ship is released from 10° and starts to roll freely. The comparison of the time histories of roll motion for this scenario resulting from the experiments and SSFSRVM simulations is presented in Fig. 3.7. Again, the predicted time history closely matches the experimental data, especially for the first three periods. Good agreement between the present theoretical calculation and the experimental measurement can be found. Based on the above comparisons of roll time histories, we validate the slender-ship free-surface random-vortex method in simulating the roll motion of a vessel with and without forward speed.

3.3 Surface waves due to the body motion

Figure 3.8 shows a time series of the surface waves disturbed by the body motion of the model C2340 resulting from the numerical simulation. In the figures, all the lengths are normalized by the body length. The color on the surface denotes the wave elevation. The peaks and troughs are represented by the cyan and blue colors respectively. The time parameter t shown in the figures is measured starting from

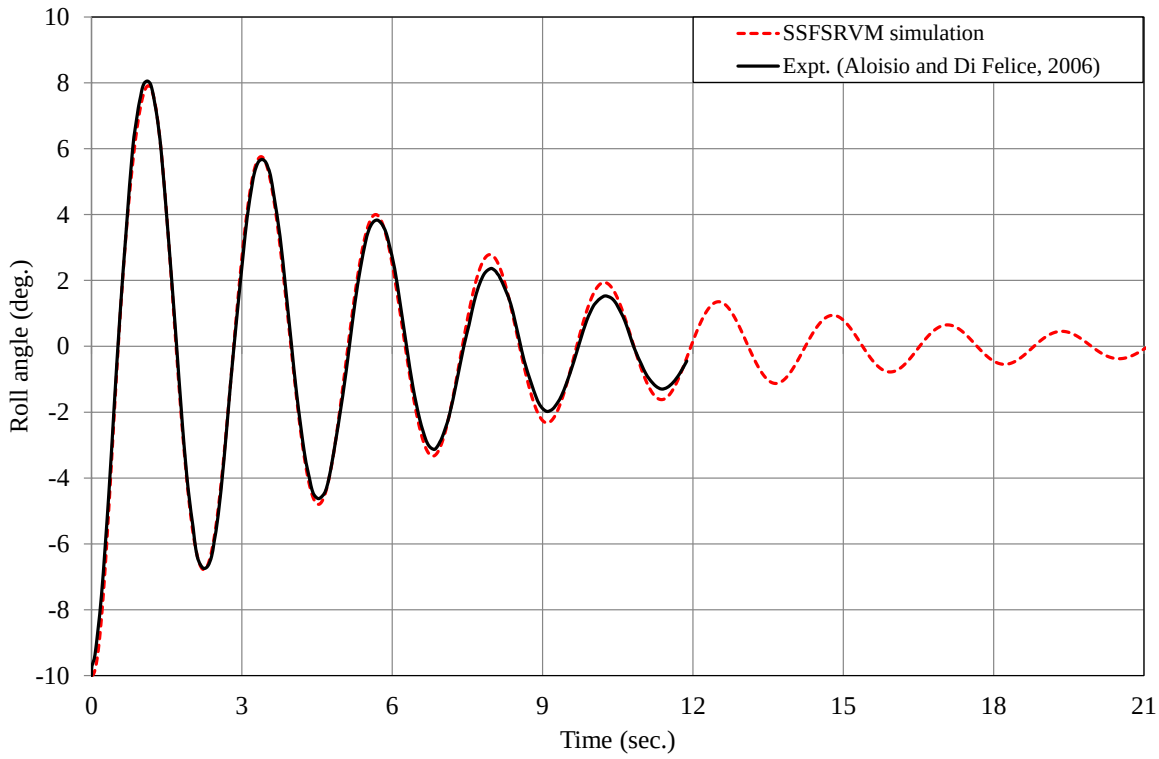

Figure 3.7: Time history of the roll motion: comparison between the experimental measurement and the SSFSRVM simulation for $Fr = 0.138$.

the release point. Before the hull was released to roll, it moved forward in static heel to port for about five seconds with a constant speed. Consequently, both sides of the divergent wave fields are fully developed and in a steady state, as shown in the first sub-figure. In addition, we find that the starboard wave field has smaller amplitudes at $t = 0$ sec, since the hull was constantly heeling to the port side.

After the ship is released, the model rolls through its vertical position to the starboard side at $t = 0.55$ sec and reaches the maximum negative roll $\theta_b = -7.9$ deg at $t = 1.11$ sec. At this time instant, it can be seen that the rolling motion of the ship induces waves on both sides of the hull. We call these waves as the roll-induced waves. The peak of the roll-induced waves is generated on the port-side surface. The bow, shoulder, and stern waves have larger amplitudes, especially close to the hull. On the starboard-side surface, the trough of the roll-induced wave is found. After that, the ship model begins another half-cycle rolling back to the port side. When the model reaches the maximum positive roll $\theta_b = 6.7$ deg at $t = 2.21$ sec, the peak of the roll-induced wave on the port side has already propagated by about a half body length. A trough is generated near the port side of the hull. On the starboard side,

the initially formed trough also propagates away from the hull, and a peak forms near the hull. For subsequent roll cycles, the motion of the wave field previously described repeats with each successive roll cycle. Peaks and troughs of the roll-induced waves are generated alternately on both sides of the hull and travel away from the hull. All of the divergent wave amplitudes are in varying stages of increasing or decreasing depending on the roll-induced waves. The initial divergence wave field has been disturbed entirely. With the motion amplitude decaying, the newly generated roll-induced waves are not as significant. The divergent wave pattern starts to recover (see the last sub-figure of Fig. 3.9).

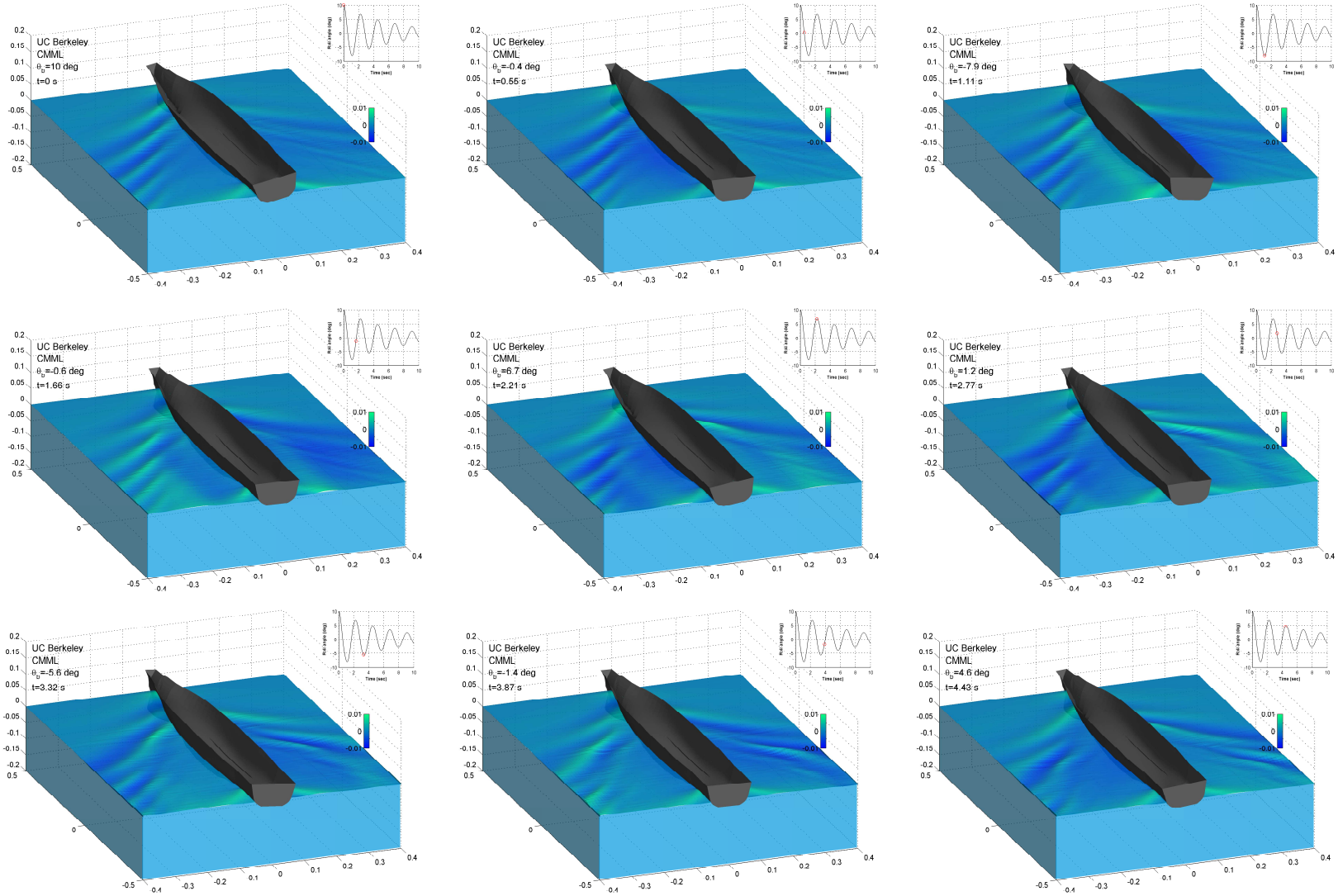

Figure 3.8: Time series of surface waves from $t = 0$ sec to 4.43 sec for $Fr = 0.138$.

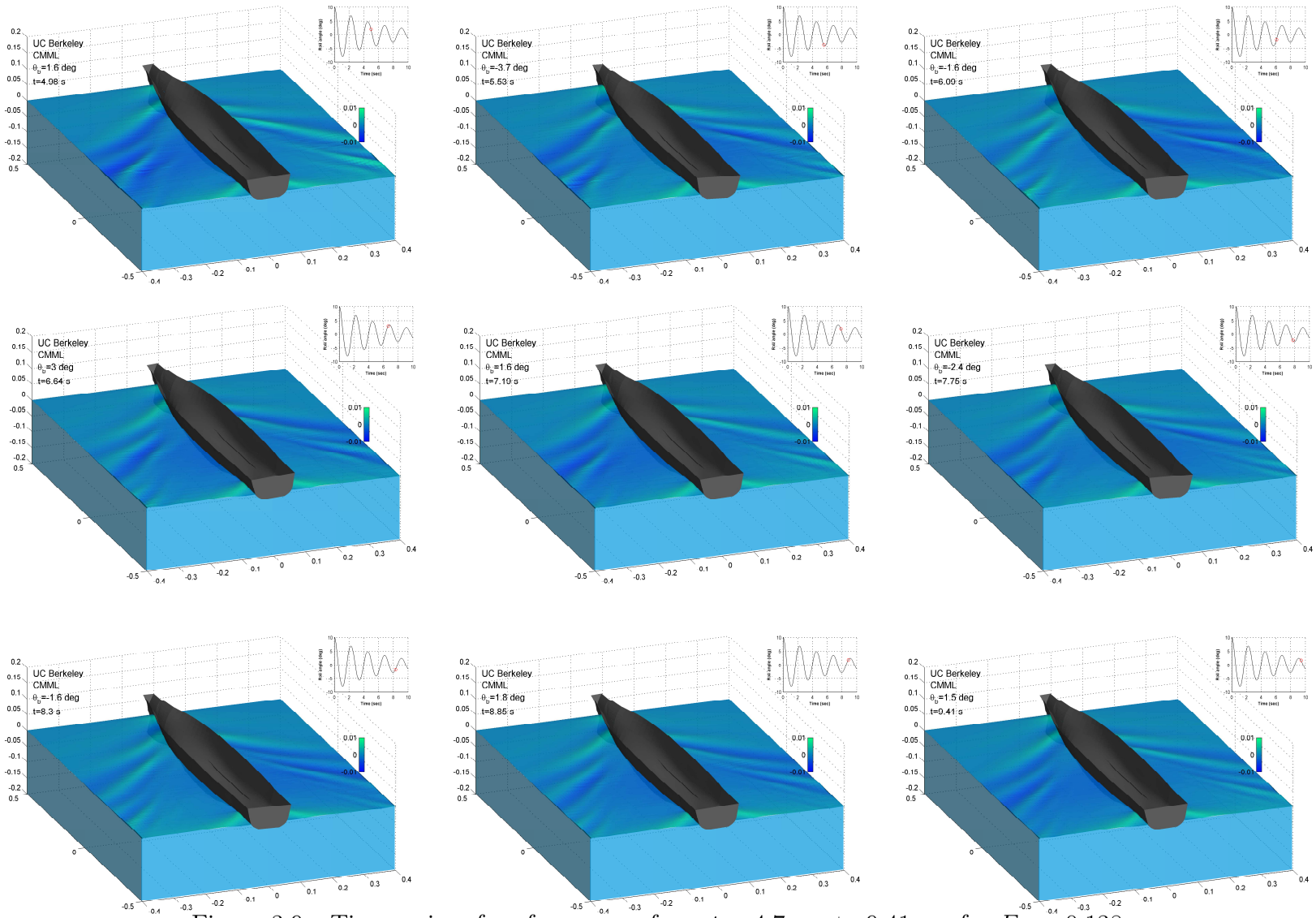

Figure 3.9: Time series of surface waves from $t = 4.7$ sec to 9.41 sec for $Fr = 0.138$.

3.4 4-DOF free decay motion

Figure 3.10 presents the free decay test of the ship model in 4 DOFs with a larger initial roll angle of 15° and zero hull speed. It can be seen that the nonlinear coupling of motion modes transfers energy among the different motions. The heave motion ramps up and oscillates roughly at the natural heave frequency. The coupling effect between the sway and roll motions leads to a slow drift of the sway response. Figure 3.10 shows the capability of SSFSRVM to simulate multi-DOF motion.

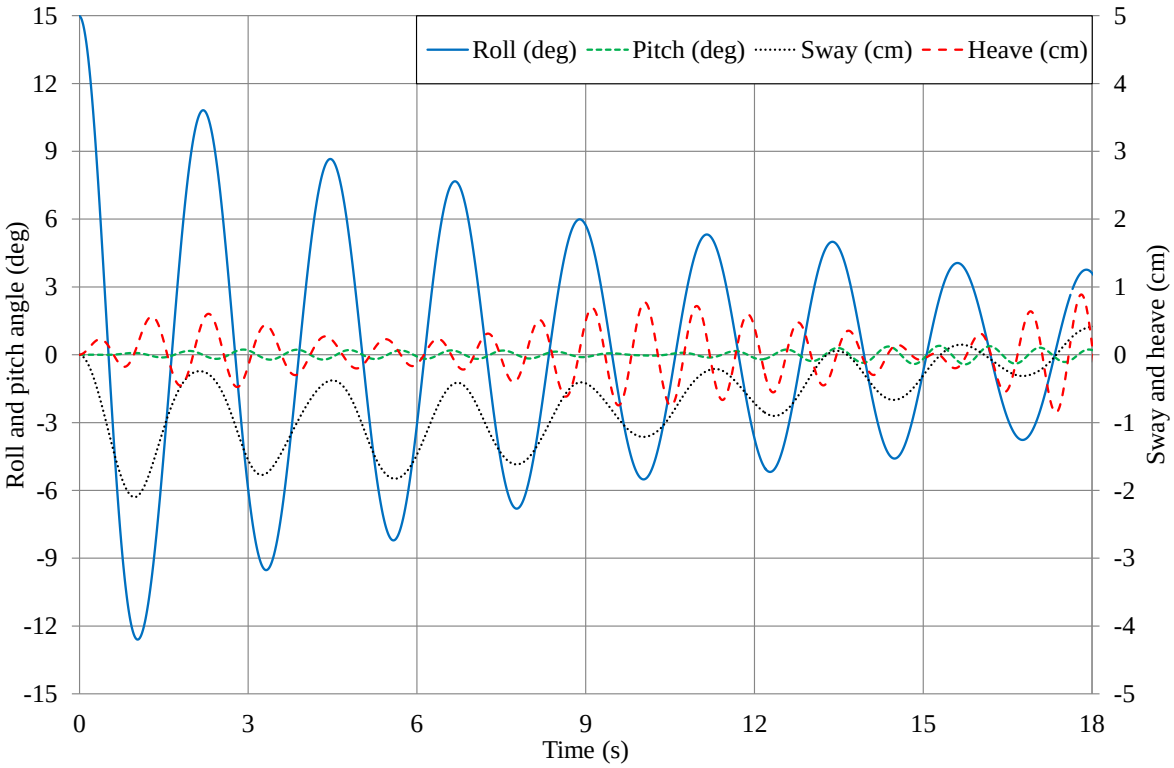

Figure 3.10: Time history of a free decay motion in four DOF with an initial roll angle of 15°, simulated by SSFSRVM.

Chapter 4

Effects of Bilge-Keel Span

As mentioned previously, the roll damping of a ship is caused by various factors, such as free-surface waves, skin friction of the hull, eddy sheeding from the hull, etc. The presence of bilge keels can also strongly affect the roll damping. The concept of component damping has been pointed out and studied for a couple of decades. The total roll damping is assumed to be a summation of five components: friction, eddy, wave, lift-effect, and bilge-keel damping. In this framework, the pair of bilge keels is considered to be an add-on to a bare hull. The bilge keel damping was proposed and defined as the increment of pressure damping due to the presence of bilge keels. Alongside the damping coming from the bilge keels themselves, the interaction effects among the bilge keels, hull, and surface waves results in extra damping. Thus, the bilge-keel damping is usually assumed to be the summation of the normal-force damping of bilge keels, the hull-pressure damping due to bilge keels, and the wave damping due to bilge keels. In this chapter, we will report the bilge keel effects based on these three components by using SSFSRVM. In addition, the roll decay coefficient, vorticity contours at the midship section, and ship response in waves will be also presented in the following sections.

4.1 Time histories of roll motion

To evaluate the effects of the bilge-keel span on roll motion and damping, four ship models with different bilge-keel spans were built numerically as shown in Fig. 4.1. These four models have the same hull design (INSEAN model C2340) but different bilge-keel sizes. The span of BK1 is 4.76% of the full beam of the hull, which is the same as that of the C2340 model. The spans of BK2 and BK3 are two and three times larger than the span of BK1 respectively, while the model BK0 has no bilge keel. Figure 4.2 provides more details by showing midship sections of these four models.

The free roll decay tests using SSFSRVM were conducted on a range of keel geometries with an initial roll angle of 10° and with zero forward speed. The time histories of roll motion are shown in Fig. 4.3. From these figures, it can be seen that the bare hull (BK0) decays the slowest, while the hull with the largest bilge keels (BK3) decays the fastest. In addition, the bare hull has the smallest roll period, while the BK3 model has the largest one. These results indicate that a larger bilge keel provides more damping to decrease the roll amplitude, and also provides larger hydrodynamic added moment of inertia to increase the roll period. This behavior has been documented in the literature (Himeno, 1981) and has been recreated by SSFSRVM model.

4.2 Roll decay coefficient

To evaluate the effects of the bilge keel span on roll damping quantitatively, we compared the non-dimensional roll decay coefficient, n, among the different bilge-keel spans. This decay coefficient is determined by the logarithmic-decrement approximation:

$$\mathrm{n} = \frac{1}{2\pi} \ln \frac{\eta_i}{\eta_{i+1}} \tag{4.1}$$

where η_i and η_{i+1} correspond to consecutive double roll amplitude (see Fig. 4.4). Each value of n has a corresponding mean roll angle $\overline{\eta}$ associated with it, where

$$\overline{\eta} = \frac{1}{2}[(\eta_i + \eta_{i+1})/2]. \tag{4.2}$$

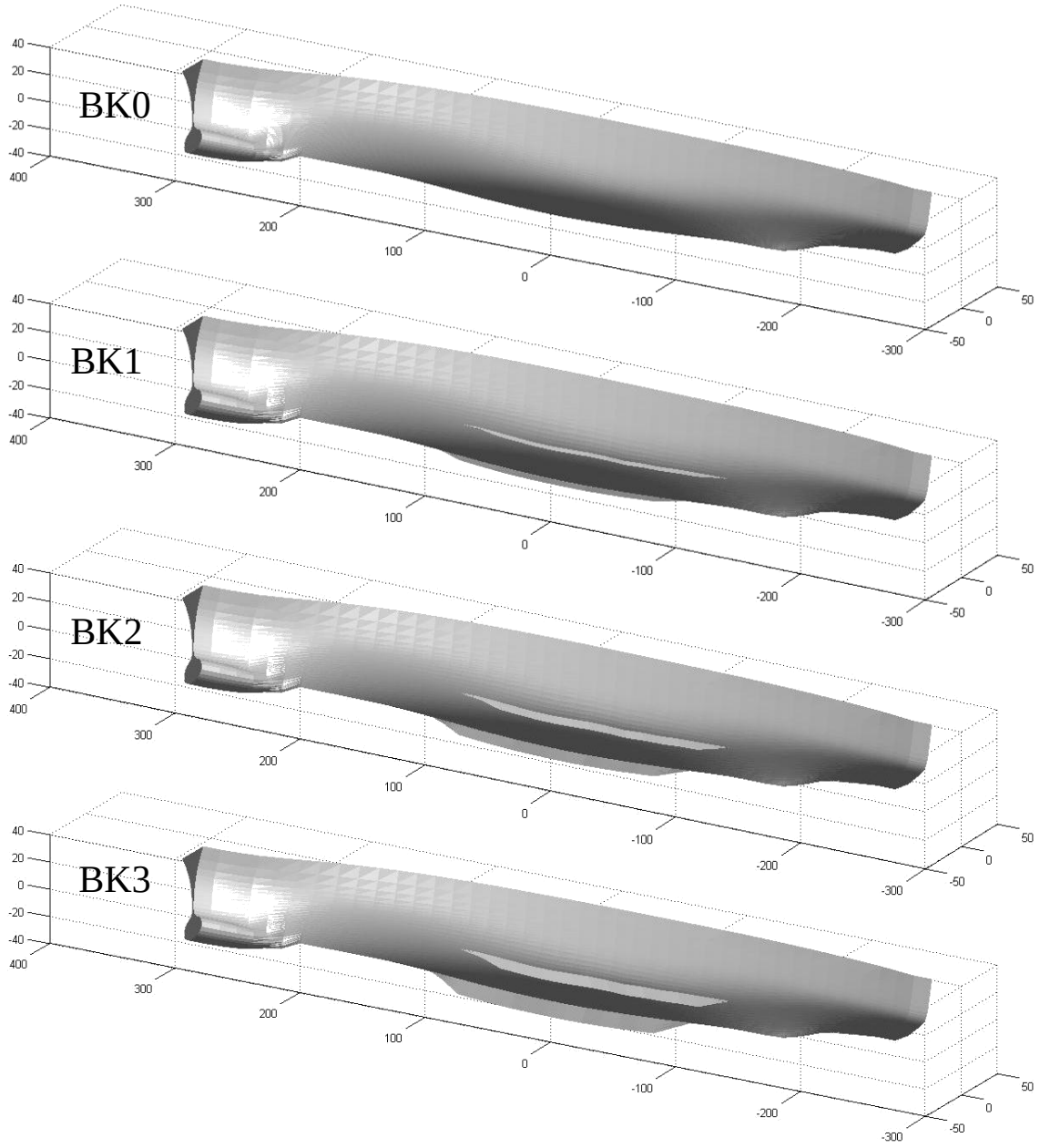

Figure 4.1: Illustration of C2340 ship model with different bilge-keel spans.

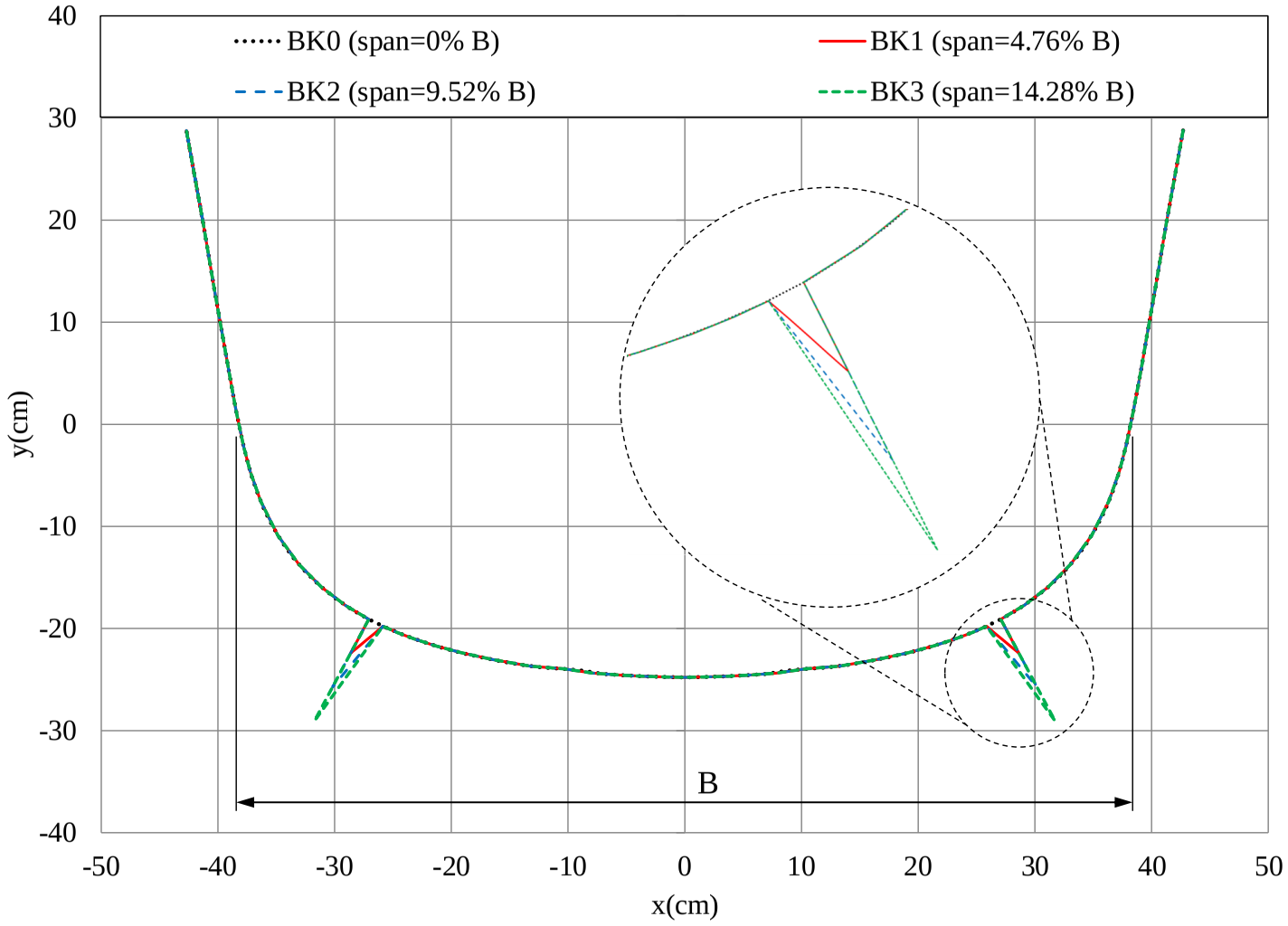

Figure 4.2: Illustration of the configurations of bilge keels at the midship section, where B denotes the full beam of the hull.

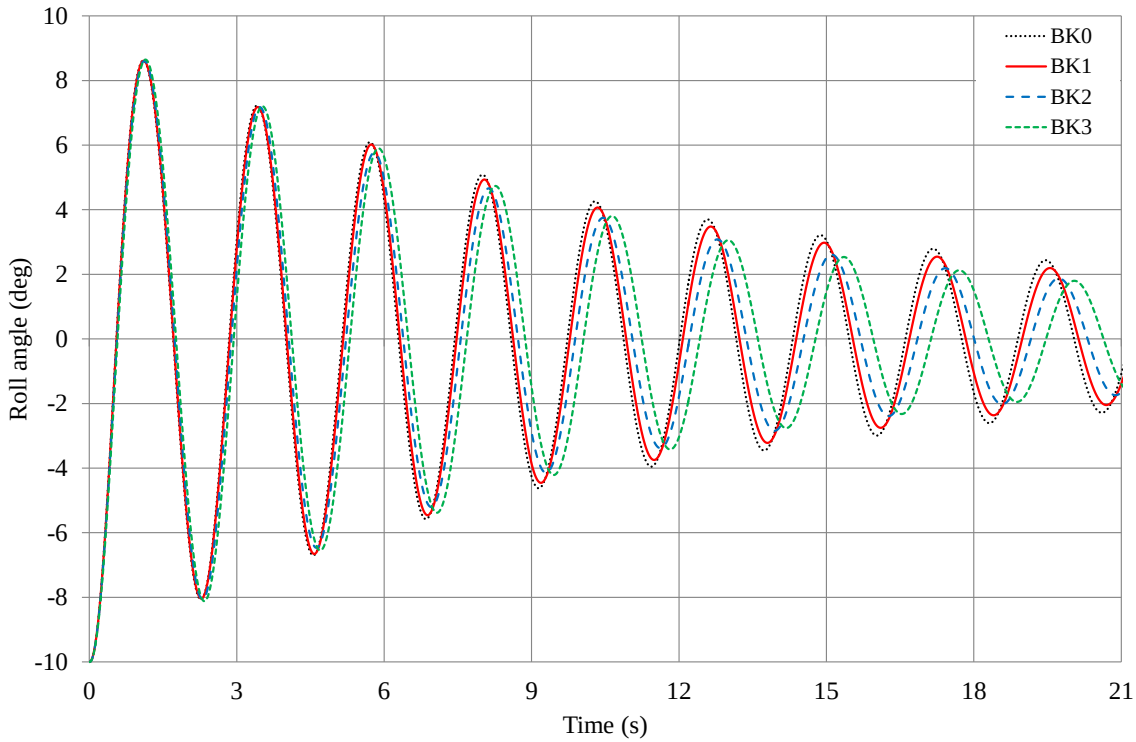

Figure 4.3: Comparison of the time histories of the roll decay motion between hulls with different bilge-keel spans.

The decay coefficient n can be plotted versus the mean roll angle $\overline{\eta}$ to evaluate the roll damping. Faltinsen (1990) showed that the slope and the y-axis intercept of the linear regression of the decay coefficient data are proportional to the linear and quadratic damping of the dynamic system, respectively. Figure 4.5 presents the non-dimensional decay coefficient versus the mean roll angle derived from the roll decay data of Fig. 4.3. The nonlinear characteristics of the roll damping are clearly reflected, based on the shapes of the curves. The decay coefficient highly depends on the mean roll angle. By using the data points whose mean roll angle is under 6°, the linear trendlines of the decay coefficient are shown in the figure for all four models. It is found that the trendlines fit the data points fairly well. This indicates that the quadratic component of the total damping plays an important role when the mean roll angle is smaller than 5°. We deduce that the BK3 model has the largest quadratic damping coefficient, since its trendline has the largest slope. In addition, a monotonic increase of the decay coefficient with the bilge keel span can be seen in the figure. However, the increase of the decay coefficient from the BK1 to the BK2 model is larger than that between BK2 to BK3. Thus, the roll damping does not linearly increase with the size of the bilge keel.

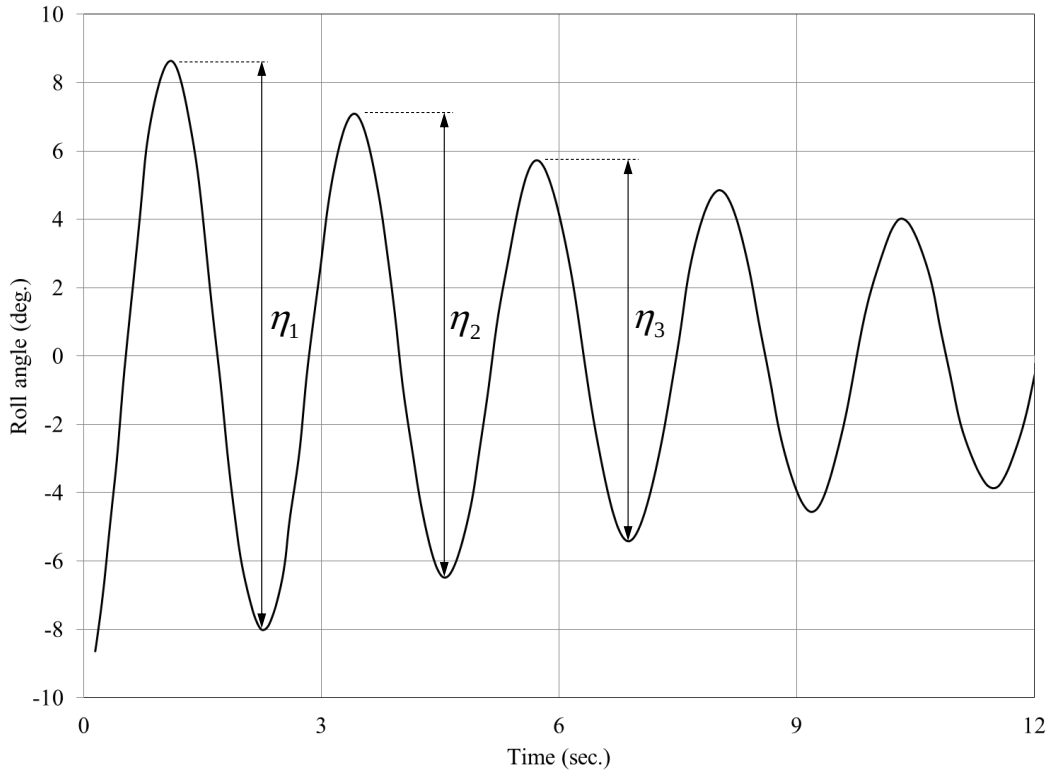

Figure 4.4: Illustration of the definition of consecutive double amplitude.

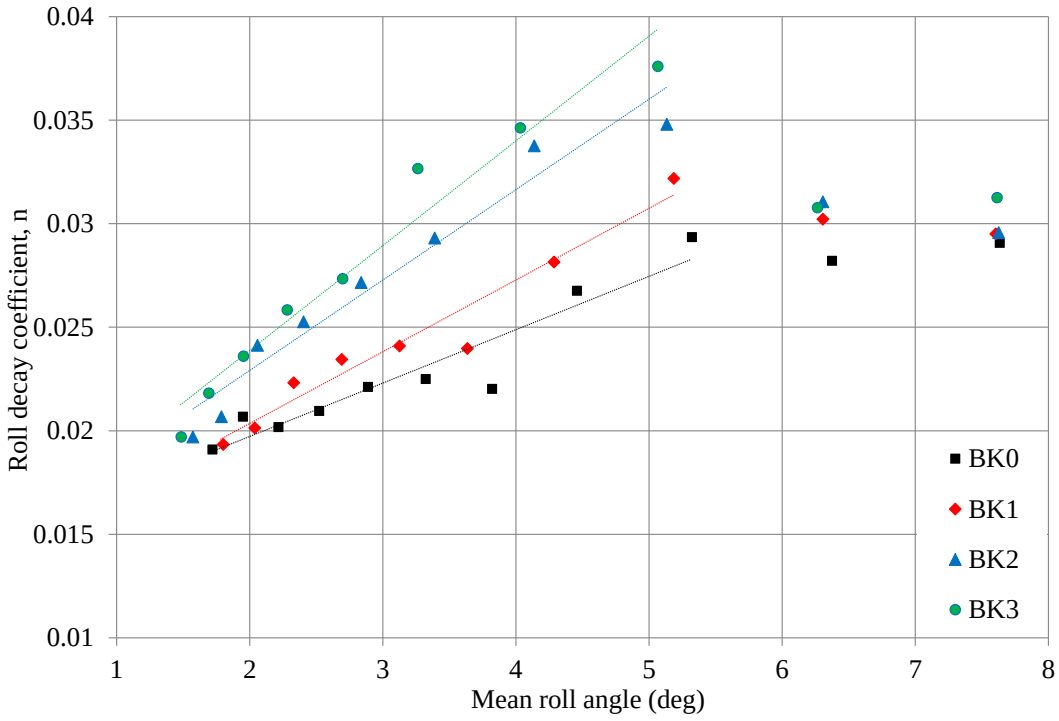

Figure 4.5: Comparison of the roll decay coefficients versus mean roll angles between hulls with different bilge-keel spans.

4.3 Vorticity contours at the midship section

To examine the differences in the roll decay coefficients of these four models from a fluid-mechanics and energy-dissipation point of view, the vorticity contours at the midship section at different time steps during numerical simulations are presented in Figs. 4.6 and Fig. 4.7. The first figure shows the fluid information in the first oscillation, and the second one shows the seventh. In these figures, each column represents one bilge keel configuration (BK0 is at the first column, and BK3 is the last). By comparing the plots of each row, we can investigate the effects of bilge keels in terms of vorticity field.

In Fig. 4.6, we note that for the model without bilge keels, the vorticity stays close to the body. That is, there is almost no flow separation, and the surrounding fluid particles do not have much voritcal motion. However, for all other models, it is found that strong vortical structures are generated by the bilge keels. Two vortices roll up gradually at two keels with increasing strength and core sizes during the first second. Two counter-rotating vortex pairs emerge when the hull changes its roll direction (see Fig. 4.6c). After that, the vortex pairs move away from the hull because of the interaction between themselves.

By comparing the vorticity contours among the BK1, BK2, and BK3 models, we find that the behavior of the vortical structures is very similar in the first oscillation, though their strength and core sizes are slightly different. The roll time histories of these four models are very similar during the first period as shown in Fig. 4.3. We deduce that the vorticity field did not build up sufficiently to provide a significant contribution to the decay, so the size of the bilge keels does not noticeably affect the response of the hull. In the second period when the vorticity field further develops, the vortical structures in the fluid start to provide a noticeable contribution to the roll damping; the roll time histories of the bare hull and the bilge-keel hulls start to differ. This feature can be seen in Fig. 4.5 where the roll decay coefficient of the BK0 model is smaller than that of other three models at $\overline{\eta} \approx 6^{\circ}$.

Figure 4.7 shows the evolution of the vorticity distributions in the seventh oscillation, where the roll amplitude is about 3°. From this figure, we find that the smallest bilge keel (BK1) cannot generate strong vortices due to the small roll amplitude, relative to BK2 and BK3. It is known that vortical structures characterize high energy dissipation. This phenomenon explains why the BK1 model has a smaller roll decay coefficient in Fig. 4.5 when the mean roll angle is around 3 degrees. By comparing

the voriticity contours of BK2 and BK3, we find that the vortices generated by the two models do not have significant differences with respect to their strengths and core sizes. However, the vorticity field of the BK3 model appears to be more complex and dynamic. This indicates that slightly more energy is dissipated into the fluid by the larger bilge keel, and explains the fact that the BK3 model has a slightly larger decay coefficient than the BK2 model in Fig. 4.5. Based on the plots of the roll decay coefficient and vorticity contours, we find that bilge keels generate vortices and these vortical structures increase the roll damping acting on the hull. Small bilge keels will not provide decent damping when the roll angle is small (under 3°).

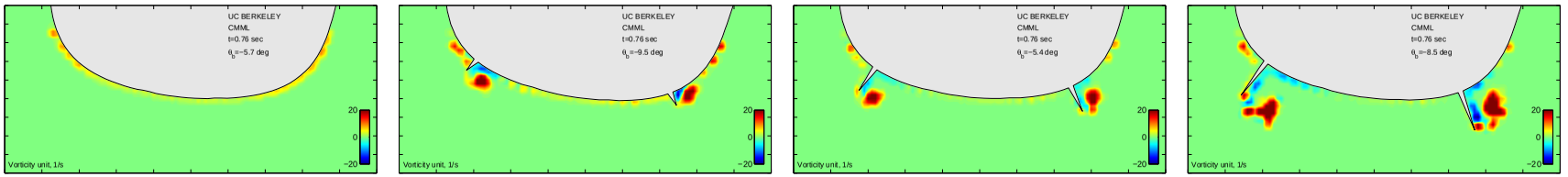

(a) t=0.76 sec.

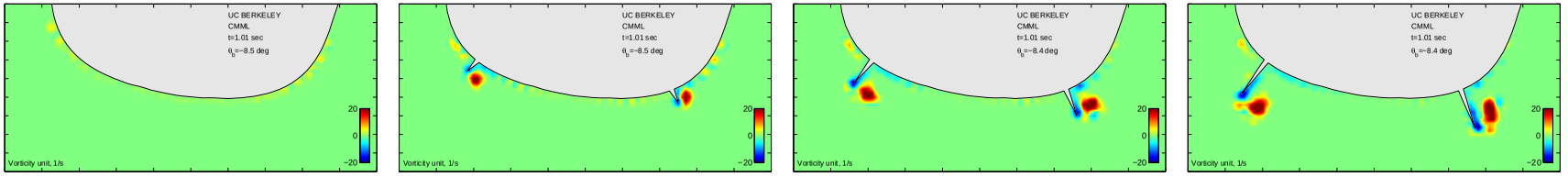

(b) t=1.01 sec.

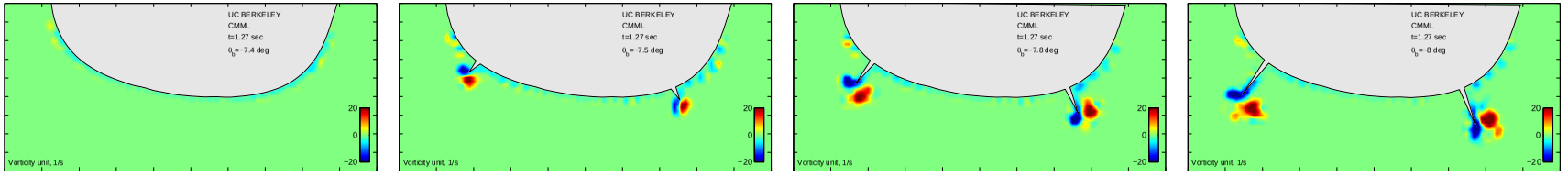

(c) t=1.27 sec.

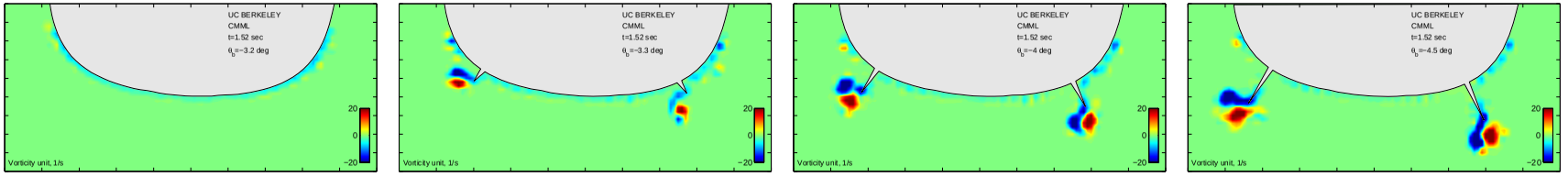

(d) t=1.52 sec.

Figure 4.6: Comparison of vorticity distributions at the midship section between hulls with different bilge-keel spans in the first oscillation. Each column represents one bilge-keel span.

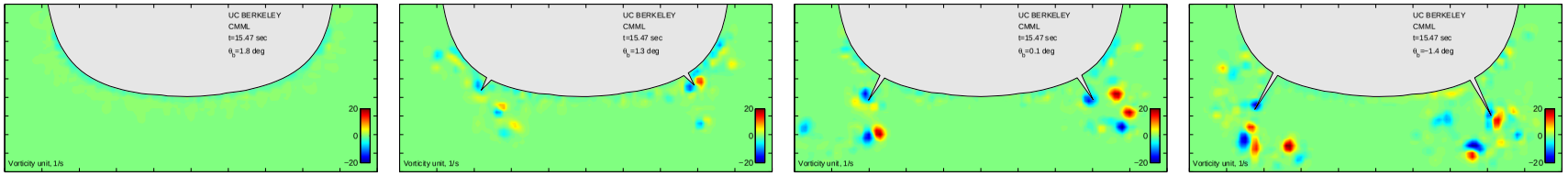

(a) t=15.47 sec.

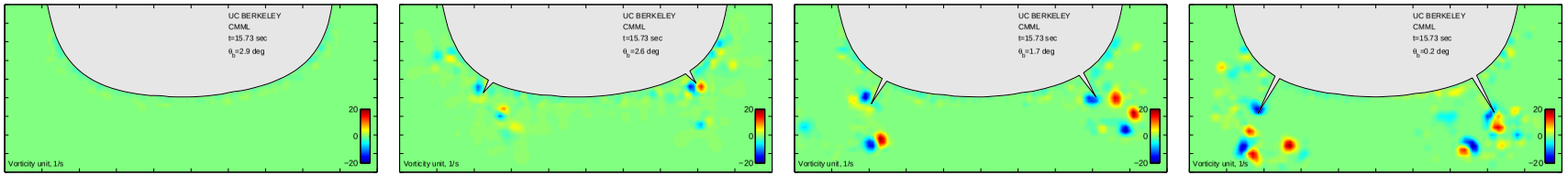

(b) t=15.73 sec.

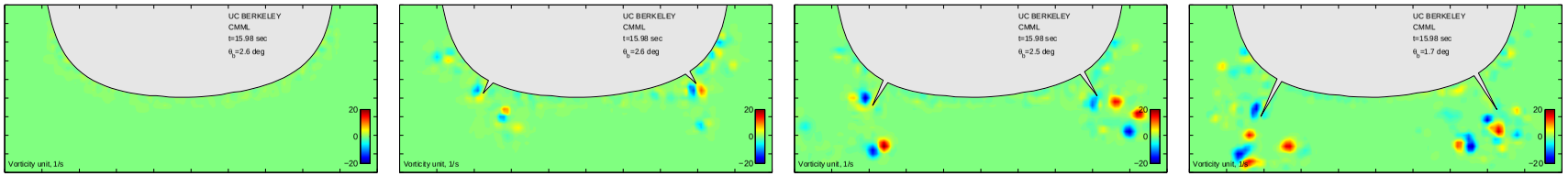

(c) t=15.98 sec.

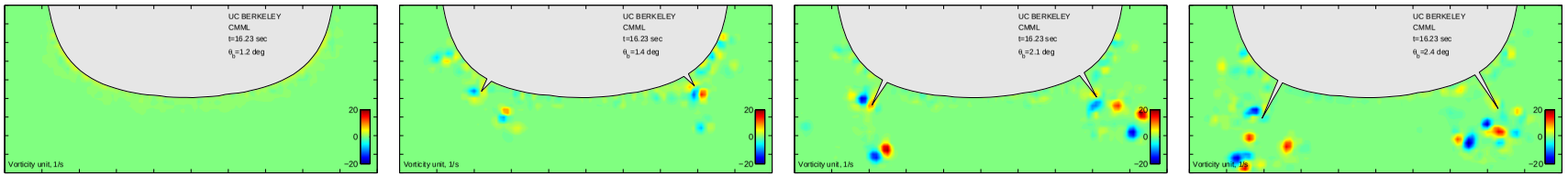

(d) t=16.23 sec.

Figure 4.7: Comparison at vorticity distributions of the midship section between hulls with different bilge-keel spans in the seventh oscillation. Each column represents one bilge-keel span.

4.4 Hull pressure distribution

From the previous results, we have found that the bilge keels generate vortices and cause flow separation. These features result in a pressure difference between the upper and lower sides of a bilge keel, as well as those on the hull surface. Here, we will discuss the hull-pressure damping due to bilge keels and the generation of the bilge-keel normal force.

Figure 4.8 shows the hydrodynamic pressure contours on the hull surface in the seventh oscillation for these four models. In this figure, the pressure contours are captured at the moment when the ship model experiences a roll angle of -5 deg. At this instant, the ship models heel to the starboard side and rotate back to the their vertical position ($\theta_b = 0$ deg). The red color represents positive pressure[1], while the blue one represents negative pressure. The pressure distribution in the left sub-figures is observed from the port side, and the one one the right is viewed from the starboard side. By combining these two sub-figures, we can almost obtain the whole pressure information on both sides of the hull. Since the BK0 model is a bare hull without bilge keels, Fig. 4.8a can be considered to be a baseline for comparison. By comparing the pressure contour of a bilge-keel model with that of the BK0 model, we can investigate the bilge keel effect on the hull pressure.

In Fig. 4.8, we find that for the model without bilge keels, the pressure contour changes continuously and smoothly. There is almost no pressure discontinuity on the hull. Positive pressure exists on the port-side hull, and negative pressure exists on the starboard side. However, for other ship models with bilge keels, pressure discontinuity can be clearly found near the bilge keels, especially in the BK3 model. On the port side of the hull, the bilge keel causes the high pressure to decrease. On the other side of the hull, the bilge keel increases the low pressure, especially in the vicinity of its root.

By integrating the hydrodynamic pressure on the hull surface, we obtain the hydrodynamic moment only acting on the hull, excluding pressure on the bilge keels. The integration results are shown in Fig. 4.9. It can be seen that increasing the bilge-keel span reduces the hydrodynamic moment on the hull. The difference in the moments on the hulls with and without bilge keels can be regarded as the effect of the bilge keels, and it is usually refered to as the hull-pressure moment due to bilge keels. Figure 4.10 shows the hull-pressure moment due to bilge keels, calculated from the

[1]The pressure contour has the unit of Pa.

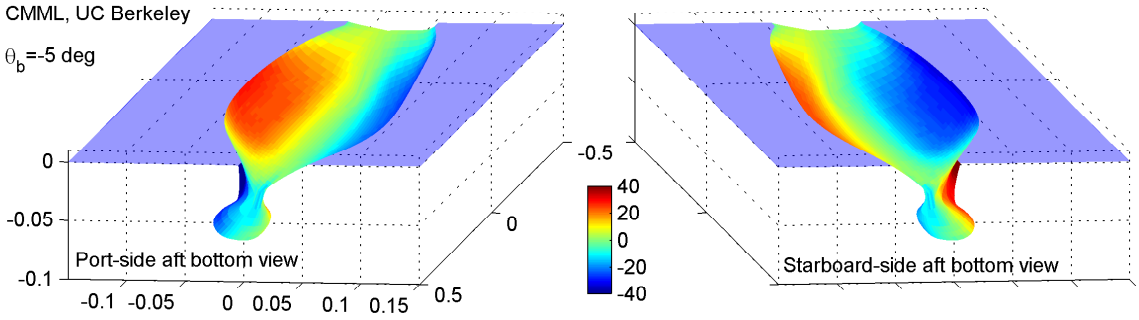

(a) BK0

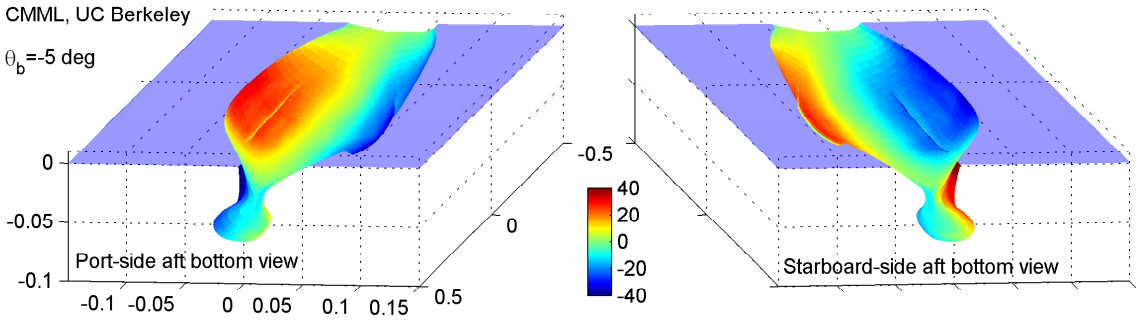

(b) BK1

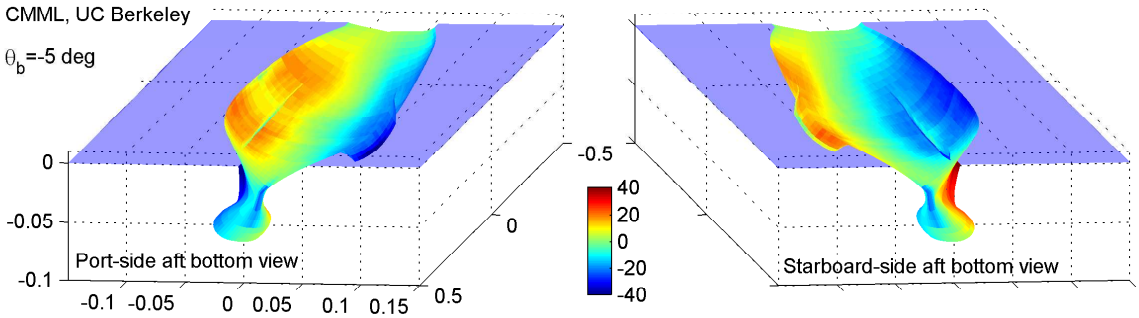

(c) BK2

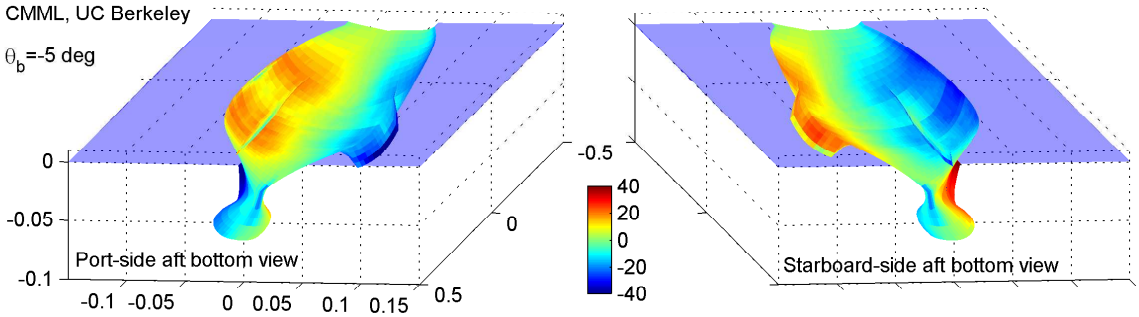

(d) BK3

Figure 4.8: Comparison of hydrodynamic pressures acting on the hulls with different bilge-keel spans in the seventh oscillation.

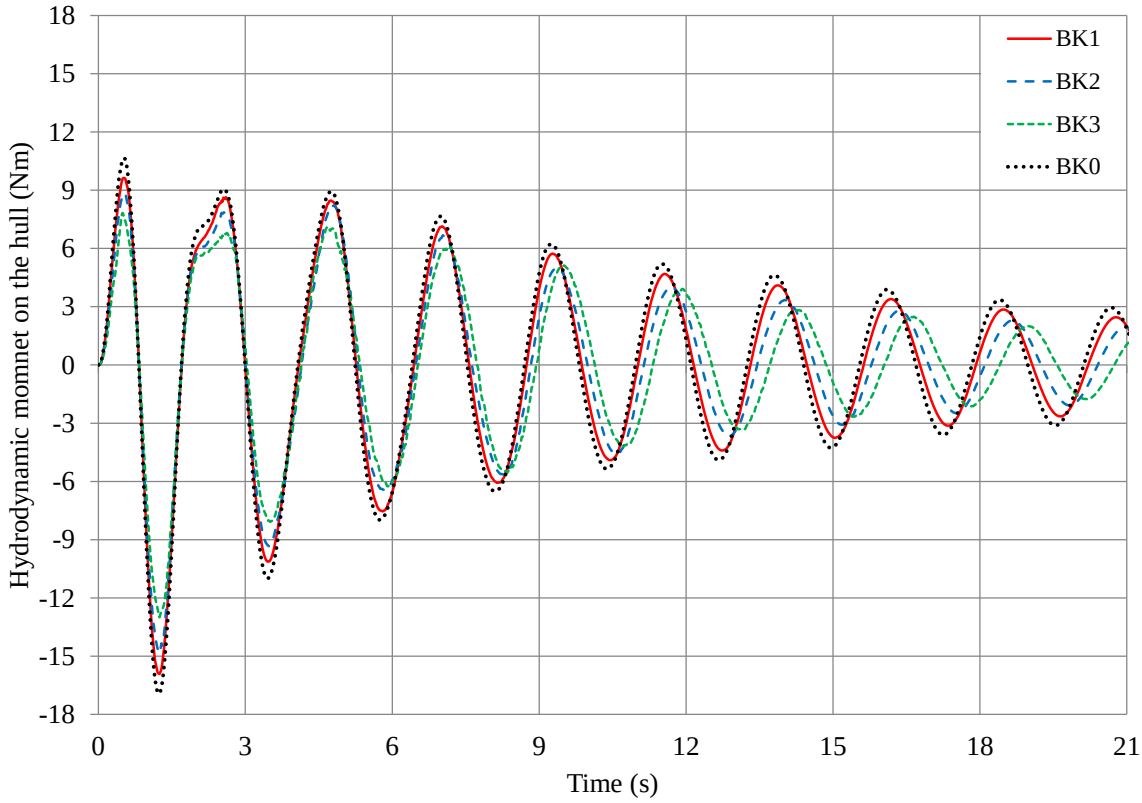

Figure 4.9: Comparison of the time histories of the hydrodynamic moment on the hull between models with different bilge-keel spans.

results shown in Fig. 4.9. We need to note that the hull-pressure moment due to bilge keels shown in the figure includes the effects of the free surface, but it dose not include the contribution from the added moment-of-inertia. Interestingly, it is found that the hull-pressure moment due to bilge keels does not decay with the motion amplitude. The amplitude keeps the same order of magnitude. From the second oscillation to the seventh, the amplitude of this hull-pressure moment due to bilge keels increases for all three bilge-keel models. After the seventh oscillation, the amplitude starts to decrease slowly. These results indicate that the hull-pressure moment due to bilge keels does not depend on the amplitudes of the roll motion nor the angular velocity. This characteristic is different from the bilge-keel moment which is highly dependent on the motion amplitude and angular velocity. In addition, we find that the hull-pressure moment due to bilge keels is approximately proportional to the span of the bilge keels. We believe that the hull-pressure moment due to bilge keels is highly dependent on the hull design and the location and configuration of the bilge keel.

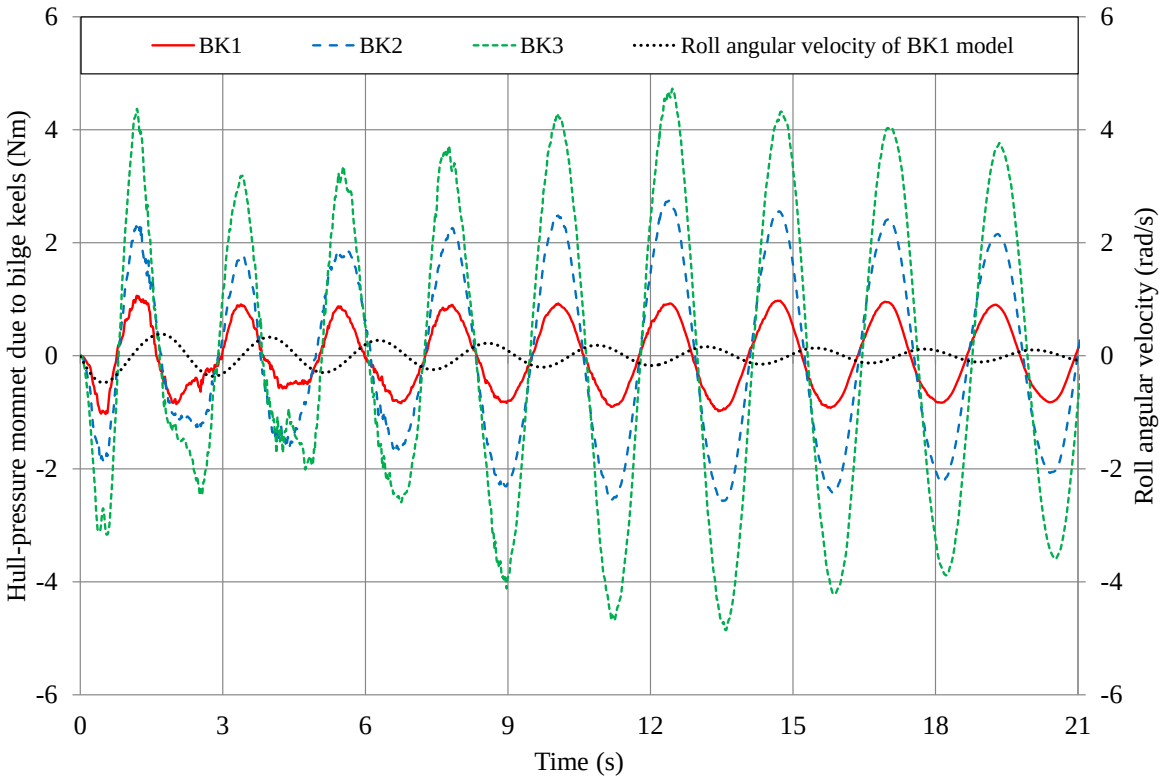

Figure 4.10: Comparison of the time histories of the hydrodynamic moment due to bilge keels between models with different bilge-keel spans.

To investigate the generation of the bilge-keel normal force, Fig. 4.11 shows the hydrodynamic pressure contours on the upper and lower sides of the bilge keels at the same instant of Fig. 4.8. The pressure difference between the upper side and lower sides of the bilge keels is clearly evident in the figure. As shown in Fig. 4.11a, the pressure exerted on the lower side of the starboard bilge keel of the BK1 model is much lower than that exerted on the upper side. Therefore, the pressure difference causes a downward normal force to act on the bilge keel. Consequently, the bilge-keel normal force results in a positive (clockwise) hydrodynamic moment acting on the ship. Since the ship rolls counter-clockwise at the instant of Fig. 4.11a, the positive moment counteracts the roll motion of the ship and performs negative work in this dynamic system. Focusing on the port-side bilge keel, we find that the pressure difference between the upper and lower sides causes an upward normal force and yet, it still results in a positive hydrodynamic moment that dissipates the kinetic energy of the ship. Although we do not show the pressure contours at other instants, we find that the pressure differences on both bilge keels generate hydrodynamic moments that oppose the direction of the roll angular velocity. Those moments perform negative

work as the ship rolls. This property reveals the working mechanism of bilge keels on reducing the roll motion.

The contours in Figs. 4.11b and 4.11c mainly show the same pattern of the pressure distributions as that in Figs. 4.11a. By comparing the pressure difference among different ship models, we find that the pressure on each side of the bilge keels has approximately the same value. Therefore, the normal force on a bilge keel should be proportional to its span. This point will be examined in the following seciton.

4.5 Bilge-keel normal force and moment

The time histories of the hydrodynamic normal forces acting on the port-side and starboard-side bilge keels are shown in Figs. 4.12 and 4.13, respectively. It can be seen that the larger bilge keels experience much greater hydrodynamic normal forces. Increasing the bilge keel span amplifies the normal force dramatically. The maximum and minimum values of the normal forces in each oscillation are nearly proportional to the bilge-keel spans. Furthermore, it is found that the normal forces acting on the BK1 model is 180 degrees out of phase with the roll angular velocity. This feature is also found in the other two models, though their roll angular velocities are not shown in the figures. The positive direction of the normal force in the two figures is defined to be driving the ship roll positively. Thus, as described previously, the normal forces perform the negative work and consume the kinetic energy of the ship during the decay process. The mechanism of this passive stability system, bilge keels, is directly evident here.

Figures 4.14 and 4.15 show the time histories of the hydrodynamic moment on the port-side and starboard bilge keels. Similarly, the roll angular velocity of the BK1 model is also included in the two figures. As expected, the hydrodynamic moment is 180 degrees out of phase with the roll angular velocity. Thus, the bilge-keel hydrodynamic moment does the negative work on the ship and causes its roll motion to decay. This bilge-keel hydrodynamic moment has been widely simulated by a quadratic damping term. In the following, we will discuss whether this quadratic damping term is accurate enough.

In the ocean engineering field, the drag force on a bluff body in oscillatory motion is normally computed by the following equation:

$$F_D = C_D \frac{1}{2} \rho S U_b |U_b|, \tag{4.3}$$

where F_D represents the drag force, C_D the drag coefficient, S the area of the body projected on the crossplane normal to the direction of motion, and U_b the velocity of motion. This equation has been applied to simulate the bilge-keel normal force. Correspondingly, the bilge-keel hydrodynamic moment caused by the bilge keel normal force can be computed through $-B_2\dot{\theta}_b|\dot{\theta}_b|$, where B_2 is known as the quadratic damping coefficient. In order to verify whether the assumption of the quadratic form is accurate enough, we plot the roll velocity square parameter[2] $-\dot{\theta}_b|\dot{\theta}_b|$ with the port-side and starboard-side bilge-keel moments in Figs. 4.16 and 4.17 for the BK1 model. If the bilge-keel hydrodynamic moment is proportional to $-\dot{\theta}_b|\dot{\theta}_b|$, it means that there exists a constant quadratic damping coefficient which can be used to simulated the bilge-keel moment. From Figs. 4.16 and 4.17, we find that a quadratic damping coefficient which can be used to calculate the bilge-keel hydrodynamic moment during the whole decay process does not exist. However, after the forth oscillation, the bilge-keel hydrodynamic moment is approximately proportional to $-\dot{\theta}_b|\dot{\theta}_b|$. Therefore, the hydrodynamic bilge-keel moment has a quadratic form starting from the forth oscillation, as shown in Fig. 4.5.

[2]The unit of $\dot{\theta}_b$ in the figure is rad/s.

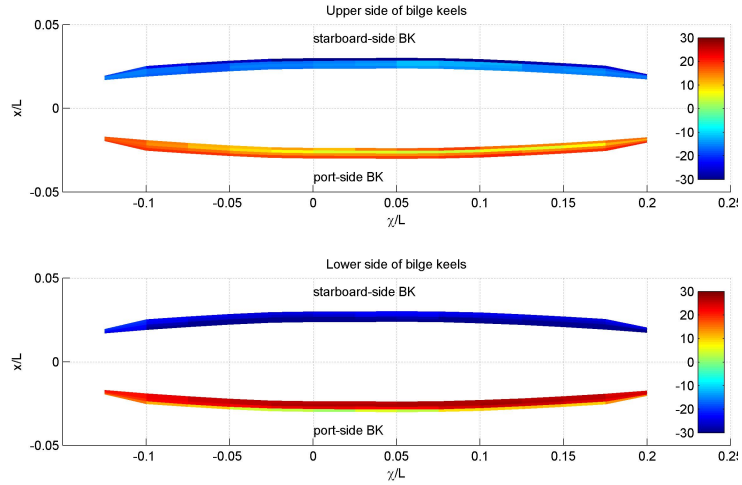

(a) BK1

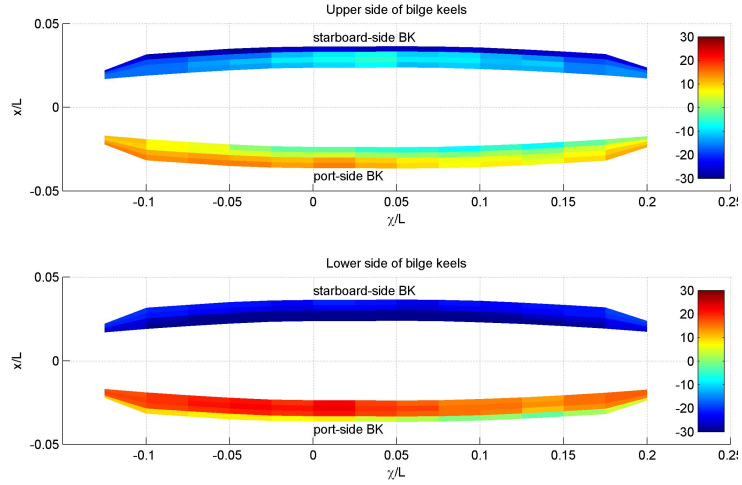

(b) BK2

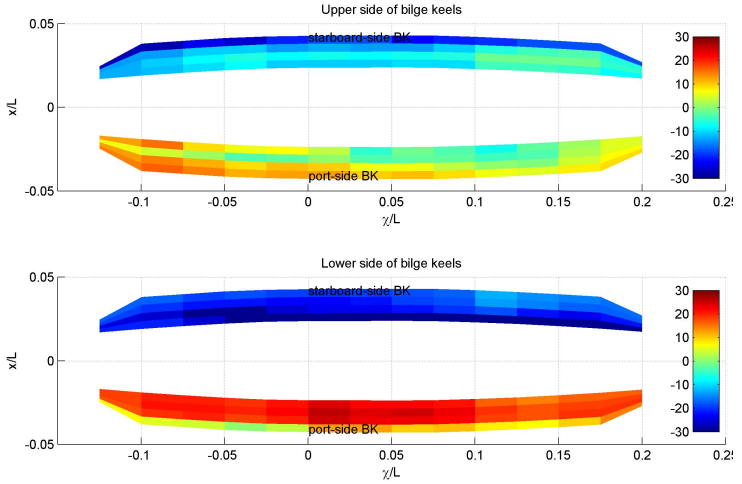

(c) BK3

Figure 4.11: Comparison of hydrodynamic pressures acting on bilge keels in the seventh oscillation.

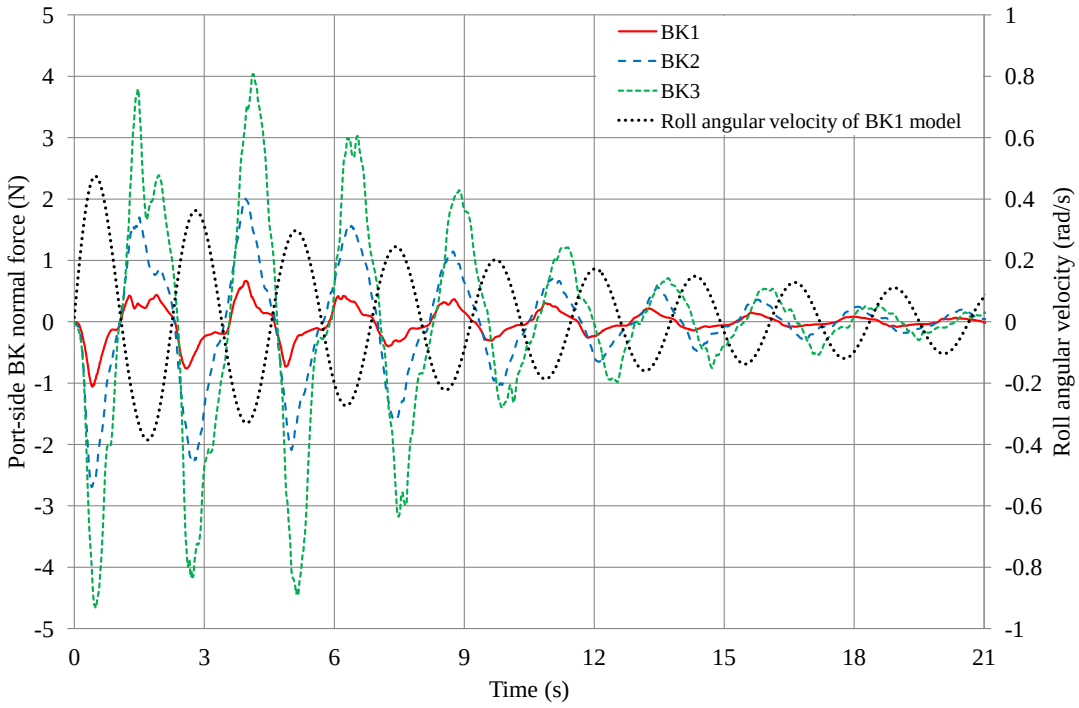

Figure 4.12: Comparison of the time histories of the hydrodynamic normal force on the port-side bilge keel between hulls with different bilge-keel spans.

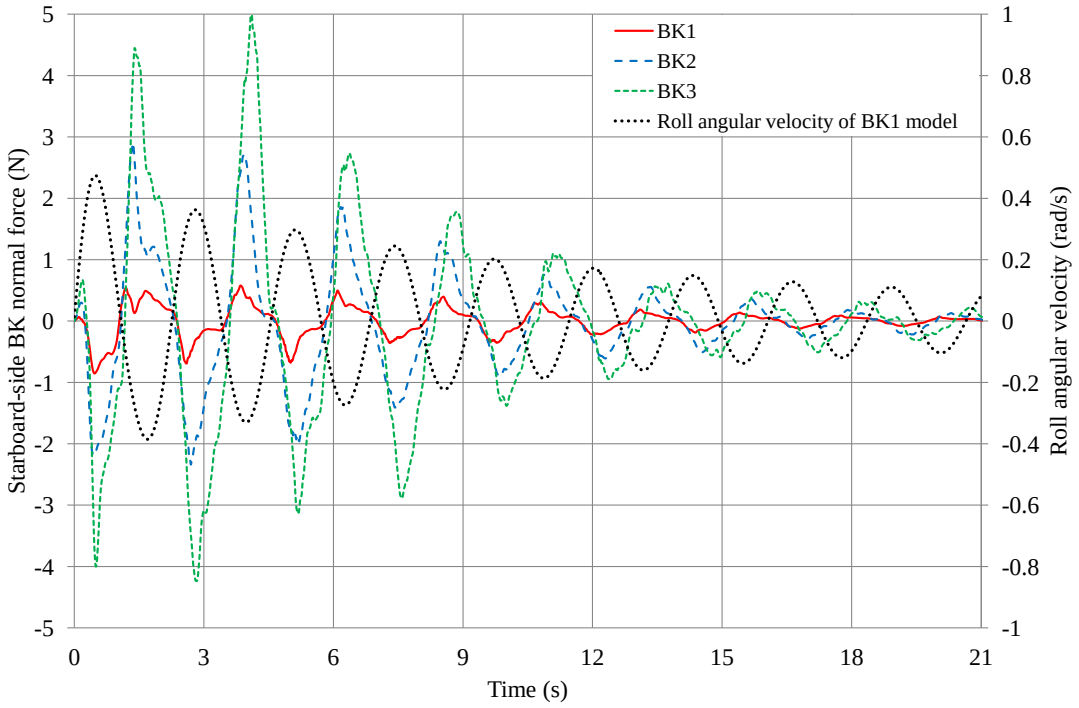

Figure 4.13: Comparison of the time histories of the hydrodynamic normal force on the starboard-side bilge keel between hulls with different bilge-keel spans.

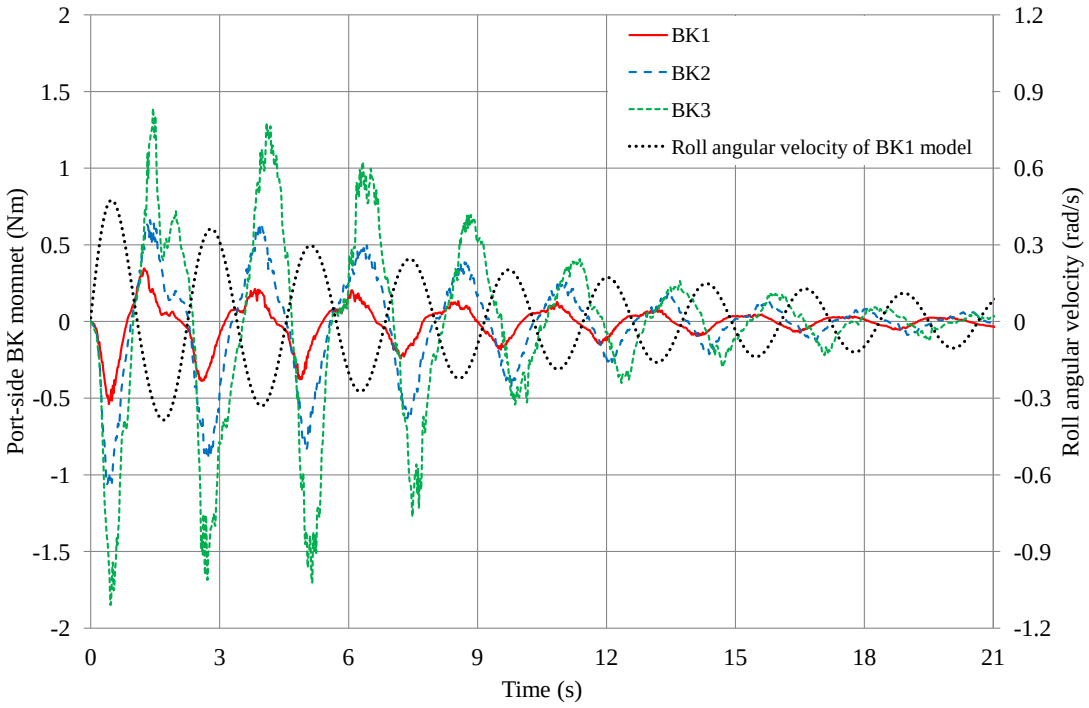

Figure 4.14: Comparison of the time histories of the hydrodynamic moment on the port-side bilge keel between hulls with different bilge-keel spans.

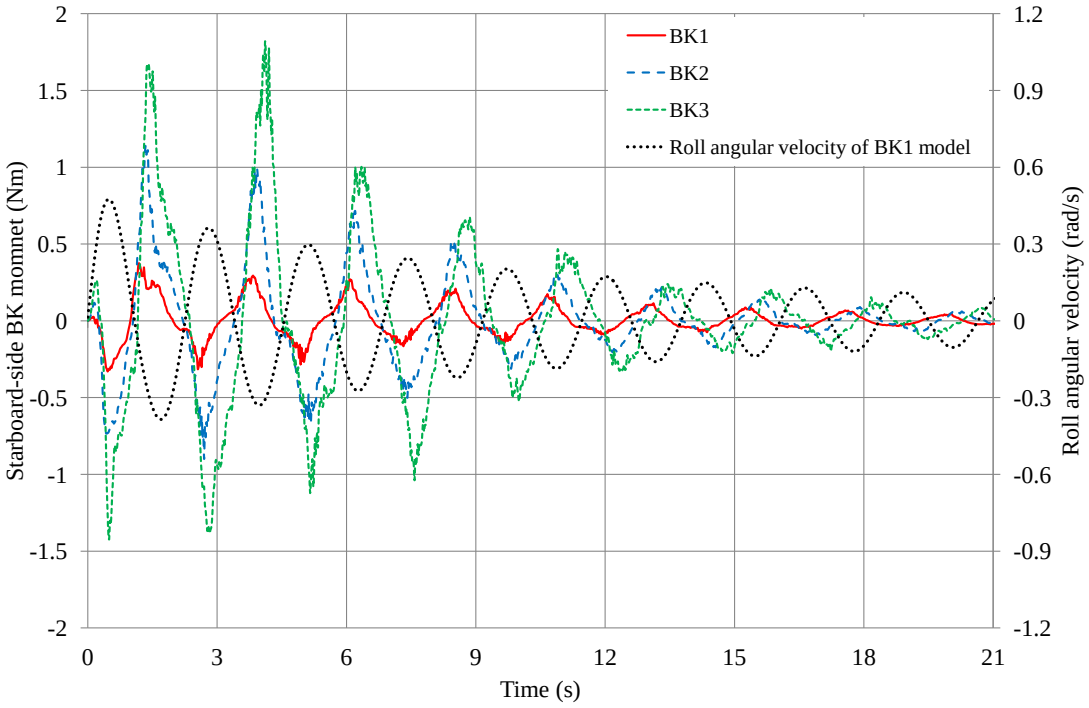

Figure 4.15: Comparison of the time histories of the hydrodynamic moment on the starboard-side bilge keel between hulls with different bilge-keel spans.

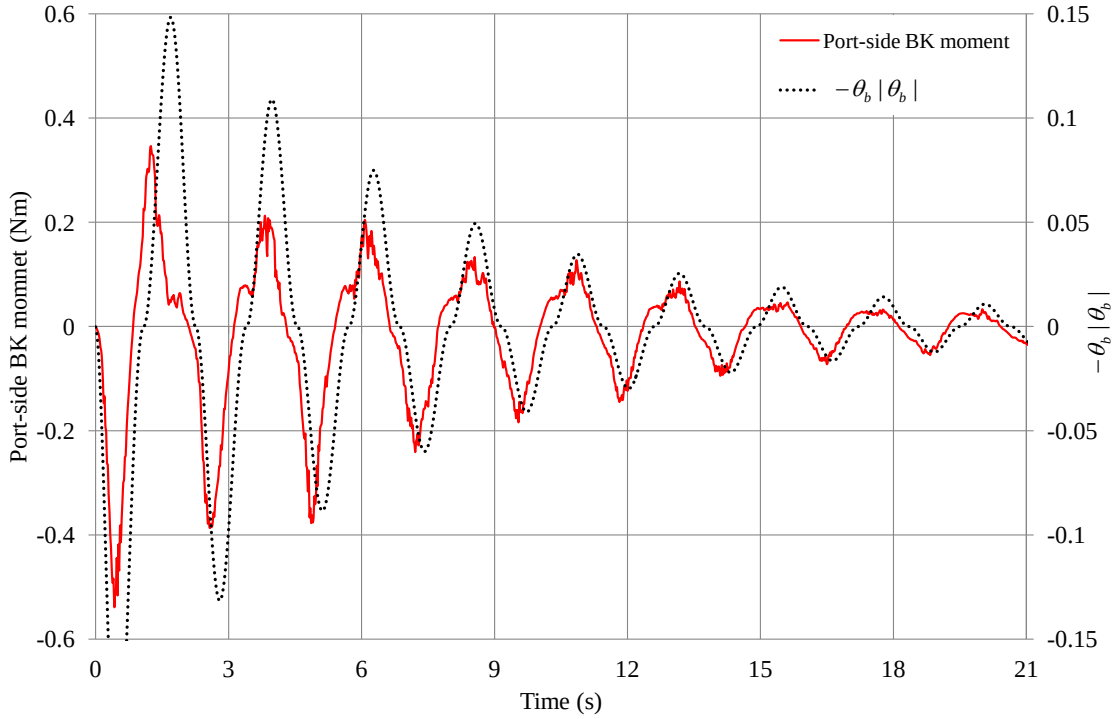

Figure 4.16: Time histories of the hydrodynamic moment on the port-side bilge keel and the value of $-\dot{\theta}_b|\dot{\theta}_b|$ for the BK1 model.

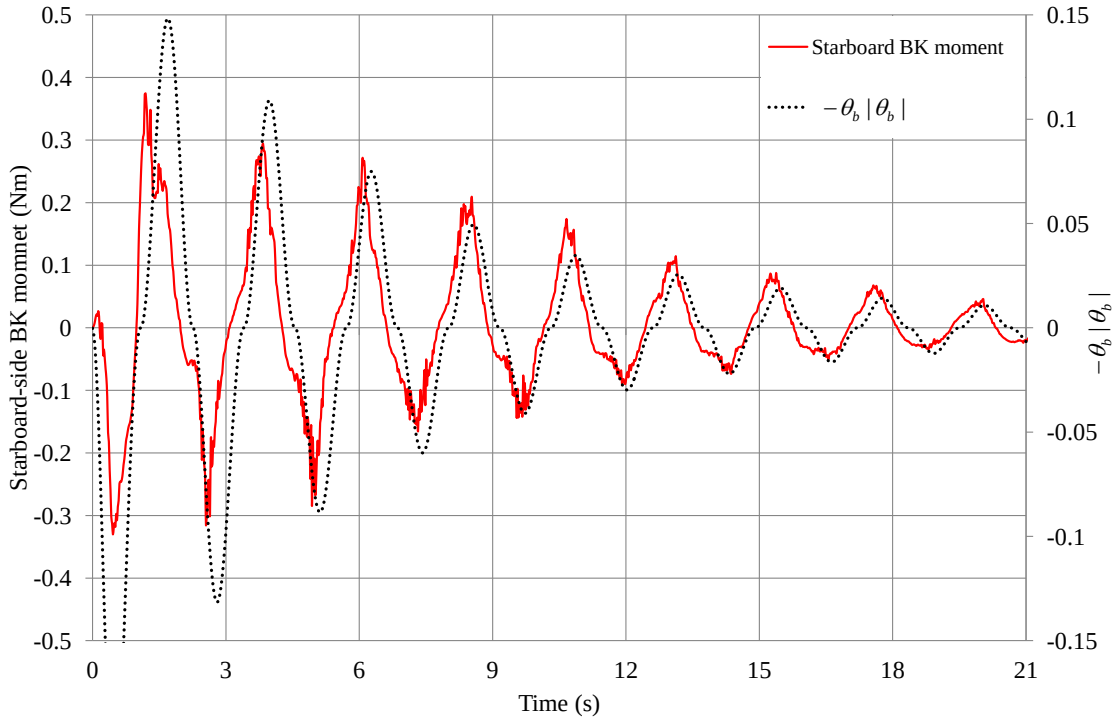

Figure 4.17: Time histories of the hydrodynamic moment on the starboard-side bilge keel and the value of $-\dot{\theta}_b|\dot{\theta}_b|$ for the BK1 model.

4.6 Surface waves

To complete our study on the effects of bilge keels, we examine the surface waves generated by ship models with different bilge-keel spans and compare them in this section. Figure 4.18 shows the comparison of surface waves from the top view among hulls with different bilge-keel spans in the second half of the first oscillation. Columns from left to right in the figure represent BK0, BK1, BK2, and BK3 models, respectively. All lengths and wave elevations are normalized by the body length. The gray level on the surface denotes the wave elevation, while the white and black colors represents peaks and troughs respectively.

In this figure, the motion of the roll-induced waves are clearly revealed. Troughs and peaks are first generated near the hull and then propagate away. As they travel away from the hull, their heights decay gradually. The differences in the roll-induced waves among different models are not significant. Therefore, we believe that the wave damping due to bilge keels is small and can be neglected for this type of hull. Himeno also drew a similar conclusion based on experimental results. In his paper from 1981, Himeno wrote, "It can be noted that for bilge keels with ordinary breadth of B/60 to B/80, we can safely neglect the wave effect of bilge keels, since the contribution of this component is usually quite small compared to the viscous damping caused by bilge keels."

4.7 Roll response in waves

In this section, an oscillating pressure patch is used to generate regular incident waves on the starboard-side free surface. The wave height is chosen to be 2.48 cm, which is 10% of the draft of the ship hull, and the wave period is 2.25 s. In order to study the bilge keel effect on the roll motion, the ship can only roll freely in waves with other motions being constrained.

Figure 4.19 shows the time histories of the roll responses among hulls with different bilge keel spans. Since the wave period is close to the roll resonance period of the vessels, the roll motion ramps up rapidly, and the motion amplitudes are quite large in steady state. Through the comparison of the responses among these four models, we find that the roll amplitude in the steady state decreases with increase of the bilge-keel size. The largest bilge keels reduce the motion amplitude most significantly. Compared to the BK0 model, the motion amplitudes of the BK1, BK2, and BK3 models are reduced by 6%, 11%, and 32%, respectively.

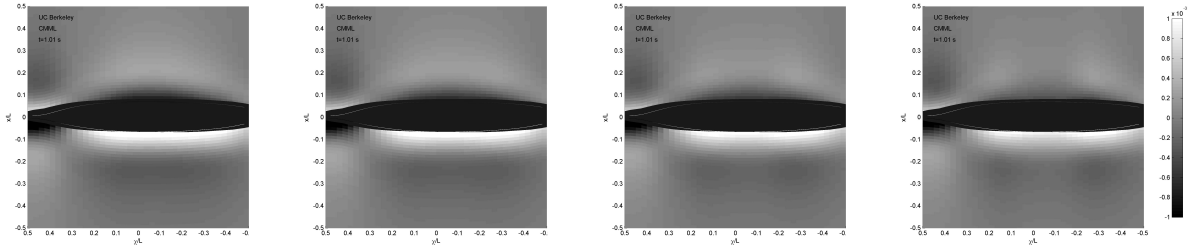

(a) t=1.01 sec.

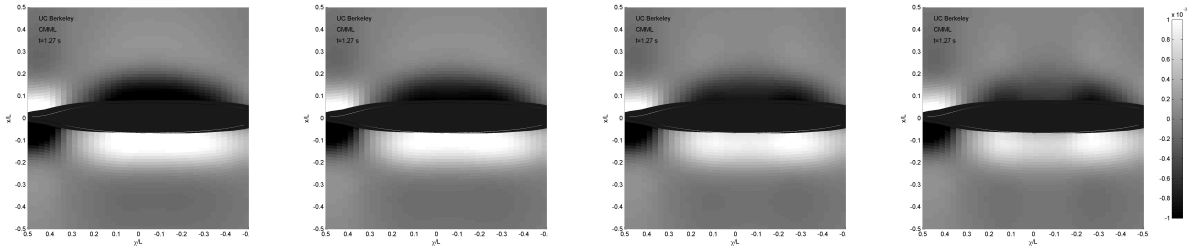

(b) t=1.27 sec.

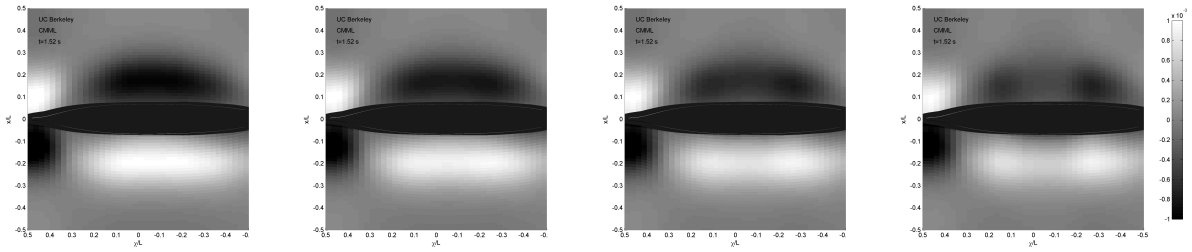

(c) t=1.52 sec.

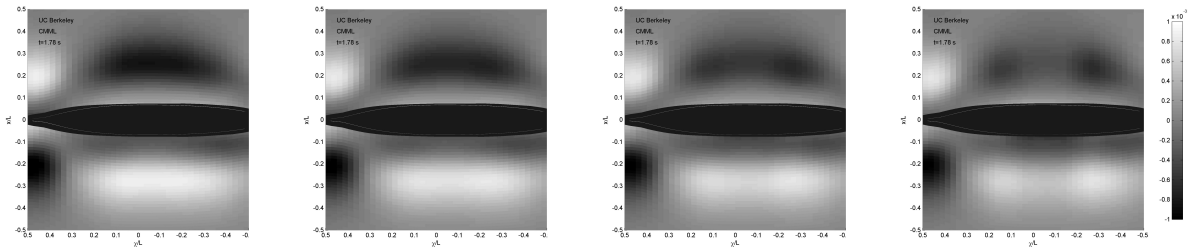

(d) t=1.78 sec.

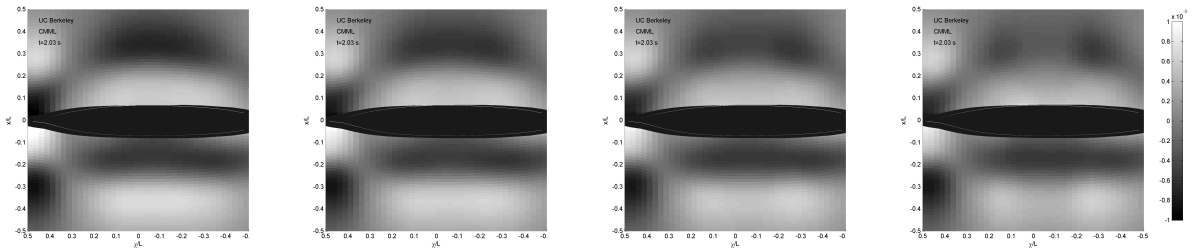

(e) t=2.03 sec.

Figure 4.18: Comparison of surface waves from the top view between hulls with different bilge-keel spans. Columns from left to right represent BK0, BK1, BK2, and BK3 models, respectively.

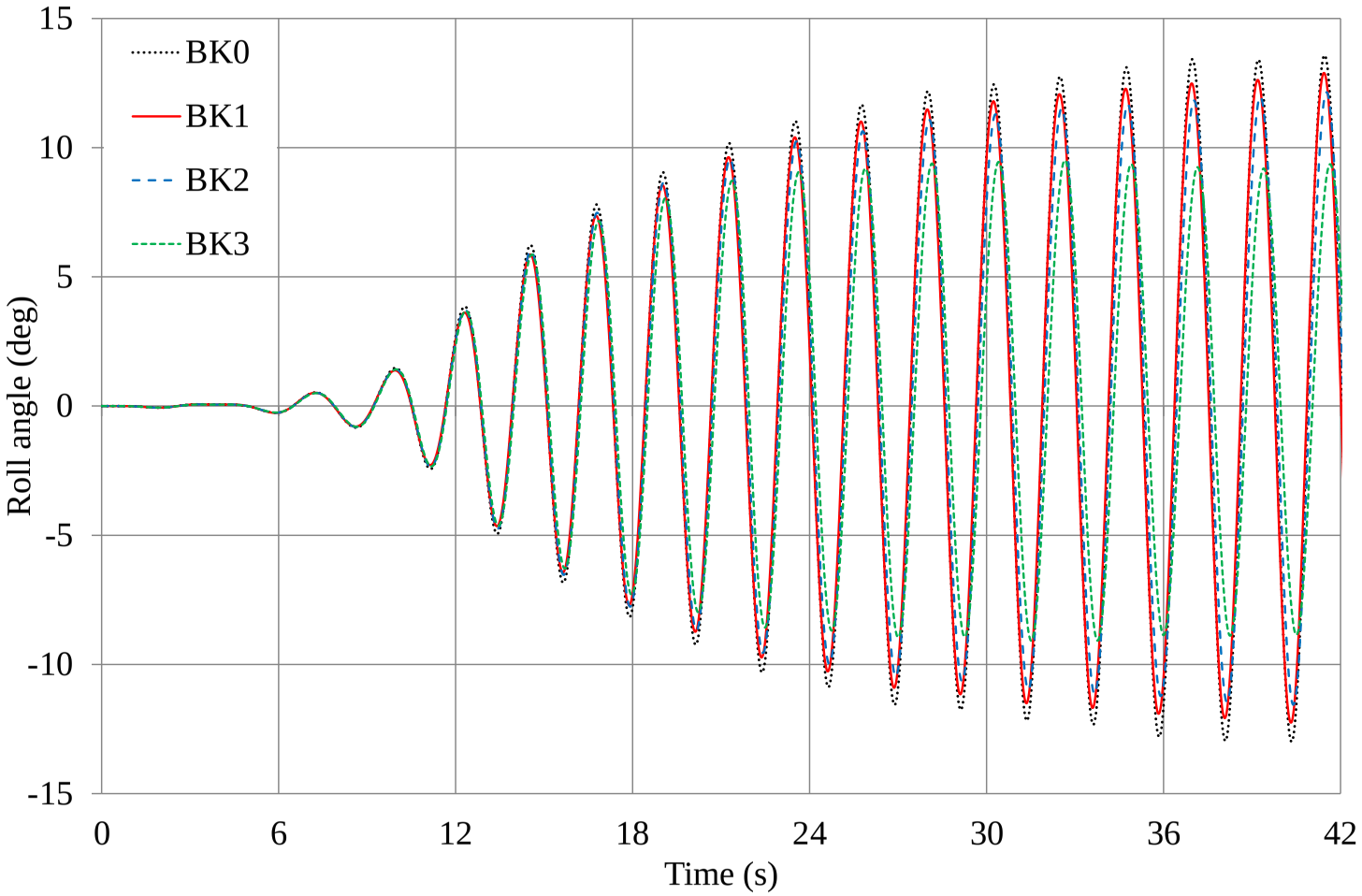

Figure 4.19: Comparison of the time histories of the roll response in waves between hulls with different bilge-keel spans.

This page intentionally left blank.

Chapter 5

Effects of Forward Speed

Unlike offshore platforms, ships are on the move because of their nature of operation. The flow field in the vicinity of a vessel is altered by the presence of the forward speed. This chapter examines the influence of the hull speed on the roll motion by taking into account various hull speeds, including a zero speed case.

Two sections are included in this chapter. In the first section, we will compare the roll time histories, decay coefficients, hydrodynamic pressures, and hydrodynamic moments between a forward speed case and a zero speed case. In the second section, the emphasis will be placed on the effect of different forward speeds. The effectiveness of SSFSRVM in simulating the free roll motion of a vessel with different hull speeds will be examined by comparing simulation results and experimental measurements. Then, the roll decay coefficients and surface waves will be presented.

5.1 Forward speed versus zero speed

Aloisio & Felice (2006) carried out the decay tests with and without forward speed at the INSEAN towing tank n°2. As shown in Chapter 3, we simulated these two cases numerically and accurately predict the roll motion. In this section, we will compare these two cases from different aspects, in order to investigate the effect of hull speed.

5.1.1 Roll time history and decay coefficient

Figure 5.1 presents the comparison of the roll time histories between these two cases, $Fr = 0$ and $Fr = 0.138$, resulting from the SSFSRVM simulations. For the case of $Fr = 0.138$, the roll motion decays much faster during the decay test, and the

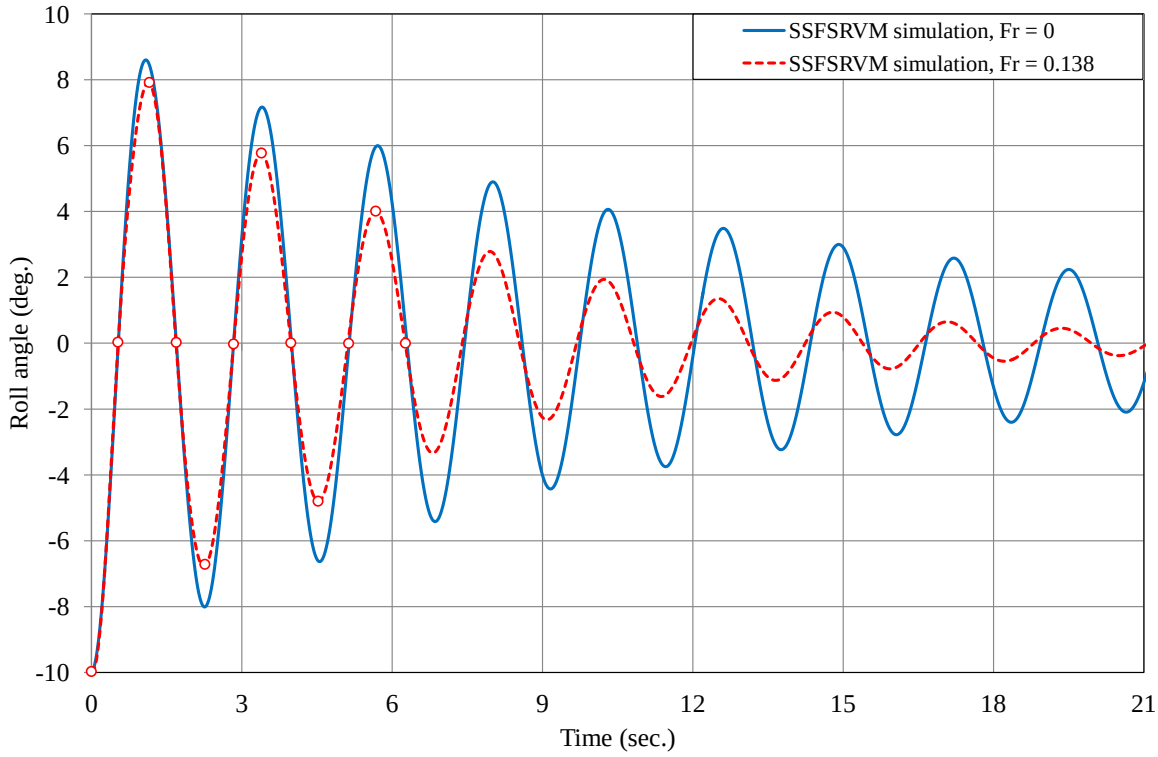

Figure 5.1: Time histories of the roll motion resulting from the SSFSRVM simulations for $Fr = 0$ and $Fr = 0.138$.

roll period is slightly smaller. These results indicate that the presence of hull speed increases the roll damping but slightly affects the added moment-of-inertia.

Figure 5.2 shows the roll decay coefficient versus mean roll angle resulting from the time histories in Fig. 5.1. The decay coefficient of the case $Fr = 0.138$ is nearly two times of that of the zero speed case. Additionally, the hull speed also alters the curve trend of the decay coefficient. The nonlinear characteristic of the decay coefficient found in the case of $Fr = 0$ has been eliminated by the addition of forward speed. When the mean roll angle is between 1 deg and 4.4 deg, the value of the decay coefficient is almost uniform. This indicates that the quadratic damping component is trivial, and the linear damping dominates. In section 4.5, we have found that the quadratic damping comes from the effect of bilge keels. Therefore, we believe that the effect of bilge keels on an advancing moving ship is not as strong as that on a zero-speed ship. Based on the results shown in Fig. 5.2, we conclude that the addition of hull speed significantly increases the linear damping but decreases the quadratic damping.

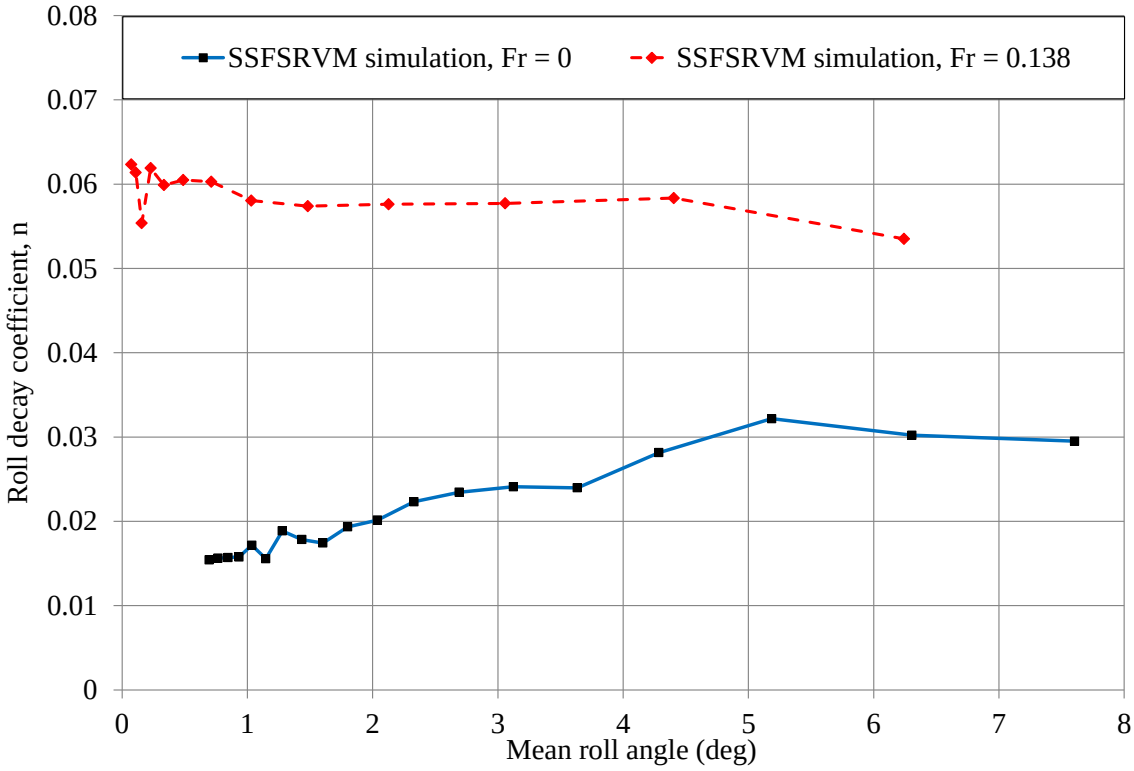

Figure 5.2: Roll decay coefficients versus mean roll angles resulting from the SSFS-RVM simulation for $Fr = 0$ and $Fr = 0.138$.

5.1.2 Flow along the three-dimensional hull

Figure 5.3 shows a quarter-period time sequence of the axial vorticity contours and vorticity iso-surfaces during the first cycle of roll decay motion for the case of $Fr = 0.138$. The ship is viewed from a perspective under the free surface. Times are selected to correspond with the peaks and zero crossing of the roll motion as shown in Fig. 5.1 (see the round markers). At the moment of Fig. 5.3a, the ship model has pierced in calm water with a constant hull speed of 1.03 m/s and with a constant roll angle of $R_0 = -10°$ for about 5 seconds. The static heel and the forward motion result in the vorticity filament emanating from the sonar dome. At this moment, no significant vortical structures are found near the bilge keels. After the model is released to roll freely (see Fig. 5.3b), two positive vortex filaments are generated by the bilge keels. With the ship continuing to roll in the same direction, the vortex filaments roll up and are convected downstream because of the forward speed. Additionally, the rolling motion of the sonar dome combined with the forward motion of the hull starts to produce a curvy sonar-dome vortex filament with positive vorticity. In Fig. 5.3c, it is found that the sonar-dome vortex filament separates into two parts.

The lower part of the sonar-dome vortex filament interacts with the previously generated negative vortex filament. Near the rear half part of the bilge keels (located at $0.5 < \chi/L < 0.7$), two new bilge-keel vortex filaments with negative vorticity appear. Accompanied by the older positive filaments, two counter-rotating vortex pairs emerge. Thus, three vortex pairs can be found in Fig. 5.3c. During the next quarter rolling cycle, the interaction of these vortex pairs rapidly mixes their energy and decreases their strengths. Eventually, they will split into parts and then disappear into the surrounding fluid. When the ship reverses its direction (see Fig. 5.3d), two negative vortex filaments emerge near the front half part of bilge keels. In addition, a newly generated sonar-dome vortex can be also found near the bow. The newly generated vortex filaments will continue to increase their length and strength, since the ship rolls in the same direction.

Figures 5.4 and 5.5 show a quarter-period time sequence of the three-dimensional flow during the second and third cycles of the roll decay motion. In these two cycles, the motion pattern of the vortex filaments described previously repeats with each successive roll cycle. Positive and negative sonar-dome vortex filaments are generated alternately and convected downstream under the hull. The combination of the rolling motion of the sonar dome and the forward motion results in a long curvy sonar-dome vortical structure (see Fig. 5.4d). This curvy structure is comprised of several alternating positive and negative vortex filaments. The two connected vortex filaments interact with each other, since they have different rotation directions. The interaction dissipates their energy and results in disturbed flow in the adjacent area. Additional, the sonar-dome vortex filament decays by itself as it is convected downstream. For instance, the very strong vortex filament near the dome in Fig. 5.4a shows smaller and smaller length and core size in Figs. 5.4b-c. In Fig. 5.5d, the vortex filament eventually splits into parts and merges into the wake.

With respect to the bilge-keel vortex filaments in Figs. 5.4 and 5.5, we find that the vorticity strength of the newly generated bilge-keel vortex filament deceases as the amplitude of roll motion decays in time. Starting from the third oscillation of the roll motion, there is almost no strong vortex filament generated by bilge keels. In addition, the newly generated vortex filaments are convected downstream very fast. Therefore, they can only affect the hydrodynamic pressure on bilge keels for a short period of time. Based on these facts, we deduce that the effects of the bilge keels in the case of $Fr = 0.138$ are not as strong as those in the zero-speed case. Therefore, we found a linear behavior of the decay coefficient in Fig. 5.2.

In summary, in the presence of ship forward speed, the sonar-dome and bilge-keel vortices are convected away downstream fast. They do not stay long enough to affect the pressure distribution on the hull and bilge keels. Consequently, the quadratic damping component of the ship decreases significantly.

5.1.3 Hydrodynamic pressure on bilge keels

Figure 5.6 shows a quarter-period time sequence of the hydrodynamic pressure acting on bilge keels during the first and a half cycle of roll decay motion for the case of $Fr = 0.138$. Times are also selected to correspond with the peaks and zero crossing of the roll motion as shown in Fig. 5.1. Focusing on each side of the bilge keels, we find the pressure varies in the longitudinal direction χ due to the presence of forward speed. But the pressure distribution on a bilge keel is very uniform along the longitudinal direction in the case of zero hull speed (see Fig. 4.11). Additionally, we find that the presence of forward speed significantly increases the range of the bilge-keel hydrodynamic pressure. However, the pressure difference between the upper and lower sides of a bilge keel in the case of $Fr = 0.138$ is a much smaller than those in the case of $Fr = 0$ (see Fig. 4.11). This indicates that the hydrodynamic moment provided by bilge keels will be smaller. In the next section, we will confirm this result.

5.1.4 Hydrodynamic moment acting on bilge keels

Figure. 5.7 presents the comparison of the hydrodynamic moment acting on the port-side bilge between these two cases, $Fr = 0$ and $Fr = 0.138$. As expected, the port-side bilge keel provides much smaller hydrodynamic moment in the case of $Fr = 0.138$ than those in the case of $Fr = 0$. In addition, for $Fr = 0.138$ we find that the bilge-keel hydrodynamic moment not 180° out of phase with the roll angular velocity. In Fig. 5.8, these phenomena can be also found with respect to the starboard-side bilge keel. Combining these results, we believe that the bilge keels in the case of $Fr = 0.138$ do not provide much quadratic damping for the ship. Therefore, as previously stated, the corresponding decay coefficient should not vary much over the range of x-axis, which confirmed in Fig. 5.2.

Focusing on the time history of the bilge-keel moment in the case of $Fr = 0.138$ in Fig. 5.7, we find a large trough distinctly showing up at $t = 0.55$ sec. This trough provides us with an opportunity to investigate what causes large bilge-keel moment. By examining the vorticity fields in Figs. 5.3-5.5, we find that the longest and strongest

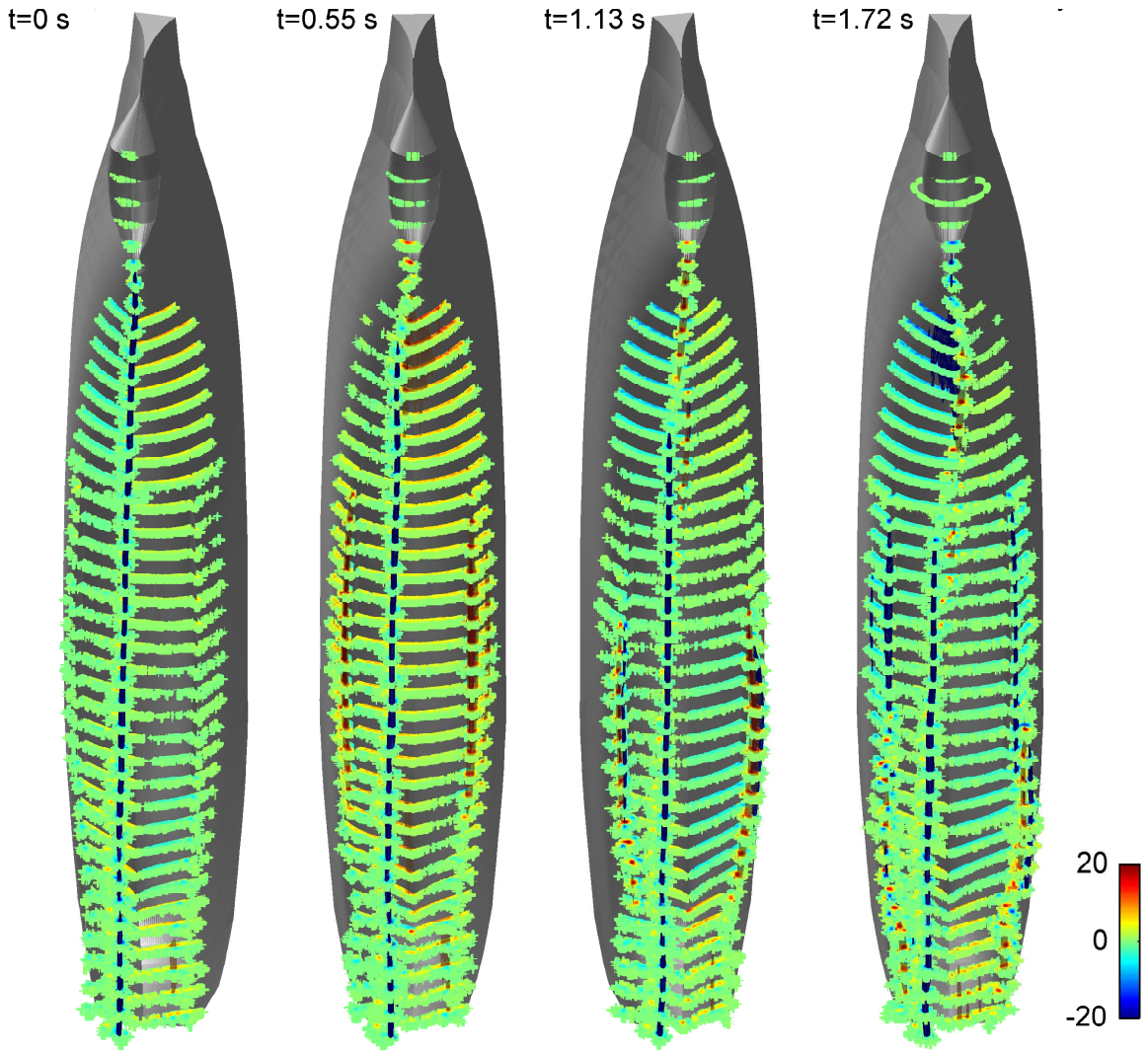

(a) $t = 0$ sec. (b) $t = 0.55$ sec. (c) $t = 1.13$ sec. (d) $t = 1.72$ sec.

Figure 5.3: Quarter-period time sequence of axial vorticity contours and vorticity iso-surfaces along the 5415 model during the first oscillation for the case of $Fr = 0.138$.

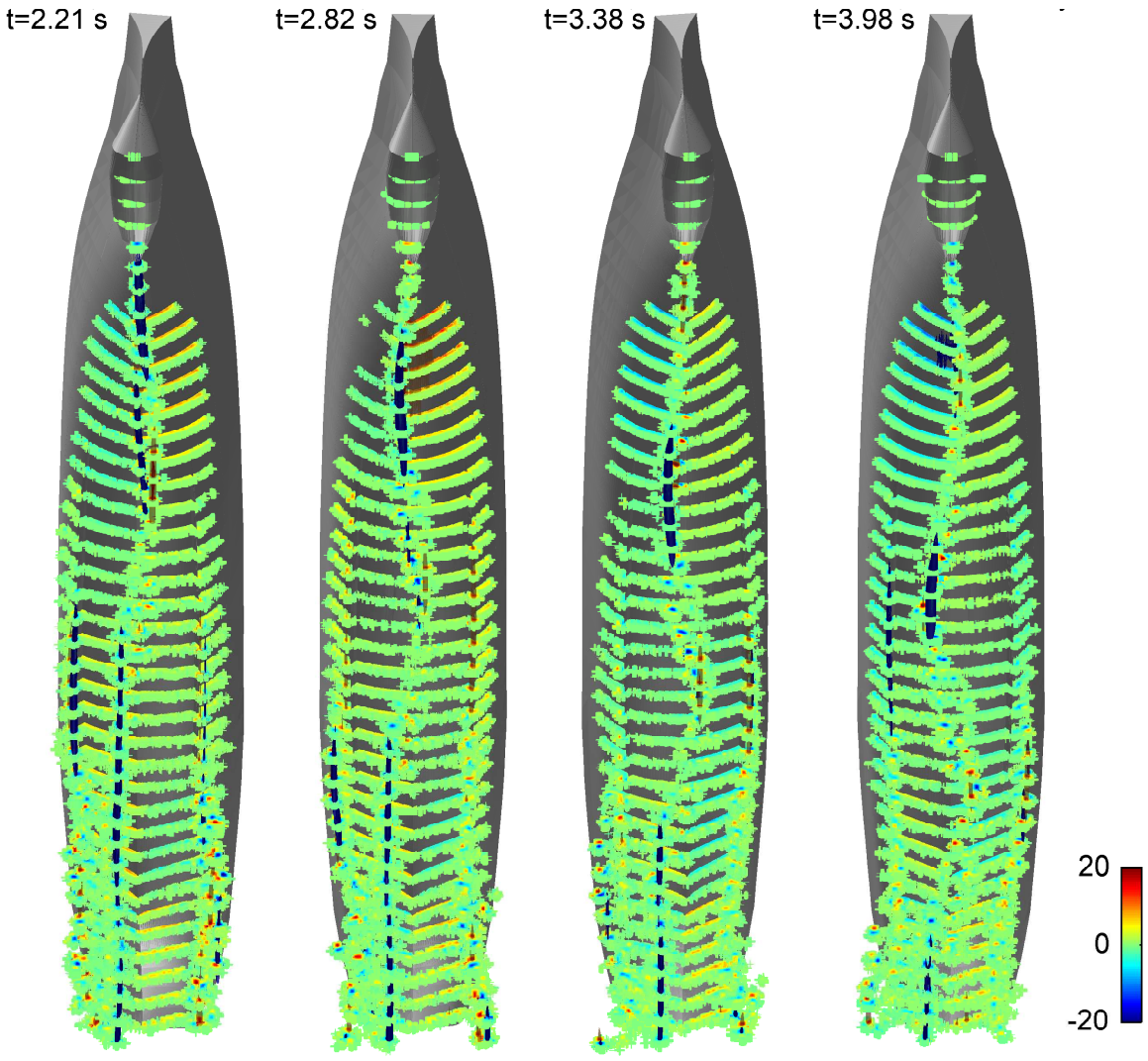

(a) $t = 2.21$ sec. (b) $t = 2.82$ sec. (c) $t = 3.38$ sec. (d) $t = 3.98$ sec.

Figure 5.4: Quarter-period time sequence of axial vorticity contours and vorticity iso-surfaces along the 5415 model during the second oscillation for the case of $Fr = 0.138$.

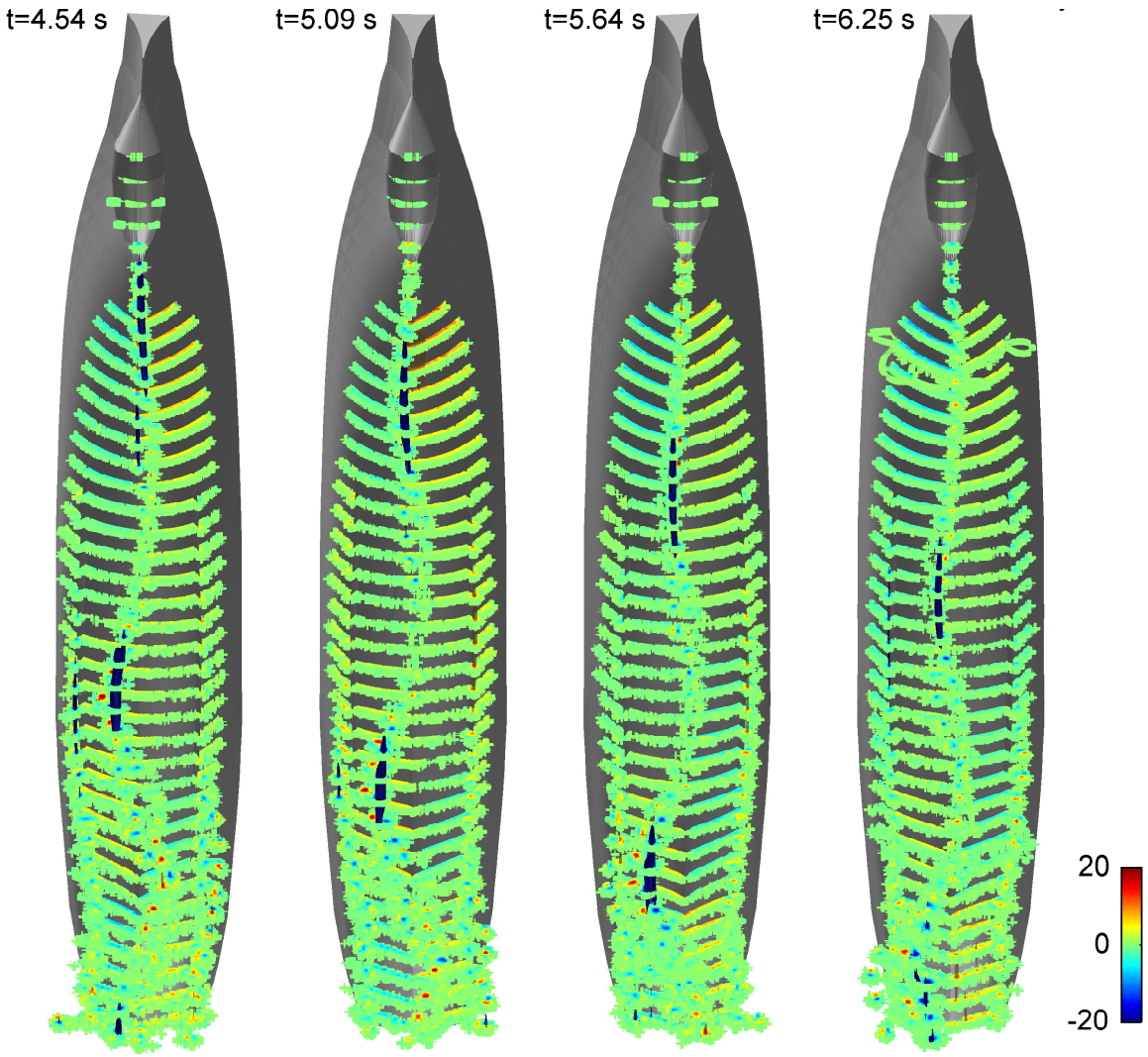

(a) $t = 4.54$ sec. (b) $t = 5.09$ sec. (c) $t = 5.64$ sec. (d) $t = 6.25$ sec.

Figure 5.5: Quarter-period time sequence of axial vorticity contours and vorticity isosurfaces along the 5415 model during the third oscillation for the case of $Fr = 0.138$.

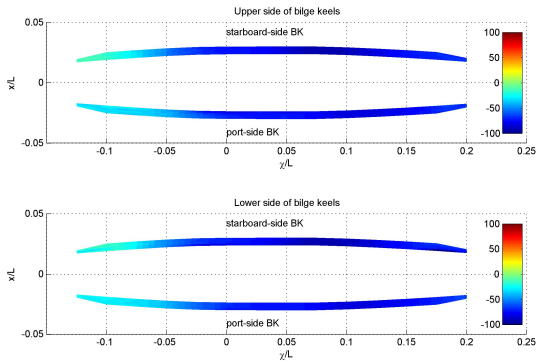

(a) $\theta_b = -10$ deg.

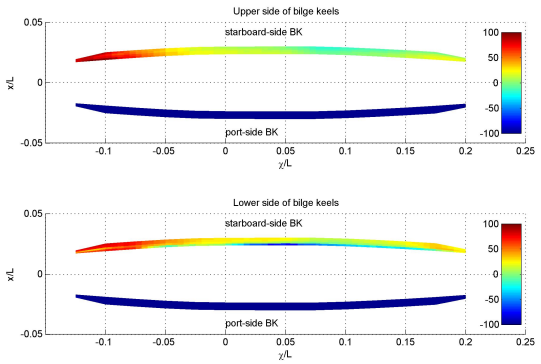

(b) $\theta_b = 0$ deg.

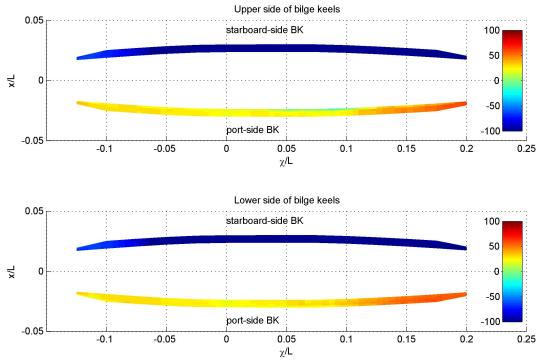

(c) $\theta_b = 7.9$ deg.

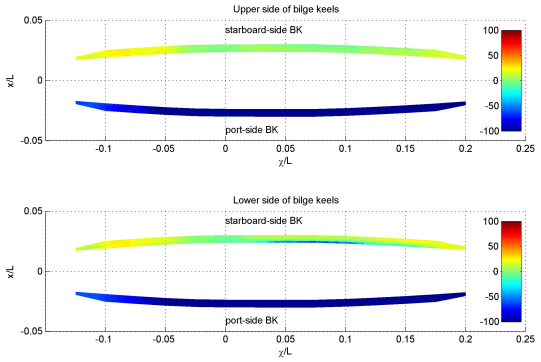

(d) $\theta_b = 0$ deg.

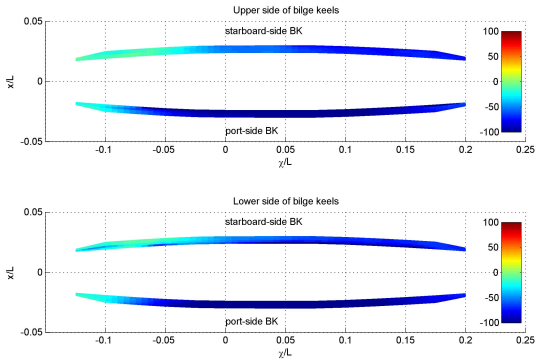

(e) $\theta_b = -6.8$ deg.

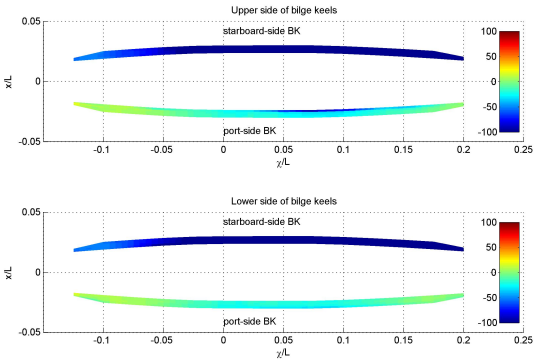

(f) $\theta_b = 0$ deg.

Figure 5.6: Quarter-period time sequence of the hydrodynamic pressure acting on bilge keels.

Table 5.1: Geometric and hydrostatic parameters of DTMB model 5412.

Parameter	Units	5512
Linear scale ratio	–	46.6
Length L	m	3.048
Beam B	m	0.405
Draft T	m	0.132
Wetted surface area S_w	m^2	1.459
Block coefficient C_B	–	0.506
Metacentric height GM	m	0.043
Roll radius of gyration $k_{44} = 0.39B$	m	0.158
Natural roll period	s	1.54

vortex filament generated by the port-side bilge keel appears at $t = 0.55$ sec (see Fig. 5.3b). This result indicates that the large hydrodynamic moment on the port-side bilge keel is induced by the strong vortex filament. Therefore, we conclude that the vortex filament generated by the bilge keel will alter pressure distributions on the upper and lower sides of the bilge keel, resulting in a larger bilge-keel hydrodynamic moment.

5.2 Effects of different forward speeds

Irvine *et al.* (2013) provided a set of benchmark experimental data for the validation of CFD codes for roll decay with forward speed in calm water. The tests were conduted in the IIHR towing tank. An 1:46.6 scale, L = 3.048 DTMB 5412 model with bilge keels was used in the experiments. Model-scale geometric and hydrostatc parameters are summarized in Table. 5.1. The published experimental data includes the roll motion of the DTMB 5212 model with three different forward speeds, corresponding to the Froude numbers of 0.138, 0.280 and 0.410, respectively. Local flow measurements are performed for phase-averaged wave pattern and bilge keel velocity field for $Fr = 0.138$, $\phi_0 = 10°$.

In this section, we will first examine the effectiveness of SSFSRVM on simulating different forward speeds by comparing the time histories of roll decay tests resulting from SSFSRVM simulations and experimental measurements. Furthermore, the top views of the wave pattern around the hull will be also compared in this section to show the effectiveness of SSFSRVM on simulating surface waves. Next, we will report what is the influence of the forward speed on the damping component.

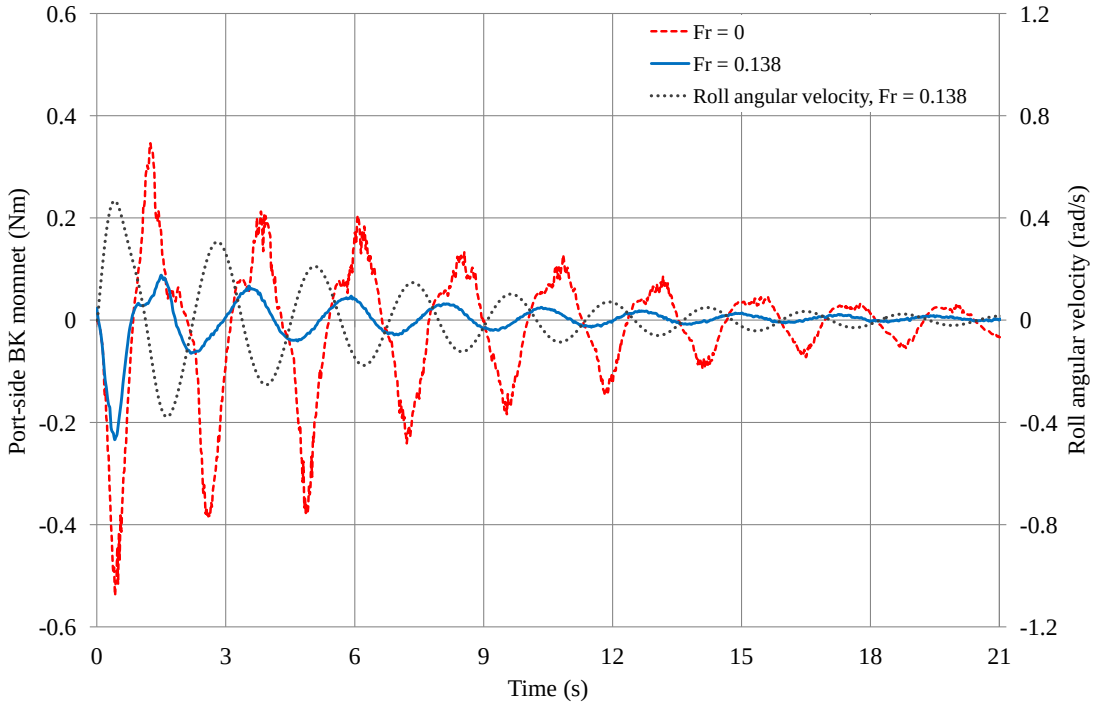

Figure 5.7: Comparison of the time histories of the hydrodynamic moment on the port-side bilge keel between two cases $Fr = 0$ and $Fr = 0.138$.

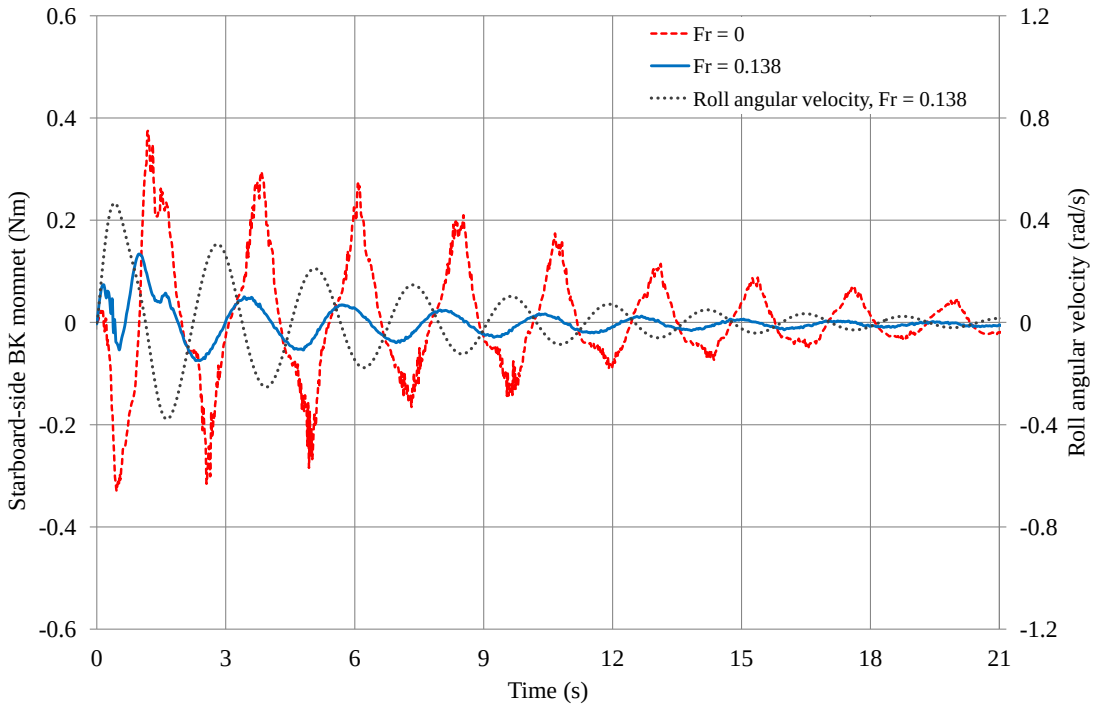

Figure 5.8: Comparison of the time histories of the hydrodynamic moment on the starboard-side bilge keel between two cases $Fr = 0$ and $Fr = 0.138$.

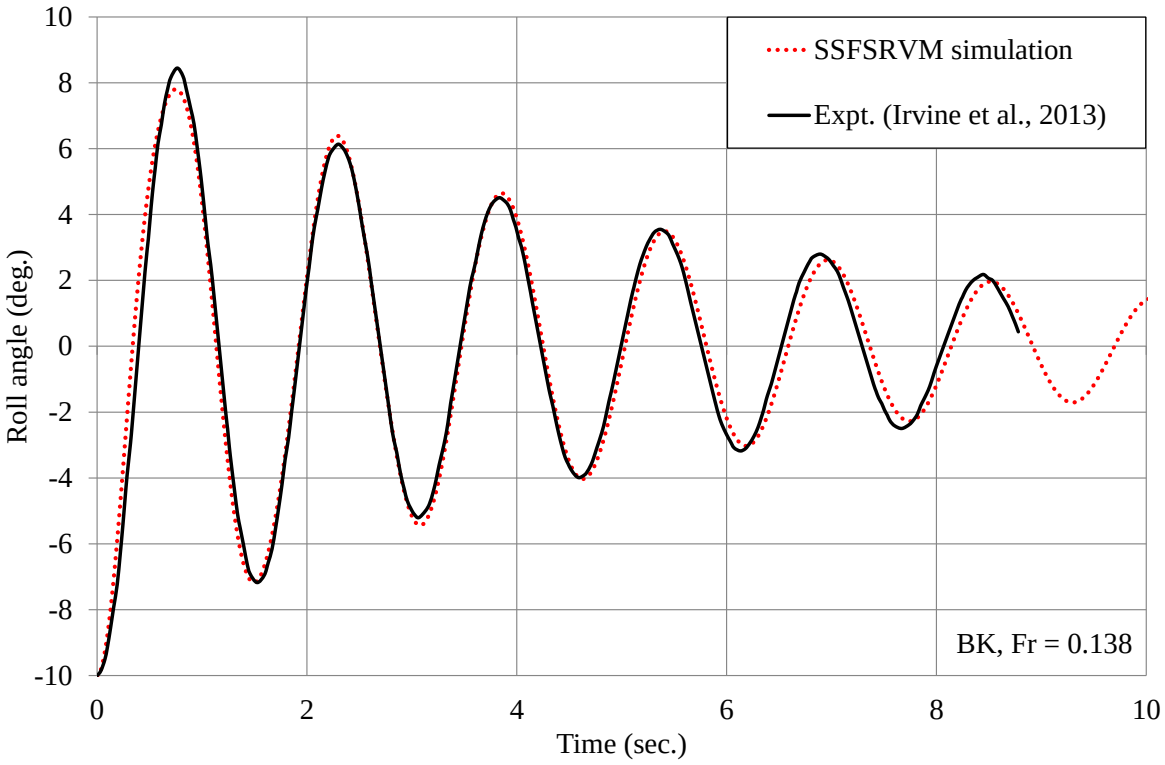

Figure 5.9: Time histories of the roll motion: experimental measurements and the SSFSRVM simulation for $Fr = 0.138$ and $R_0 = 10°$.

5.2.1 Roll time history and decay coefficient

Using SSFSRVM, we simulated the roll motion of the DTMB 5212 model with the Froude numbers Fr of 0.138, 0.280 and 0.410. The time histories of the roll motion resulting from the experiments and SSFSRVM simulations are presented in Figs. 5.9-5.11. It can be seen that the numerical predictions are in good agreement with the experimental measurements for all three different speed cases. Thus, we conclude that the SSFSRVM model is capable of simulating different forward speeds.

Figure 5.12 presents the time histories of the roll motion with the Froude numbers Fr of 0.138, 0.280 and 0.410, in order to directly demonstrate the effect of different forward speeds. We find that the model with the largest speed $Fr = 0.410$ decays the fastest, while the model with the smallest speed $Fr = 0.138$ decays the slowest. This means that increasing the forward speed can result in an increase in roll damping, as discussed in Section 5.1. Additionally, it is found that the forward speed also alters the roll period. Figure 5.13 shows the time histories of the predicted added moment-of-inertia of all three models, which clearly decrease as the forward speed increases.

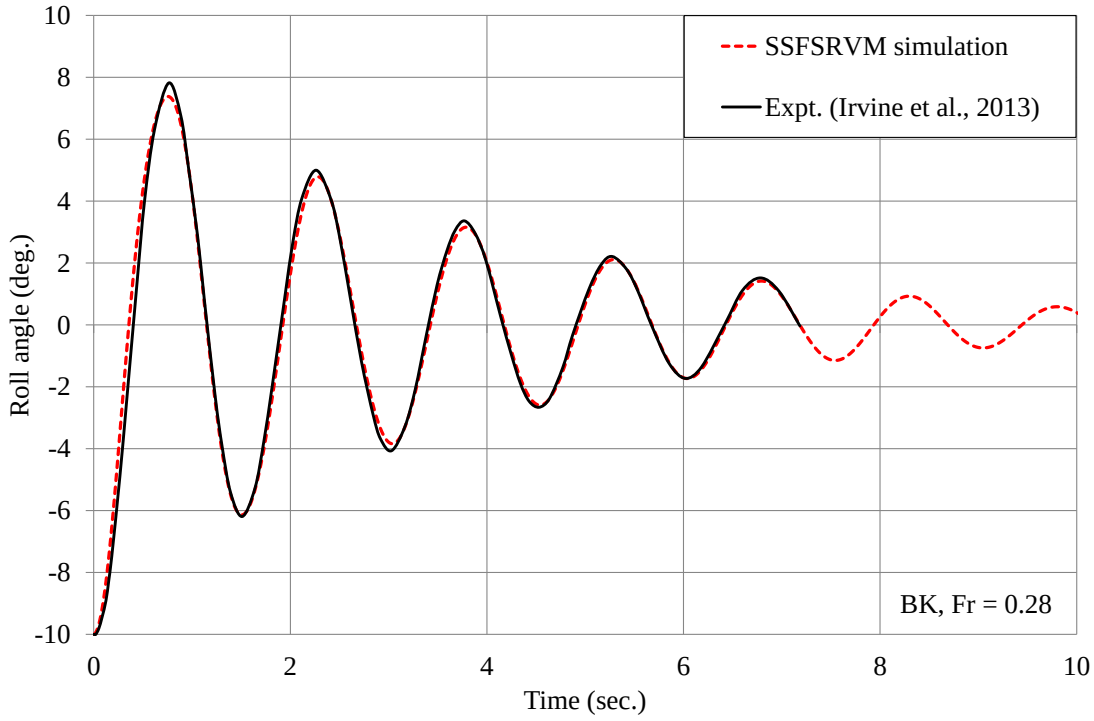

Figure 5.10: Time histories of the roll motion: experimental measurements and the SSFSRVM simulation for $Fr = 0.280$ and $R_0 = 10°$.

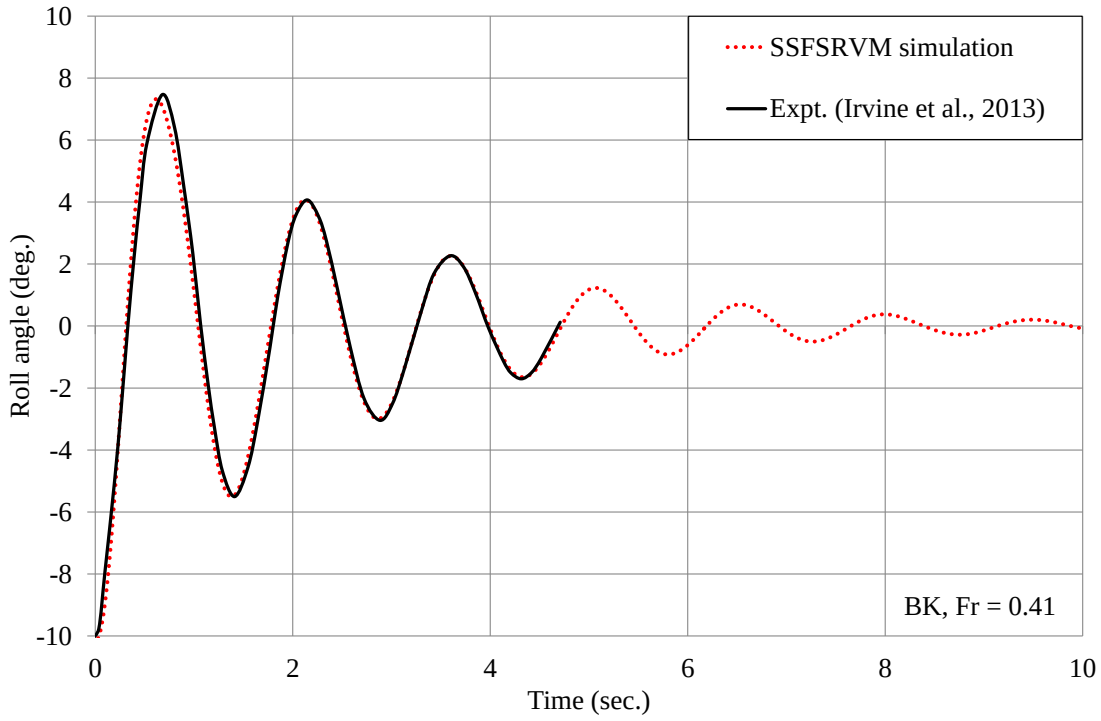

Figure 5.11: Time histories of the roll motion: experimental measurements and the SSFSRVM simulation for $Fr = 0.410$ and $R_0 = 10°$.

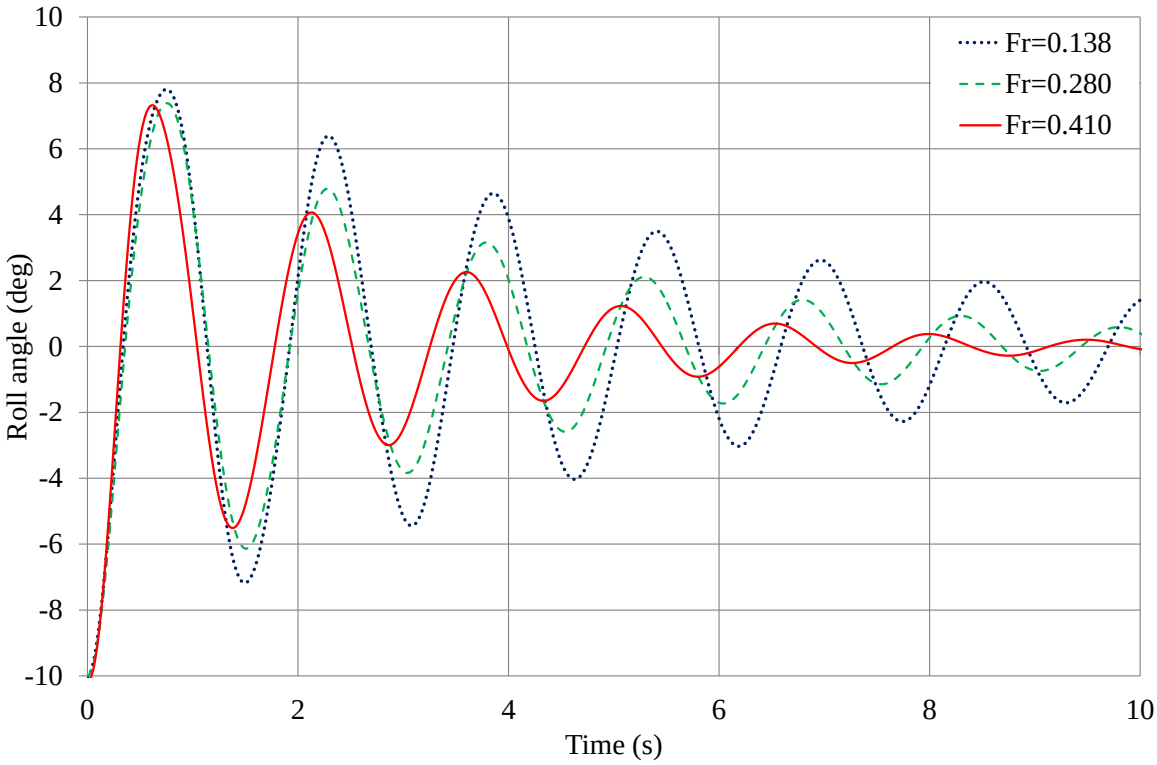

Figure 5.12: Comparison of the roll time histories resulting from SSFSRVM simulations among models with different Froude numbers.

To quantitatively examine the effect of forward speed on roll damping, we compare the roll decay coefficients of the three models with different forward speeds. Figure 5.14 presents the non-dimensional decay coefficient derived from the roll decay numerical data of Figs. 5.9-5.11. We find that values of the decay coefficients do not vary much over the range of the mean roll angle for all three models. This result indicates that the presence of forward speed in the model lessens the nonlinear component of the total damping, as discussed in Section 5.1. Furthermore, the largest forward speed should result in the most linear total damping. This point can be verified by the fact that the curve of $Fr = 0.410$ in Fig. 5.14 is the flattest one among the three. In conclusion, the nature of the roll damping changes from being nonlinear to more linear as ship speed increases, because bilge-keel vortex filaments do not stay as long to roll up and affect the hydrodynamic pressure on the bilge keels.

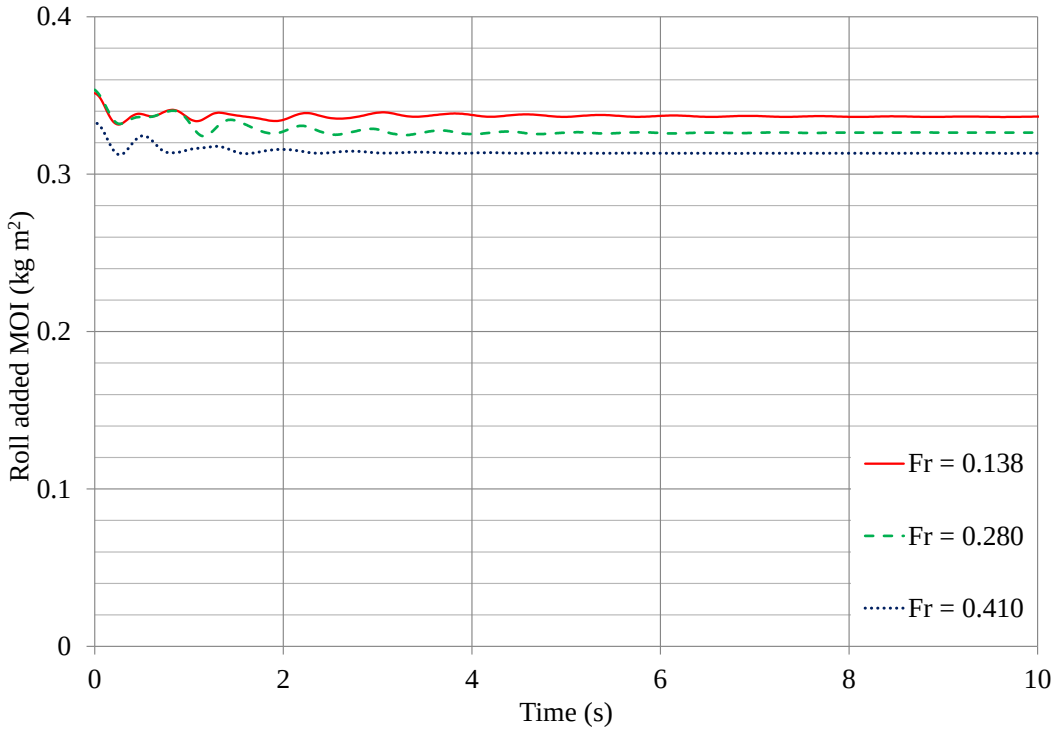

Figure 5.13: Comparison of the added moment-of-inertia among models with different Froude numbers.

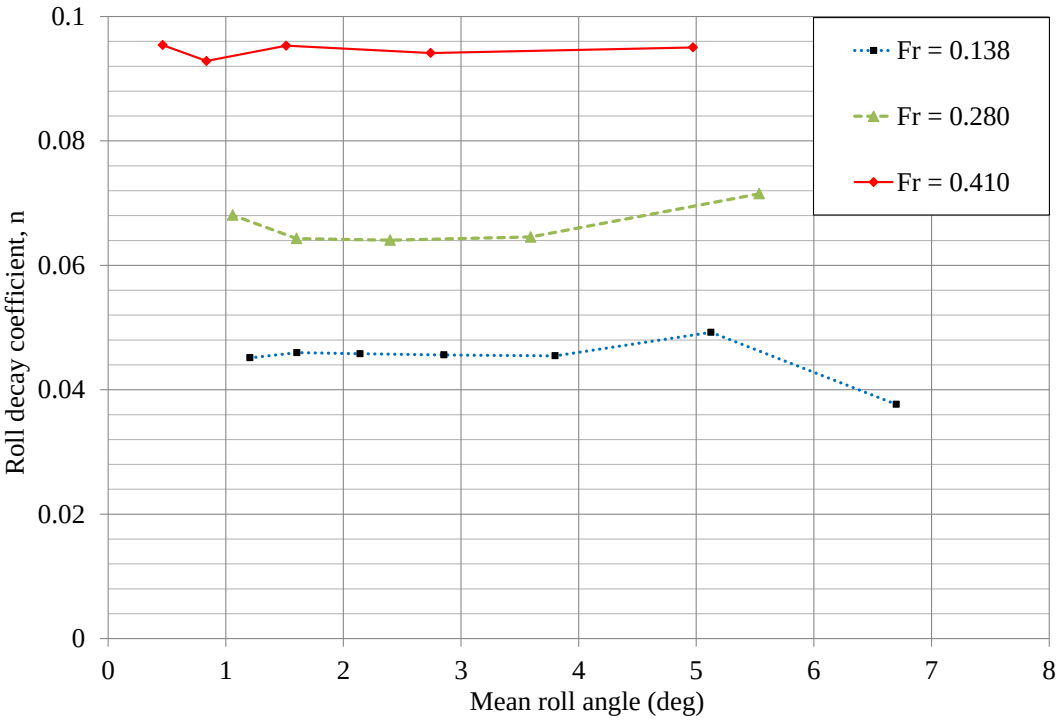

Figure 5.14: Comparison of the roll decay coefficients among models with different Froude numbers.

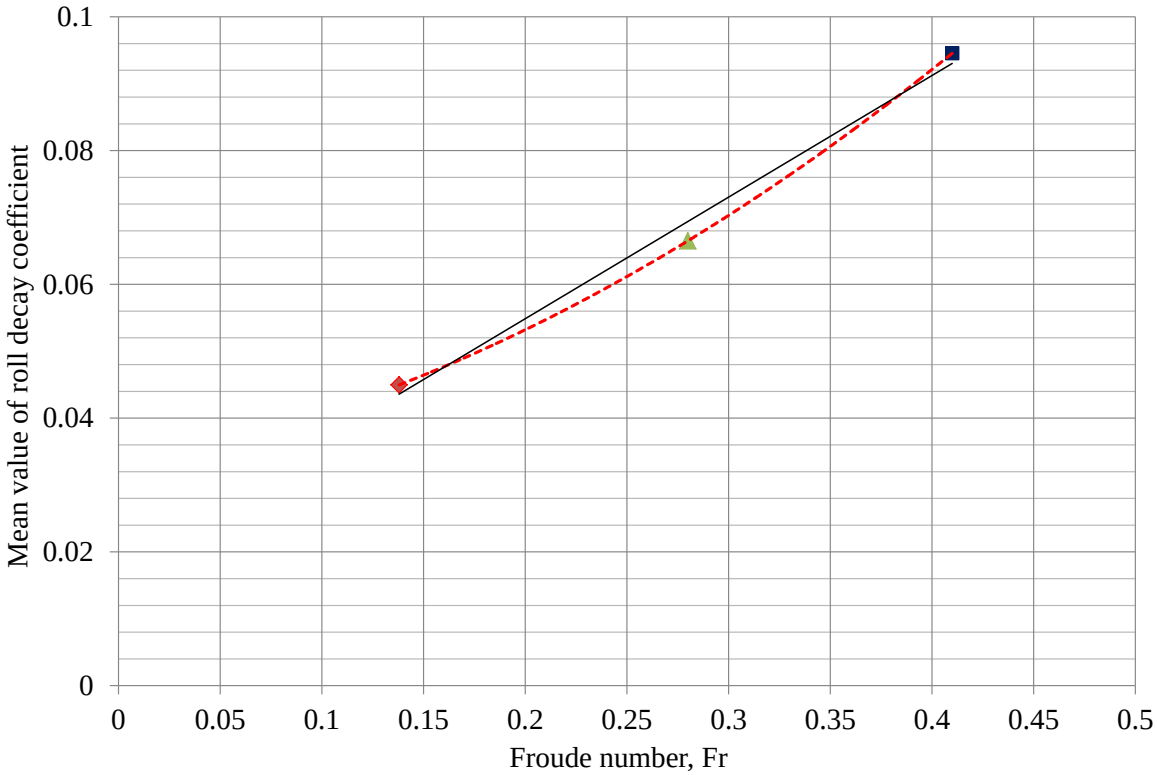

Figure 5.15: Forward speed effect on mean roll decay coefficients.

In addition, we find the decay coefficient monotonically increases with increase of hull speed. Since the curves of the decay coefficients in Fig. 5.14 are quite flat, the mean value of each data set should be approximately proportional to the linear damping of the corresponding case. To inspect the relation between the linear damping and the forward speed, we plot the mean value of roll decay coefficient versus the Froude number, as seen in Fig. 5.15. The solid line represents a linear fit of the data, while the dashed line is a quadratic fit. Examination of the lines shows that a quadratic polynomial of the Froude number can predict the roll decay coefficient better. Thus, the linear damping is more likely a quadratic function of the forward speed.

5.2.2 Wave damping

To investigate the role of wave damping component in the total linear damping of a hull with forward speed, we simulate the free decay test of the bare hull without bilge keels in an inviscid fluid for the case of $Fr = 0.280$. In this case the bilge-keel damping, lift damping, and surface-friction damping are eliminated from the

numerical model. Besides, the hydrodynamic added moment of inertia is reduced. To ensure the bare hull decays with the same natural period, the moment of inertia of the hull is increased correspondingly. Therefore, the damping calculated from the bare hull in an inviscid fluid can be assumed to be the wave damping of the bilge-keel hull in a viscous fluid. The predicted roll time history of the bare hull is shown in Fig. 5.16, compared with that of the bilge-keel hull. It can be seen that the rolling motion of the inviscid model still decays quite fast though the bilge keels and fluid viscosity are not included in the model. Figure 5.17 presents the non-dimensional decay coefficient derived from the roll decay numerical data of Fig. 5.16. In the figure, the linear fit of the roll decay coefficient of the bilge-keel hull is also shown in the figure to calculate the total linear damping. By comparing the wave damping and the total linear damping, we find that about 90 percent of the total linear damping comes from the wave damping, for $Fr = 0.280$. This indicates that wave damping prevails in the presence of ship forward speed.

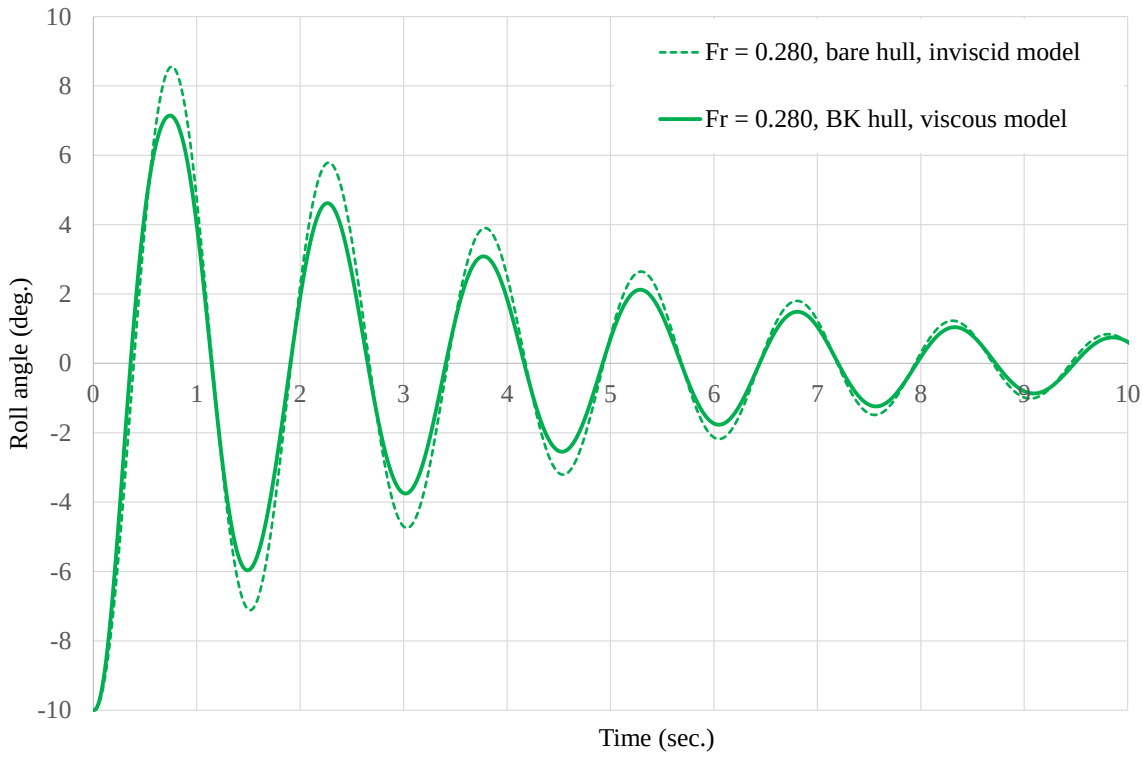

Figure 5.16: Time histories of the roll motion of the bare hull of DTMB 5415 model in an inviscid fluid and the bilge-keel hull in a viscous fluid for $Fr = 0.280$.

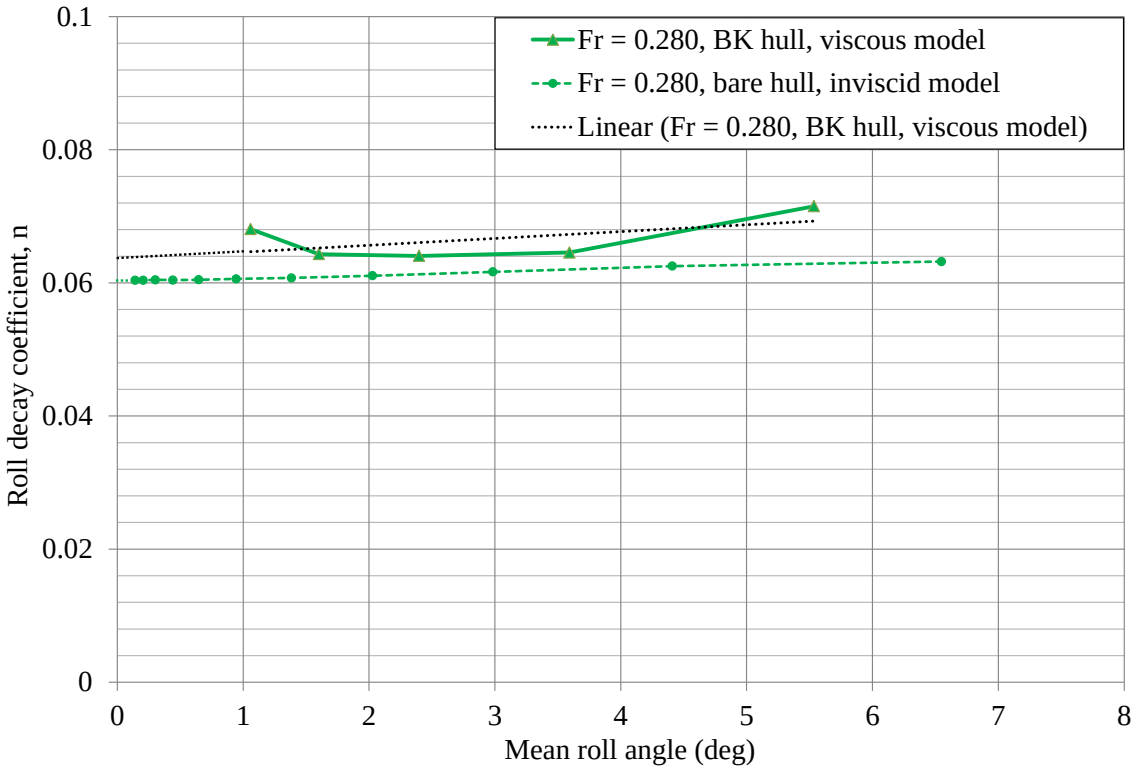

Figure 5.17: Roll decay coefficients of the bare hull of DTMB 5415 model in an inviscid fluid and the bilge-keel hull in a viscous fluid for $Fr = 0.280$.

5.2.3 Surface waves

The measurements of the wave pattern around the DTMB 5412 model for the case of $Fr = 0.138$ have been published in Irvine *et al.* (2013). To examine the accuracy of SSFSRVM model in simulating the surface waves, Fig. 5.18 shows the comparison of the top view of the surface waves during steady state, when the disturbance of the roll-induced waves is trivial and the roll angle θ_b has decayed to 3% of the initial angle $R_0 = 10$ deg. The upper part of the figure shows the experimental measurements of the wave pattern on the starboard side, while the lower part shows our numerical simulation of the wave pattern on the port side. Since the roll angle has decayed to a very small value, the degree of the symmetry of Fig. 5.18 will indicate the degree of accuracy of the numerical model in simulating surface waves.

As shown in Fig. 5.18, the numerical model successfully produces the divergent waves with the same angle as those measured in the experiment. In addition, the locations of the peaks and troughs are also predicted by the SSFSRVM model very accurately. However, minor differences can be found in the comparison. For instance,

a strong trough appears at the stern in the numerical model, while in the experiment stern waves are not as strong. In general, the wave patterns in the upper and lower parts of Fig. 5.18 show good agreement. Therefore, we conclude that the SSFSRVM model is capable of simulating surface waves around an advancing hull.

Figure 5.19 shows the surface waves as viewed from the top in the first oscillation of decaying motion. Each column in this figure represents a specific forward speed, and each row represents an instant of time that are selected to correspond with the peaks and zero crossing of the roll motion for each ship. The first row shows the steady surface waves that are created by the constant forward speed and the static heel of the ship before $t = 0$ sec when the ship is released to roll freely. It can be seen that divergent waves emanate from the bow and stern of the ship. The surface waves in the model of Fr=0.138 have the largest divergent angle among the three models, and have the smallest wave amplitudes. On the other hand, the divergent waves of the case of Fr=0.410 have the largest wave amplitudes. These results reveal the fact that increasing the forward speed increases the the amplitudes of divergent waves, and consequently results in a larger wave drag on the ship.

After the ship model is released to roll freely (see the sub-figures from rows 2 to 5 in Fig. 5.19), peaks and troughs of the roll-induced waves are generated alternately on both sides of the hull and travel away from the hull. The divergent wave amplitudes are in varying stages, especially for the case of Fr=0.138. Since the divergent waves for the cases of Fr=0.280 and 0.410 have very large amplitudes, the initial divergence wave field has not been disturbed significantly.

In summary, the presence of ship forward speed convects the bilge-keel vortices and eddies downstream fast, so they do not stay long enough to affect the pressure distribution on the hull and bilge keels. Consequently, the quadratic damping component of the DTMB 5412 ship model decreases with the forward speed. The nature of the total damping changes from being nonlinear to being more linear as ship speed increases. The wave damping dominates the total damping. With respect to the relation between the linear damping and the forward speed, it is found that the linear damping is more likely a quadratic function of the forward speed.

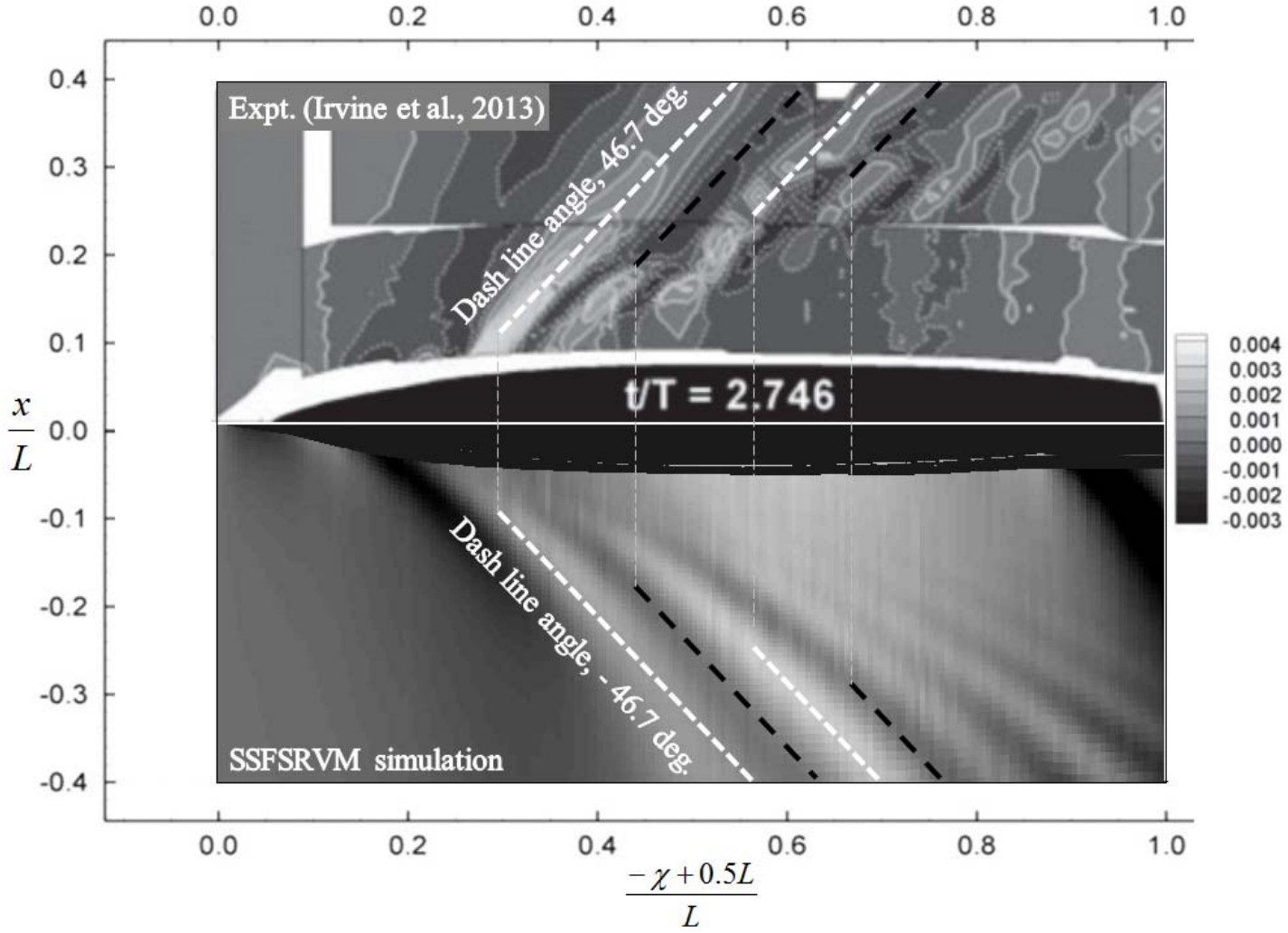

Figure 5.18: Comparison of the top view of the surface waves obtained from numerical simulations and experimental measurements during a steady state for case of $Fr = 0.138$.

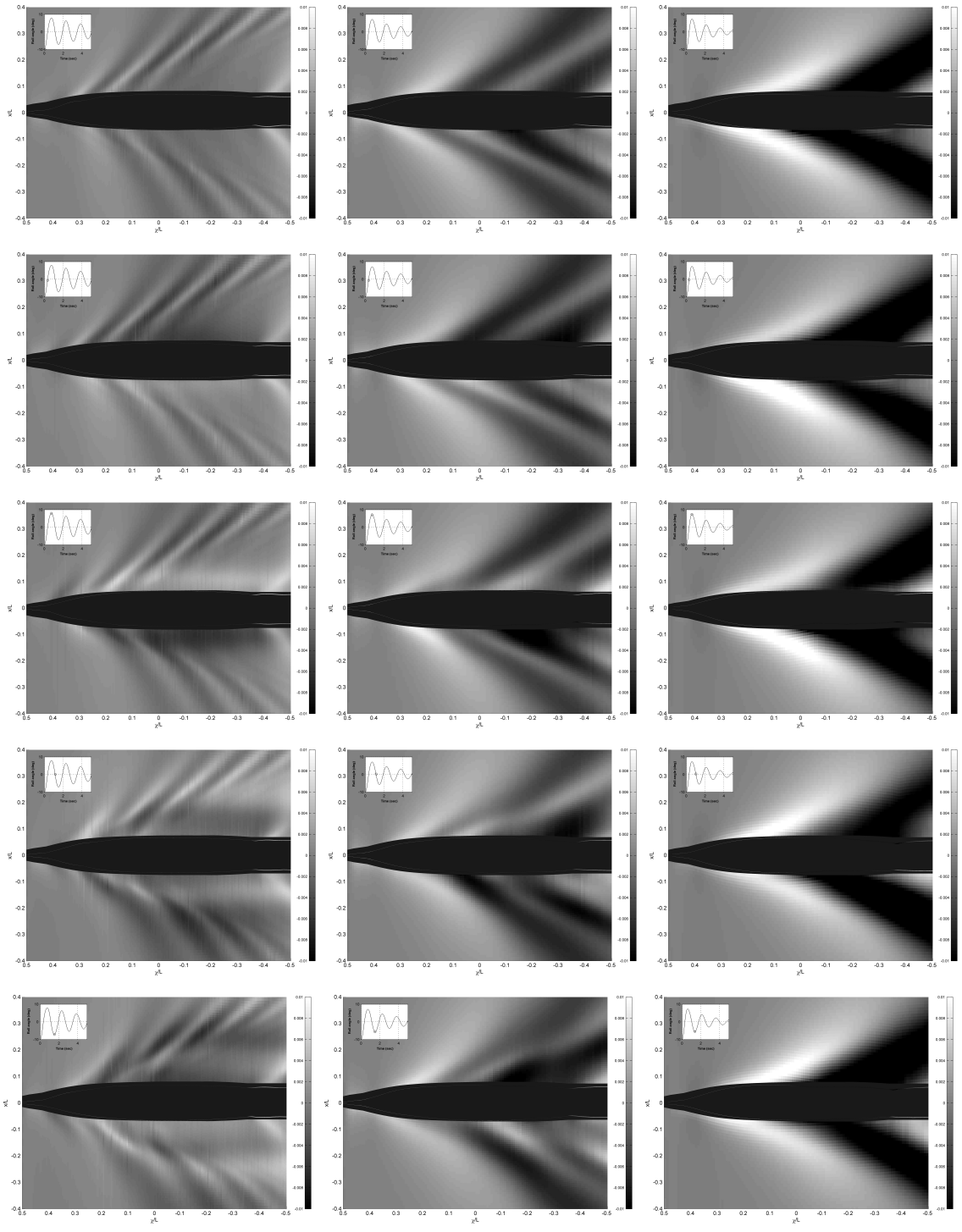

Figure 5.19: Comparison of surface waves from the top view between hulls with different forward speeds. Columns from left to right represent Fr=0.138, Fr=0.280, and Fr=0.410, respectively.

This page intentionally left blank.

Chapter 6

Conclusions

In this study, we validated the slender-ship free-surface random-vortex method in simulating the free roll decay motion of a vessel with and without forward speed. The numerically predicted vorticity contours near a bilge keel closely matched existing PIV measurements. In the presence of forward speed, the numerical model also successfully produced divergent waves with the same angles as those measured in the experiment, and accurately predicted the locations of the peaks and troughs of the divergent waves. We believe that the SSFSRVM model is capable of predicting the roll motion of a hull, simulating the behavior of the vortical structures in the fluid, and capturing the divergent waves on the surface.

With regard to the effects of bilge keel span in the case of zero forward speed, it was found that a larger bilge keel generated stronger counter-rotating vorticity pairs. The vortices and the flow separations caused by a bilge keel resulted in a pressure difference between the upper and lower sides of the bilge keel, and produced an additional hydrodynamic moment on the hull. The hydrodynamic moment was 180 degrees out of phase with the roll angular velocity, and it performed negative work and consumed the kinetic energy of the ship during the decay process. Thus, a larger bilge keel provides more damping to decrease the roll amplitude. Based on the plot of roll decay coefficient versus the roll angle, the fully nonlinear behavior of the roll damping was evident. The quadratic damping played an important role in the total damping when the mean roll angle was small ($< 5^\circ$). A larger bilge-keel span resulted in larger quadratic damping. In the presence of incident beam waves, increasing the bilge keel span significantly reduced the amplitude of the roll motion.

The presence of ship forward speed convected the bilge-keel vortices and eddies downstream fast, so that they did not stay long enough to affect the pressure distribution on the hull and bilge keels. The normal hydrodynamic forces on the bilge keels are reduced. Consequently, the quadratic damping component decreased with forward speed. The nature of the total damping changed from being nonlinear to being more linear as ship speed increased. The wave damping dominates the total damping. With respect to the relation between the linear damping and the forward speed, we observed that the linear damping is more likely a quadratic function of the forward speed.

In the end, considering the accuracy and the computation time, we conclude that SSFSRVM is an excellent modeling tool for predicting the roll motion of a ship with bilge keels and forward speed.

Bibliography

[1] Aloisio, G. and Di Felice, F. (2006). "PIV analysis around the bilge keel of a ship model in free roll decay", XIV Congresso Nazionale AI VE. LA., Rome, Italy, November.

[2] Araki, M., Sadat-Hosseini, H., Sanada, Y., Tanimoto, K., Umeda, N., and Stern, F. (2012). "Estimating maneuvering coefficients using system identification methods with experimental, system-based, and CFD free-running trial data", *Ocean Engineering*, 51, 63-84.

[3] Avalos, G. O. G., Wanderley, J. B., and Fernandes, A. C. (2013). "Roll damping decay of a FPSO with bilge keel", *Proceedings of the 32nd ASME International Conference on Ocean, Offshore and Arctic Engineering*, Nantes, France.

[4] Bassler, C. C., and Reed, A. M. (2009). "An analysis of the bilge keel roll damping component model", *Proceedings of the 10th International Conference on Stability of Ships and Ocean Vehicles (STAB2009)*, June 22-26, St Petersburg, Russia.

[5] Bassler, C. C., Reed, A. M., and Brown, A. J. (2010). "A Method to Model Large Amplitude Ship Roll Damping", *Proceedings of the 11th International Ship Stability Workshop*, Wageningen, The Netherlands.

[6] Beck, R. F. (1994). "Time-domain computations for floating bodies", *Applied ocean research*, 16(5), 267-282.

[7] Broglia R., and Di Mascio A.,(2003). "Unsteady RANSE calculations of the fow around a moving ship hull",*8th NSH*, Busan, Korea.

[8] Chakrabarti, S. (2001). "Empirical calculation of roll damping for ships and barges", *Ocean Engineering*, 28(7), pp. 915-932.

[9] Chorin, A. J. (1973). "Numerical study of slightly viscous flow", *Journal of Fluid Mechanics*, Vol. 57, pp. 785-796.

[10] Dalzell, J. F. (1978). "A note on the form of ship roll damping", *Journal of Ship Research*, Vol 22(3), pp. 178-185.

[11] Einstein, A. (1956). "Investigation on the Theory of Brownian Movement", Courier Dover Publications, New York.

[12] Faltinsen, O. M. (1990). *Sea loads on ships and offshore structures*, Cambridge university press, UK.

[13] Froude, W. (1872). "On the influence of resistance upon the rolling of ships", *Naval Science*, 1: 411-429.

[14] Grosenbaugh, M. A. and Yeung, R. W. (1989). "Nonlinear Free-surface Flow at a Two-dimensional Bow", *J. Fluid Mech.*, Vol. 209, pp. 57-75.

[15] Han, S. L., and Kinoshita, T. (2012). "Nonlinear damping identification in nonlinear dynamic system based on stochastic inverse approach", *Mathematical Problems in Engineering*, vol. 2012, Article ID 574291.

[16] Himeno, Y. (1981). "Prediction of ship roll damping - state of the art", Technical Report No. 239, Dept Naval Arch and Mar Eng, Univ of Michigan.

[17] Ikeda, Y. (2004). "Prediction methods of roll damping of ships and their application to determine optimum stabilization devices", *Marine Technol*, 41(2), pp. 8993.

[18] Ikeda Y, Himeno Y, Tanaka N. (1976). "On roll damping force of shipeffects of friction on hull and normal force on bilge keels", *Journal of Kansai Society of Naval Architects*, 161: 41-49 (in Japanese).

[19] Ikeda Y, Himeno Y, Tanaka N. (1977a). "On eddy-making component of roll damping force on naked hull", *Journal of Japan Society of Naval Architects*, 162: 59-69(in Japanese).

[20] Ikeda Y., Himeno Y., and Tanaka N. (1978). "A prediction method for ship roll damping", Rep. No. 00405 of Dep. of Naval Arch., Univ. of Osaka.

[21] Ikeda Y, Himeno Y, Tanaka N. (1978). "Components of roll damping of ship at forward speed". *Journal of Japan Society of Naval Architects*, 143: 121-133 (in Japanese).

[22] Ikeda, Y. and Katayama, T., (2000). "Roll damping prediction method for a high-speed planing craft", *Proceedings of the 7th International Conference on Stability of Ships and Ocean Vehicles*, Tasmania, Australia.

[23] Ikeda Y, Komatsu K, Himeno Y, *et al.*(1977b). "On roll damping force of ship-effects of hull surface pressure created by bilge keels", *Journal of Kansai Society of Naval Architects*, 165: 31-40 (in Japanese).

[24] Jiang, Y. and Yeung, R. W. (2012). "Computational modeling of rolling cams for wave-energy capture in a viscous fluid", *Proceedings of the 31th ASME International Conference on Ocean, Offshore and Arctic Engineering*, Paper Number OMAE2012-84150, Rio de Janeiro, Brazil.

[25] de Kat, J. O., Pinkster, D. J., and McTaggart, K. A. (2002). "Random waves and capsize probability based on large amplitude motion analysis", *Proceedings of the 21st ASME International Conference on Offshore Mechanics and Arctic Engineering*, Oslo, Norway.

[26] Katayama, T., Taniguchi, T., and Kotaki, M., (2008). "A study on viscous effects of roll damping of a high-speed catamaran and a high-speed trimaran", *Proceedings of the 6th Osaka Colloq. Seakeeping and Stability of Ships*, Osaka, Japan.

[27] Kawahara, Y., Maekawa, K., and Ikeda, Y., (2009). "A simple prediction formula of roll damping of conventional cargo ships on the basis of Ikedas method and its limitation", *Proceedings of the 10th International Conference on Stability of Ships and Ocean Vehicles*, St. Petersburg, Russia.

[28] Kim, Y. (2002). "A numerical study on sloshing flows coupled with ship motion-the anti-rolling tank problem", *Journal of Ship Research*, 46(1), 52-62.

[29] Liao, S. W. (2000). "Development and Applications of the Free-Surface Random Vortex Method (FSRVM)", Ph.D. dissertation, University of California, Berkeley.

[30] Liao, S. W. and Roddier, D. R. (1998). "Generation of plunging breakers - laboratory and numerical simulation.", *OEG-98.1, OEGG, Univ. of California, Berkeley.*

[31] Miller, R., Bassler, C., Atsavapranee, P., and Gorski, J. (2008). "Viscous roll predictions for naval surface ships appended with bilge keels using URANS", *Proceedings of the 27th Symposium on Naval Hydrodynamics*, Seoul, South Korea.

[32] Nakos, D., and Sclavounos, P. (1991). "Ship motions by a three-dimensional Rankine panel method", *Proceedings of the 18th Symposium on Naval Hydrodynamics*, Ann Arbor, MI.

[33] Oliveira, A. C., and Fernandes, A. C. (2006). "The bilinear behavior for FPSO rolling motions", *Proceedings of the 9th International Conference on Stability of Ships and Ocean Vehicles*, Brazil.

[34] Oliveira, A. C., and Fernandes, A. C. (2014). "The nonlinear roll damping of a FPSO hull", *Journal of Offshore Mechanics and Arctic Engineering*, 136(1), 011106.

[35] Quérard, A. B. G., Temarel, P. and Turnock, S. R. (2008). "Influence of viscous effects on the hydrodynamics of ship-like sections undergoing symmetric and anti-symmetric motions, using RANS", *27th International Conference on Offshore Mechanics and Arctic Engineering*, Estoril, Portugal.

[36] Ribeiro e Silva, S., and Guedes Soares, C. (2013). "Prediction of parametric rolling in waves with a time domain non-linear strip theory model", *Ocean Engineering*, 72, 453-469.

[37] Roberts, J. B. (1985). "Estimation of nonlinear ship roll damping from free-decay data", *Journal of Ship Research*, Vol. 129 (2), pp. 127-138.

[38] Roddier, D. R., Liao, S. W., and Yeung, R. W. (1999). "Time-domain solution of freely-floating cylinders in a viscous fluid", *Proceedings of the 9th International Conference of Society of Offshore and Polar Engineers*, vol. III, pp. 454-462, Brest, France.

[39] Roddier, D. R., Liao, S. W. and Yeung, R. W. (2000). "Wave-induced motion of floating cylinders fitted with bilge keels.", *Int'l J. Offshore Polar Engr.*, Vol. 10, pp. 241-248.

[40] Roddier D. R., Liao S. W., and Yeung R. W. (2000). "On freely-floating cylinders fitted with bilge keels", *Proceedings of the 10th International Society of Offshore and Polar Engineers (ISOPE)*, Seattle.

[41] Sadat-Hosseini, H., Carrica, P., Stern, F., Umeda, N., Hashimoto, H., Yamamura, S., and Mastuda, A. (2011). "CFD, system-based and EFD study of ship dynamic instability events: Surf-riding, periodic motion, and broaching", *Ocean Engineering*, 38(1), 88-110.

[42] Salui, K. B, Sarkar, T., Vassalos, D. (2000). "An improved method for determining hydrodynamic coefficients in roll motion using CFD techniques", *Journal of Ship Technical Research*, Vol. 47, pp.161174.

[43] Sarkar, T. and Vassalos, D. (2000). "A RANS-based technique for simulation of the flow near a rolling cylinder at the free surface", *Journal of Marine Science and Technology*. Vol.5, pp. 66-77.

[44] Seah, R. K. M. (2007). "The SSFSRVM computational model for three-dimensional ship flows with viscosity", Ph.D. dissertation, University of California, Berkeley.

[45] Seah, R. K. M. and Yeung, R. W. (2003). "Sway and roll hydrodynamics of cylindrical sections", *International Journal of Offshore and Polar Engineering*, Vol.13, 4, pp. 241-248.

[46] Seah, R. K. M. and Yeung, R. W. (2008). "Vortical-flow modelling for ship hulls in forward and lateral motion", *Proceedings of the 27th Symposium on Naval Hydrodynamics*, Seoul, S. Korea.

[47] Thiagarajan, K. P. and Braddock, E. C. (2010). "Influence of bilge keel width on the roll damping of FPSO", *Journal of Offshore Mechanics and Arctic Engineering*. Vol. 132, 011303. doi:10.1115/1.3160384.

[48] Turk, A., Prpi-Ori, J., e Silva, S. R., and Soares, C. G. (2013). "Experimental investigations of roll damping of the C11 containership for the prediction of parametric rolling in regular waves", *Hydraulic Engineering II*, 127.

[49] Vinje, T. and Brevig, P. (1980). "Nonlinear, two-dimensional ship motions", Tech. Rept., The Norwegian Inst. Of Tech., Trondheim.

[50] Wilson, R. V., Carrica, P. M., and Stern, F. (2006). "Unsteady RANS method for ship motions with application to roll for a surface combatant", *Computers & Fluids*. Vol.35 (5), pp. 501-524.

[51] Xia, J., Wang, Z., and Jensen, J. J. (1998). "Non-linear wave loads and ship responses by a time-domain strip theory", *Marine Structures*, 11(3), 101-123.

[52] Yeung, R. W. (2002). "Fluid dynamics of finned bodies - from VIV to FPSO", Plenary Paper, *Proceedings of the 12th International Society of Offshore and Polar Engineers (ISOPE)*, Vol. 3, pp. 1-11.

[53] Yeung, R. W. and Cermelli, C. A. (1998). "Vortical flow generated by a plate rolling in a free surface", *Free surface flow with viscosity, advances in fluid mechanics, Comp. Mech.*, Vol. 16, pp. 1-36.

[54] Yeung, R. W., Cermelli, C. A. and Liao, S. W. (1996). "Vorticity fields due to rolling bodies in a free surface - experiment and theory", *Proc. 21st ONR Symp. on Naval Hydrodyn.*, Trondheim, Norway.

[55] Yeung, R. W. and Jiang, Y. (2011). "Effects of shape on viscous damping and motion of heaving cylinders", *Proc., 30th International Conference on Ocean, Offshore and Arctic Engineering*, Paper Number OMAE2011-50243, Rotterdam, The Netherlands

[56] Yeung, R. W. and Kim, S. H. (1981). "Radiation forces on ships with forward speed", *Proceedings of the 3rd International Conference on Numerical Ship Hydrodynamics*, Paris, France, June 16-19.

[57] Yeung, R. W. and Liao, S. W. (1999). "Time-domain solution of freely floating cylinders in a viscous fluid.", *Proc. 9th Int'l Soc. Offshore Polar Engr., Brest, France.*

[58] Yeung, R. W., Liao, S. W. and Roddier, D. R. (1998). "Hydrodynamic coefficients of rolling rectangular cylinders", *Int'l J. Offshore Polar Engr.*, Vol. 8(04), pp. 241-250.

[59] Yeung, R. W., Roddier, D. R., Alessandrini, L., Gentaz, L, and Liao, S. W. (2000). "On roll hydrodynamics of cylinders fitted with bilge keels", *Proceedings of the 23rd Symposium on Naval Hydrodynamics*, Val de Reuil, France.

[60] Yeung, R. W., Seah, R. K. M. and Imamura J. T. (2013). "Lateral force and yaw moment on a slender body in forward motion at a yaw angle", *Journal of Offshore Mechanics and Arctic Engineering*, 135 (3), 031101. doi:10.1115/1.4006153.

[61] Yeung, R. W. and Vaidhyanathan, M. (1994). "Highly separated Flows Near a Free Surface", *Proc. Intl Conf. on Hydrodynamics*, Wuxi, China.